

https://dspace.org/

Traumatic effects of lightning strike on human bone morphology and ultrastructure

Bacci, Nicholas

2016-10-17
http://hdl.handle.net/10539/21230

Downloaded from a DSpace repository. https://dspace.org/

Traumatic Effects of Lightning Strike on Human Bone Morphology and Ultrastructure



Nicholas Bacci

A Dissertation submitted to the Faculty of Health Sciences, University of the Witwatersrand, Johannesburg, in fulfilment of the requirements for the degree of Master of Science

FACULTY OF HEALTH SCIENCES
UNIVERSITY OF THE WITWATERSRAND, JOHANNESBURG

2016

Declaration

I, Nicholas Bacci, declare that this dissertation entitled “Traumatic Effects of Lightning Strike on Human Bone Morphology and Ultrastructure” is my own unaided work. It is being submitted for the Degree of Master of Science in Medicine at the University of the Witwatersrand, Johannesburg. It has not been submitted before for any degree or examination at any other University.

_____

Nicholas Bacci

13 June 2016 at Parktown, Johannesburg

Abstract

South Africa reports lightning fatality rates as high as 8.8 per million annually. Traditionally, forensic lightning fatality identification consists of soft tissue traumatic pattern recognition. This does not allow for manner of death identification in cases of full skeletonization.

This study has expanded upon our earlier research, which identified characteristic patterns of lightning disruption in non-human bone. We thus explored the effects of induced lightning high voltage current on human cadaveric material in order to recognise electrically induced trauma. The objectives comprised analysis of microstructural damage through conventional thin-section histology, micro-focus computed tomography and histomorphometry.

Experimentation was undertaken on bone blocks extracted from human lower limbs obtained from cadaveric specimens. An experimental system for simulated lightning induction to bone was developed and investigations were carried out on twenty-two bone block specimens. Micro-focus computed tomography was undertaken prior and after experimental treatment; while three blocks were used unmodified as control samples. Thin sections were obtained following post-trauma imaging. Measurements and photomicrographs of the alteration patterns were taken, while micro-focus computed tomography data were reconstructed and visualised as 2D orthoslices and 3D rendered volumes.

Results indicated a poor efficiency of micro-focus computed tomography to resolve traumatic features in cortical bone. However, conventional histological methods demonstrated cortical bone trauma patterns well, allowing easy identification. Statistical analyses demonstrated relationships between current intensity and extent as well as typology of damage observed.

The relationships identified suggested a dual mechanism of bone trauma, consisting of a combination of both electrically and thermally induced alterations. This study has thus allowed a primary overview and analysis of lightning trauma to human skeletal tissues.

Dedication

To my wife, the woman who stands with me always and forever

Anu Joseph

Acknowledgements

I thank the NRF for funding the equipment at Necsa (grant number: UID 72310) (FB, JH, LB); the NRF, Eskom (TESP programme) and the Department of Trade and Industry (THRIP) for funding the Lightning/EMC Research Group; CBI-electric for funding the Chair of Lightning at the University of the Witwatersrand and for direct support of the Lightning Research Group (HH, KN). I would like to thank the NRF Thuthuka and Carnegie Corporation Transformation Programme at the University of the Witwatersrand for funding the Olympus iX51 Inverted Microscope and CellSense Software (TNA). Thanks are also due to the FRC and the JJJ Smieszieck grant (NB).

I humbly thank the Radiography and Tomography group (RADTOM) of the Radiation Sciences department at Necsa and Dr Frikkie de Beer, Jakobus Hoffman and Lunga Bam that assisted me in the realisation of the micro-focus computed tomography aspect of this project by allowing access to their equipment and their expertise. I thank the School of Information and Electrical Engineering, particularly Prof Ken Nixon and Mr Hugh Hunt, as well as two of their students, Harry Lee and Carson McAfee, for their extensive assistance with the experimental procedures and making the electrical equipment necessary for this study available as well as their assistance in imparting in me their understanding of the electrical aspects of this study. Thanks are also due to the School of Anatomical Sciences for providing consumables and access to the human cadaveric collection.

I direct my thanks to Dr Patrick Randolph-Quinney for his backing, proficiency and supervision and Dr Tanya Augustine for her constant guidance, reliability, mentoring, and unyielding support throughout this struggling endeavour, against all odds.

Thanks are also due to Mrs Hasiena Ali and Mrs Alison Mortimer for their assistance and training in histological and staining methods throughout the course of the laboratory work conducted for this study.

I greatly thank Mr Brendon Billings for his support and assistance in coping with the hardships of a postgraduate degree as well as mentoring me into a better individual.

A great deal of thanks are due to friends and the fellow postgraduate students who came to my support when I was in need, in the darkest hours: Josh Davimes, Kyrtania Pather, Shayla Pillay, Martin Bernert, Nicholas Driver, and Dean Harris.

Contents

Declaration....ii
Abstract....iii
Dedication....iv
Acknowledgements....v
Table of Contents....vii
Nomenclature....ix
List of Figures....x
List of Tables....xii
1 INTRODUCTION....1
1.1 A Brief Description of the Lightning Phenomenon....1
1.2 Mechanisms and Reported Lightning Injuries and Fatalities....4
1.3 Lightning Trauma Simulation and Identifiers of Microstructural Bone Trauma....10
1.4 Experimental Concerns and Understanding....15
1.5 Aims and Objectives....16
2 MATERIALS AND METHODOLOGY....17
2.1 Sample Acquisition....17
2.2 Electrical Testing Experimental Design....20
2.3 Fluid Electrical Property Testing....22
2.4 Bone Samples Curent Testing Procedure....23
2.4.1 Provisional testing of current application to bone samples....23
2.4.2 Parallel plate current mode....24
2.4.3 Wire-directed current mode....24
2.4.4 Photography of experimental current application procedures....25
2.5 Bone Block Processing....25
2.6 Multi-disciplinary Histological Analysis....28
2.7 Micro-focus Computed Tomography....31
3 RESULTS....32
3.1 Electrical Charcteristics of Embalming Fluid Compared to Isotonic Saline....32
3.2 The Macroscopic Effects of High Voltage Impulse Current on Bone....36
3.3 Qualitative Observations of Bone Microscopic Structural Modification....41
3.4 Quantitative Analysis of Miroscopic Fracturing....47
3.4.1 Preliminary investigation of relationships between fracture measurements and controlled current outputs....47
3.4.2 Evaluation of microscopic damage in relation to current voltage and mode of current application through variable dimension reduction....51

3.5 Micro-focus Computed Tomography Observations 64
4 DISCUSSION 69
4.1 Methodology Construct Validity and Fluid Testing 69
4.2 Observed High Voltage Impulse Current Induced Damage 71
4.3 Understanding Micro-fracture Occurrence, Extent, and Typology 74
4.4 Quantification of Electrical Effects on the Bone Histological Structure 82
4.5 The Inability of Micro-focus Computed Tomography in Resolving Micro-fracturing 85
5 CONCLUSION 87
5.1 Introduction 87
5.2 Findings 87
5.3 Limitations and Future Studies 90
References 95
APPENDIX A: Solution Recipes 108
APPENDIX B: Original Photomicrographs 110
APPENDIX C: Descriptie Statistics 113
APPENDIX D: Intra-Class Corellations 114
APPENDIX E: KWA Full Analysis 118
APPENDIX F: PCA Extra Iteration 137
APPENDIX G: Ethics Clearance Waiver 139
APPENDIX H: Turnitin Report 140

Nomenclature

CATPCA - Categorical Principal Components Analysis

COD – Cause of Death

CP – Charging Potential

FA - Fracture Area

FL - Fracture Length

FN – Fracture Number

FP - Fracture Perimeter

FT - Fracture Type

FW - Fracture Width

KMO - Kaiser-Meyer-Olkin

KWA – Kruskal-Wallis ANoVA by ranks

Mode - Mode of Current Application

MI – Myocardial Infarction

µCT – Micro-focus computed tomography

NC – Natural Causes

No - Number

N/A – Not Available

pC - Peak Current Traversing a Specimen

PCA – Principal Component Analysis

PPM – Parallel Plate Mode of Current Application

pV - Peak Voltage Generated

TBA – Total Bone Area

TFA – Total Fracture Area

WDM – Wire-directed Mode of Current Application

List of Figures

Figure Number	Title of Figure	Page
Figure 1.3.1	Example of basic human bone histological structure	11
Figure 1.3.2	Comparison of control slides A1 (giraffe) and A2 (pig) to experimental slides B1, B2 (giraffe) and B3, B4 (pig) (Bacci *et al.* 2014)	14
Figure 2.1.1	Schematic of bone block extraction from femora and tibiae	20
Figure 2.2.2	Photograph of the impulse generator used in the experimental procedure	21
Figure 2.3.1	Photograph of the experimental design for fluid electrical property testing	22
Figure 2.4.1.1	Photographs of parallel plate arrangement (A) and wire-directed for experimental current application	24
Figure 2.6.1	Example of fracture measurement procedure	29
Figure 3.1.1	Graphical representation of shunt voltage over voltage input across isotonic saline, used embalming fluid and fresh embalming fluid	32
Figure 3.1.2	Graphic representation of percentage increase in shunt voltage against voltage input in regards to isotonic saline, used embalming fluid and fresh embalming fluid	33
Figure 3.1.3	Graphical representation of oscilloscope data for current application to isotonic saline solution at 2kV charging potential	34
Figure 3.1.4	Graphical representation of oscilloscope data for current application to a used embalming solution at 2kV charging potential	35
Figure 3.1.5	Graphical representation of oscilloscope data for current application to a fresh embalming solution at 2kV charging potential	35
Figure3.2.1	Long exposure photographs of observed flashing before (A), during (B) and after (C) current application	36
Figure 3.2.2	Before (A) and after (B) photographs indicating extent of singeing on one of the bone	37
Figure 3.2.3	Long exposure photographs of a sample that exhibited a bight current flash-over, before (A), during (B) and after (C) current application	38
Figure 3.2.4	Long exposure photographs of the specimen before (A), during (B) and after (C) current application	39
Figure 3.2.5	Long exposure photographs of specimen before (A), during (B) and after (C) current application	40
Figure 3.2.6	Long exposure photograph of 10kV current application on tape covered sample	40
Figure 3.2.7	Photograph of the tape enveloped specimen post current treatment	40

Figure 3.4.1.1	Graphical representation of mean fracture area against charging potential highlighted for fracture type	50
Figure 3.4.1.2	Graphical representation of mean fracture length and perimeter against charging potential	51
Figure 3.4.2.1	Scatterplot of the regression factor scores for PC1 against PC2 extracted from the individual fracture data set in the first purely continuous iteration and marked for mode of current application	53
Figure 3.4.2.2	Scatterplot of the regression factor scores for PC1 against PC2 extracted from the individual fracture data set in the first purely continuous iteration and marked for charging potential	54
Figure 3.4.2.3	Scatterplot of the regression factor scores for PC1 against PC2 extracted from the individual fracture data set and marked for mode of current application	56
Figure 3.4.2.4	Scatterplot of the regression factor scores for PC1 against PC3 extracted from the individual fracture data set and marked for mode of current application	57
Figure 3.4.2.5	Scatterplot of the regression factor scores for PC1 against PC2 extracted from the individual fracture data set and marked for charging potential	58
Figure 3.4.2.6	Scatterplot of regression factor scores for PC 1 and PC2 marked for fracture type for the individual fracture data set	59
Figure 3.4.2.7	Scatterplot of regression factor scores for PC 1 against PC 3 marked for fracture type for the individual fracture data set	60
Figure 3.4.2.8	Scatterplot of PC1 against PC2, marked for charging potential, for the total fracture data set's first iteration	62
Figure 3.4.2.9	Line graphical representation of fracture number per field of view against mean peak current	63
Figure 3.5.1	Photomicrograph of a representative field of view demonstrating average fracture widths (light microscopy)	65
Figure 3.5.2	Close view of three-dimensional reconstruction of a bone block after being scanned with µCT	66
Figure 3.5.3	Orthoslice of experimental sample demonstrating resulting from post current application µCT	66
Figure 3.5.4	Visual comparison of material densities of thin section µCT scans	67
Figure 3.5.5	Example of a transverse orthoslice extracted from a thin section µCT scan contrasted to the equivalent histologically acquired image	68
Figure 4.3.1	Thin sections of the experimentally heated bone samples (Brain, 1993)	76

List of Tables

Table Number	Title of Table	Page
Table 2. 1	Details of cadaveric sample pool	18
Table 2.6.1	Outline of resulting peak residual voltages and peak currents for each charging potential	28
Table 3.3.1A	Representative photomicrographs of unstained section photomicrographs	44
Table 3.3.1B	Representative photomicrographs of unstained section photomicrographs	45
Table 3.3.2	Representative photomicrographs of stained sections	46
Table 3.4.2.1	Eigenvalues, respective percentage of variance and cumulative percentages of variance for the first iteration of PCA for the individual fracture data set	52
Table 3.4.2.2	Principal component extraction with Varimax rotation and Kaiser Normalization of the individual fracture data set	52
Table 3.4.2.3	Eigenvalues, respective percentage of variance and cumulative percentages of variance for the first iteration of PCA for the individual fracture data set	55
Table 3.4.2.4	Principal component extraction with Varimax rotation and Kaiser Normalization of the individual fracture data set	55
Table 3.4.2.5	Eigenvalues, respective percentage of variance and cumulative percentages of Variance for the total fracture data set's first iteration	61
Table 3.4.2.6	Principal component extraction with Varimax rotation and Kaiser Normalization of the total fracture data set's first iteration	61
Table 3.4.2.7	Spearman's correlation test results on fracture number in the total fracture data set	63
Table 4.3.1	Comparative summary of electrical and thermal ultrastructure alterations	78

1 INTRODUCTION

1.1 A Brief Description of the Lightning Phenomenon

Lightning is a multidimensional rapid form of extremely vast charge transfer occurring in the atmosphere. This transfer in the majority of circumstances occurs with no ground involvement whatsoever (Rakov and Uman, 2003a). These types of lightning events are classified as intra-cloud, inter-cloud and cloud-to–air events. Of the remainder, in which lightning discharges involve the ground, four main types are documented: downward negative lightning, upward negative lightning, downward positive lightning, and upward positive lightning (Rakov and Uman, 2003a). These types of cloud-to-ground discharges are termed flashes. The most common type of flash is downward negative lightning, accounting for as much as 90% of all cloud-to-ground lightning, with the remaining 10% consisting mainly of downward positive discharges. The upward discharges are fairly rare and believed to occur mainly from objects standing at heights greater than 100 meters (Rakov and Uman, 2003a).

The downward negative lightning discharge process begins as negative charge accumulates in the lower portion of a cloud, effectively polarising the cloud due to the ground's comparative positive charge (Rakov and Uman, 2003b). Once the potential difference between the cloud and the ground has reached a high enough density, initial breakdown of the isolating nature of the internal area of the cloud and air occurs (Rakov and Uman, 2003b). Thereafter, charge begins moving towards the more positively polarised areas of the cloud-ground system (Rakov and Uman, 2003b). This results in a stepped leader of charge, which then propagates the breakdown by creating a primary channel of plasma, or ionised air, along its path (Rakov and Uman, 2003b). This stepped leader eventually connects with an upward streamer from a protruding object or individual, or the ground itself (Rakov and Uman, 2003b). When the leader and the streamer attach, a return stroke is observed in the form of the lightning flash, traditionally witnessed when viewing a lightning strike. This is termed a return stroke due to

the apparent direction of the flash coursing upwards while the charge itself dissipates through the channel downwards into the ground (Rakov and Uman, 2003b). The whole process of lightning attachment occurs over tens of milliseconds; the generation of a stepped leader occurs over approximately 20ms, whilst the actual first return stroke within the next 100 to 200μs and lasting approximately 100μs itself (Uman, 2001). Following first stroke completion, a lightning event may terminate. However, the majority of lightning discharges are composed of multiple strokes, ranging from one to 26, with an average of three to five full strokes (Hendry, 1993). Each of them is comprised of a dart leader and a return stroke functionally similar to the previously described stepped leader and return strokes but of lesser intensities (Hendry, 1993).

The intensities of the potential difference between cloud and ground have been shown to vary greatly, between -102 and +94 megavolts through experimental testing (Marshall and Stolzenburg, 2001), and from 50 to 500 megavolts when calculated from atmospheric observations (Rakov and Uman, 2003b). As this potential difference between ground and clouds increases, the probability of an upward streamer to induce further breakdown, also increases. Hence the possibility of lightning attachment increases at greater potential differences, especially from more projecting structures or individuals where the distance for charge transit is decreased (Rakov and Uman, 2003a).

The true current component of a lightning event is experienced in the return stroke, following lightning attachment, as the accumulated charge dissipates through the ionised gas channel into the ground (Rakov and Uman, 2003b). Hence, return strokes are believed to be the main force behind structural damage and individual injuries. The lower measured limit of a return stroke has been identified to be 2kA (Berger *et al.,* 1975). Peak currents for 95% of first strokes are above 14kA and only 5% range beyond 80kA (Berger *et al.,* 1975). In subsequent strokes, peak currents tend to be smaller, with 95% of them being over 4.6kA and only 5% releasing currents greater than 30kA (Berger *et al.,* 1975). The impulse current flow of the return stroke,

in certain cases, is followed by a weaker current within the range of hundreds of amperes sustained for ten to 100 milliseconds (Kitagawa *et al.* 1962). These continuous currents are believed to be the cause behind more severe extents of thermal damage in multiple structures, including powerlines (Nakahori *et al.* 1982), aircrafts (Reazer *et al.,* 1987), and forest fires (Fuquay *et al.* 1967, 1972).

It has been documented that during the return stroke process an excessive amount of heat is produced as the charge traverses the plasma channel so rapidly. This effectively superheats the plasma to temperatures as high as 30 000 K producing the customarily witnessed luminous radiation of lightning (Orville *et al.,* 1967). To allow for the extreme thermal energy dissipation, the creation of a pressure wave of over 10 atmospheres along the channel occurs, which forces a violent expansion of the plasma extending outwards in the form of a blast wave (Orville, 1968). As the energy level is dispersed, it leads to a lower intensity sound wave, audible at great distances as thunder (Orville, 1968).

Lightning is a more common event than many would believe; to understand lightning frequency the term flash density is used. Flash density is an indicator of the amount of ground flashes per square kilometre per year. Approximations based on real storm observations suggest a lightning flash density of 6 flashes/km^2/year worldwide (Brooks, 1925; Rakov and Uman, 2003). In South Africa this frequency is far more alarming, demonstrating a range of 10 to 15 lightning flashes/km^2 /year (Gijben, 2012).

Lightning has been known to create major hazards for humans, animals and structures alike (Jandrell *et al.,* 2009). Between these lightning risk areas, an estimated expenditure of R500 million rand annually is reported (Gill, 2008a). There are numerous documented cases of animal and human lightning injuries and fatalities, as well as of the destructive effects of lightning on structures (Wright and Davis, 1980; Mellen *et al.* 1992; Rakov and Uman, 2003; Gomes, 2012; Pfortmueller et al., 2012).

1.2 Mechanisms and Reported Lightning Injuries and Fatalities

Ever since Benjamin Franklin's experiments and his invention of the lightning rod in 1752 (Schonland, 1964), there has been an ever increasing focus on lightning protection both in research and commercial enterprises (e.g. Golde, 1977; Vance, 1980; British Standards Institute, 1992). Nevertheless, lightning strike associated deaths remain fairly common. According to recent estimates, roughly 24 000 lightning related casualties per annum are reported globally (Holle, 2008). South Africa reports lightning fatalities ranging from 1.5 to 8.8 per million of the population per annum (Blumenthal, 2005; Holle, 2008; Jandrell *et al.,* 2009). This however, remains most likely a grossly under-reported figure, as the large number of rural communities are poorly protected and poorly informed in terms of lightning risks, mechanisms and fatalities (Gill, 2008b). While lightning has a greater likelihood of attaching at the most protruding structures from the ground (Rakov and Uman, 2003a), in an urban environment, the saturation of tall structures and favourable pathways of conduction throughout these structures, essentially prevents direct injury in most circumstances (Rakov and Uman, 2003a). However, in rural areas with smaller structures and greater extents of flat land, an individual close to a minimally protruding object is more likely to be injured than an individual in an urban environment (Holle *et al*, 2005).

Misreporting of lightning injury often occurs due to a large number of factors. Transient rapid lightning events are not always identified as such. Eyewitnesses and victims may misrepresent incidents. This is particularly due to the lack of training and inability to define multiple lightning mechanisms, notwithstanding the traumatic nature of experiencing or witnessing such an event (Cooper and Holle, 2010). Victims have been reported to present amnesia and thus awareness and reporting of a lightning incident may be delayed, or in some cases, not provided at all (Cooper and Holle, 2010). Regardless of poor reporting, there remains a low number of lightning incidents that are investigated (Cooper and Holle, 2010). In South Africa this is primarily due to strained police resources with few experts in lightning detection and

injury investigation. Added to which, in South Africa, folklore around lightning may contribute to attribution of some mechanisms mistakenly.

There are six accepted mechanisms of lightning injury which include: direct strike, contact potential, side flash, ground current, upward streamer and blast wave concussive injury (Cooper and Holle, 2010). Direct strike consists of a lightning's return stroke directly attaching to an individual. This scenario is most likely to occur in an open area with no precautions for lightning protection having being taken (Cooper *et al.*, 2008). Direct strike, despite being commonly believed to be the most common mechanism of injury, is contrarily identified as accounting for only 3 to 5% of lightning injuries (Cooper and Holle, 2010). Contact potential, which accounts for 15 to 25% of lightning related injuries, consists of current transferred into an individual in contact with an object that is struck by lightning at a distance; such objects include most plumbing and electrical outlets or metallic objects strongly conductive of charge (Cooper *et al.*, 2008; Cooper and Holle, 2010). This occurs since a potential difference is generated between the structure struck by lightning and the ground. The victim's contact allows for a release of the charge through themselves and into the ground, resulting in injury (Cooper *et al.*, 2008).

Side flashes, conversely, can occur when lightning strikes a structure and does not traverse the structure entirely. This results in division of the current and a flash-over to an adjacent person (Golde and Lee, 1976). This has been reported to occur even from person to person (Cooper *et al.*, 2008). The prevalence of this mechanism of injury ranges between 20 to 30% (Cooper and Holle, 2010).

Ground current, representing approximately 40 to 50% of lightning injuries, occurs due to the imperfect non-homogeneous conductive properties of the earth. When lightning strike currents are transferred into the ground the specific resistances of its constituents pose a greater potential in certain locations (Cooper *et al.*, 2008; Cooper and Holle, 2010). In these situations,

as a current is travelling through the earth and encounters an individual along its dissipation pathway. It is modelled as the current travels through them due to the generated step potential of the individual's lower limbs' position. This effectively results in a secondary current pathway upwards along the lower limb positioned closer to the lightning strike, across the pelvic region and downwards, through the more distant lower limb, back into the earth (Gookin, 2010).

The remainder 10 to 15% of injuries are likely a results of a possibly underestimated mechanism of injury, upward streamers coursing directly through individuals (Anderson, 2001; Cooper, 2002; Cooper and Holle, 2010). Injury has been demonstrated to occur even if there is no direct attachment of a stepped leader on a person induced upward streamer, as these streamers carry significant amount of current in the ranges of several hundred amperes (Anderson, 2001; Cooper, 2002).

The sixth and most recently identified mechanism of injury consists of blast trauma induced by close proximity to the pressure wave of a lightning strike channel (Blumenthal *et al.*, 2012). This was suggested by the type of injuries traditionally reported in lightning circumstances. Blumenthal and colleagues actualistically tested the phenomenon using ballistic ordinance gel instead of bone tissue, and demonstrated signs of pressure induced trauma termed barotrauma (Blumenthal *et al.*, 2012). Prevalence of this newest barotrauma mechanism is not clearly understood yet due to its very recent discovery.

Research in post-mortem lightning death identification is traditionally dependant on soft tissue analysis (Hanson and McIlwraith, 1973) and has been primarily put forward in the form of case studies (e.g. Wright and Davis, 1980; Mellen *et al.* 1992). Soft tissue analysis has revealed that the extent of damage undergone by a specific tissue depends on the amount of resistance to current flow of the tissue. The first barrier encountered by a current is the skin which, when dry, has a relatively high resistance, yet intermediate when compared to other tissues in the body (Cooper and Cantrill, 1992). Due to this high resistance it can result in the current igniting

the skin, causing what is identified as electrical burns, in the attempt to penetrate the body. The least resistant tissue of the body is nerve fibres (Cooper and Cantrill, 1992). Additionally, all high electrolyte containing tissues (vascular and muscle) have a low resistance (Cooper and Cantrill, 1992). Therefore, a current is expected to go through them relatively effortlessly with minimal, if any, disruption. The most resistant tissues are bone, tendon and fat (Cooper and Cantrill, 1992). These resistances are further highlighted when simulated tests of tissue models are considered (Lee, 2015). In fact, charge density is primarily distributed among the most conductive components of a multi-tissue model system considered, namely the vasculature and muscle, as nervous tissue was not considered (Lee, 2015). When looking at the most resistant tissues, very little charge density is observed across them (Lee, 2015). These tissues, bone, fat, and tendon, could suffer some thermal damage similar to what is observed on the skin. It is thus important to consider the possibility of thermal alteration to the skeleton of a lightning victim. Forensic burnt remains analysis is strongly dependant on skeletal remains as well as soft tissue, as fire trauma to the skeleton is relatively well understood (Fairgrieve, 2008; Schmidt and Symes, 2008; Randolph-Quinney 2014a-b).

Bone undergoes a multitude of changes when exposed to fire, which is highly dependent on the state of the body. Firstly, in fleshed remains or a living individual, the fire begins thermally damaging the soft tissue, with the first signs seen as dehydration and superficial burns of the skin (Fairgrieve, 2008). This would then be followed by more in depth thermal damage on the underlying tissues and internal organs as the more superficial tissues are consumed by direct fire contact or retracted due to radiating heat induced dehydration (Fairgrieve, 2008). Either of these scenarios would lead to exposure of bone which then will suffer direct damage from the heat.

As bone material is exposed, it also dehydrates, losing firstly its physiologic water content and then the chemisorbed water from the bone matrix itself, demonstrating heat lines and heat borders of differing coloration as the retracting soft tissues expose the bones partially (Randolph-Quinney, 2014a). The now dehydrated and exposed bone will then start

undergoing organic component decomposition and deposition within the bone matrix, in the form of soot, giving it a blackened charred appearance (Randolph-Quinney, 2014b). In the burning process, the mineral matrix of bone then starts undergoing chemical changes and the actual structure of bone alters as the hydroxyapatite crystals undergo inversion and then fuse in a structurally weakened lattice, and giving bone an off white-grey coloration as it becomes calcined (Randolph-Quinney, 2014b). None of these changes have been identified or reported, to the best of our knowledge, in any lightning fatalities. This would hence suggest a different mechanism of injury, related to the short thermal spike occurring with the nature of rapid high intensity current passage.

Bone is reportedly defined as a material demonstrating piezoelectric properties (Fukada and Yasuda, 1957; Bassett and Becker, 1962; Wieland *et al.* 2015). Piezoelectricity is defined as the generation of an electrical field from mechanical stress on a material (Skoog *et al.* 2007). Two types of piezoelectricity have been observed in bone: converse piezoelectricity, and inverse piezoelectricity (Fukada and Yasuda, 1957; Bassett and Becker, 1962). A conversely piezoelectric material would be defined as a material that is capable of producing mechanical stress induced electrical fields (Fukada and Yasuda, 1957; Bassett and Becker, 1962). An inversely piezoelectric material is defined as a material that demonstrates the opposite effect, namely the generation of mechanical stress on itself when placed within an electric field (Fukada and Yasuda, 1957; Bassett and Becker, 1962). These properties have been investigated more recently in terms of bone healing induction and acceleration in a small scale and small voltages (Wieland *et al.* 2015). However, the implications of these properties of bone have not been consider as mechanisms of injury to the best of our knowledge and may be considered suggestive of some mechanism of alteration to the bone structure induced by high voltage currents, when a sufficient amount of stress is exerted on the bone matrix.

Causes of death associated with lightning strike and electrocuted victims include ventricular fibrillation, cardiac arrest, respiratory arrest and asphyxia (Bernstein 1973; O'Keefe Gatewood and Zane 2004). These are also consistent with other accidental and naturally occurring

deaths, making them unreliable indicators for lightning associated deaths (Bernstein 1973; O'Keefe Gatewood and Zane 2004). Numerous forms of injury may occur in lightning and electrocution fatalities and include neurological trauma (Andrews, 2014), rupture of the tympanic membrane (O'Keefe Gatewood and Zane 2004; Blumenthal, 2005), arborisation patterns (Lichtenburg figures) (Bernstein 1973), unilateral or bilateral scapular fracture-dislocation combination (Kotak *et al.* 2000), fracture-subluxation of the first metacarpal (Kannan *et al.* 2004), shrapnel trauma (Blumenthal, 2005), and specific types of electrical burns, particularly at the soles of the feet (Lifschultz and Donoghue 1993; Blumenthal, 2005). Intermittent absence of electrical burns can further complicate manner of death identification (O'Keefe Gatewood and Zane 2004). Occasionally severe burns along the current's entry and exit sites have been observed (Pfortmueller et al. 2012). All these mechanisms are consistent with the short duration but high amperage of the current (Lifschultz and Donoghue 1993).

Overall, lightning fatalities are challenging to interpret and identify due to the various presentations of trauma (Blumenthal, 2009). Considering these limited indicators of lightning strike related death identification, complexity arises in correctly attributing manner of death without resorting to examining the individual's clothing or personal items for traces of related evidence, or relying on a witness report of the incident (Lifschultz and Donoghue 1993; Blumenthal, 2005). Hence, a holistic approach is ideally required to truly ascertain a lightning event and its victims.

Currently no criteria exist which allow for the recognition of lightning as a cause of death in cases of entirely skeletonized remains where no soft tissue can be scrutinized for evidence of lightning strike. In fact the effects of lightning passage on the skeleton have been largely ignored. From a forensic perspective this lack of research is problematic, especially so in South Africa, where a particularly high yearly lightning fatality rate exists (Blumenthal, 2005) particularly in the Highveld region (Holle, 2008). South Africa also has an exceptionally high

rate of unidentified bodies from natural and deliberate deaths, many of which are recovered in a skeletonised state from the veldt and other outdoor areas in both urban and rural contexts.

This study investigated the effects of lightning discharge on skeletonised human remains, providing associations between current and trauma, possibly facilitating assessment of mechanism and manner of death in cases of suggested lightning related deaths, where no other forensic evidence may be available.

1.3 Lightning Trauma Simulation and Identifiers of Microstructural Bone Trauma

In the course of my BHSc Honours we took to completion a proof of concept study (Bacci *et al.,* 2014) demonstrative of the disruptive nature of high intensity electrical currents on animal bone. A series of porcine bones were subjected to individual high voltage impulse currents, of approximately 15kA, via an impulse generator. A sample of a lightning struck giraffe was used as a primary analysis for baseline trauma identification. To allow comprehension of the results of this study a basic understanding of bone histology is required, hence a brief overview will be carried out here.

Bone tissue is macroscopically classified into two types, cortical and trabecular bone (Kerr, 2010). Since the observed micro-trauma in the aforementioned study was identified exclusively within the cortical bone (Bacci *et al.* 2014), solely that part of the bone matrix will be reviewed.

The outermost layer of osteoid is laid down circumferentially around the more internal bone matrix as a series of external circumferential lamellae (Kerr, 2010). Beyond the circumferential lamellae a multitude of tightly arranged, vertical cylindrical functional units, termed Haversian systems, is seen (Kerr, 2010). These are also commonly referred to as osteon units across all animal bone histology (Fig. 1.3.1). Individual osteons are comprised of a central canal, which contains a neurovascular bundle, surrounded by a sequence of concentric lamellae, each separated by a layer of collagen fibres arranged in a parallel manner (Mescher, 2009a). As the concentric lamellae of osteoid are laid down by osteoblasts, these cells become trapped

within the bone matrix in spaces termed lacunae. Now termed osteocytes and responsible for maintenance of the bone matrix, these cells extend projections through a network of canaliculi, necessary for extracellular communication and nutrient-waste exchange in a calcified matrix (Mescher, 2009a) (Fig. 1.3.1). Between the separate osteon units interstitial lamellae are visible. They are arranged in a relatively regular straight manner, separated from the osteons by a noticeably different mineral structure termed cement lines which surround individual osteons (Ross and Pawlina, 2006) (Fig. 1.3.1). Osteons are occasionally horizontally connected by transverse canals of similar diameter to the osteon canals (Ross and Pawlina, 2006) (Fig. 1.3.1).

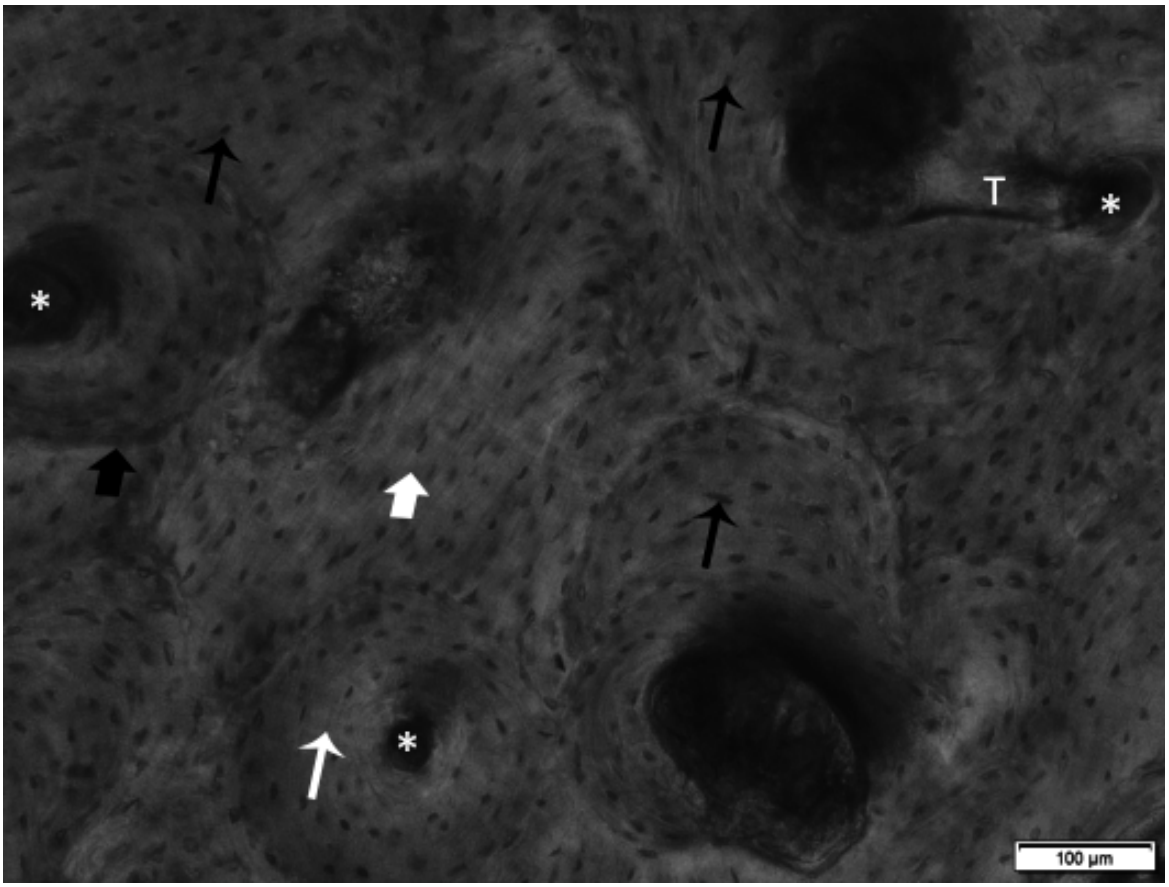


Figure 1.3.1: Example of Basic Human Bone Histological Structure

This photomicrograph demonstrates basic human bone histological structure. The image highlights osteon canals within osteon units (*), transverse canals connecting osteon canals (T), interstitial lamellae within the interstitial space between osteon units (wide white arrow). A single separation between two concentric lamellae is shown (thin white arrow), along with multiple osteocytes lying in lacunae (thin black arrows). The quite evident separation between osteons and interstitial lamellae histologically termed cement line is also highlighted (wide black arrow)

The overall bone matrix is composed of an organic and an inorganic component. This inorganic mineral component constitutes approximately 50% of the dry weight of a bone (Mescher, 2009a). The main mineral constituent of bone is hydroxyapatite crystals [$Ca_{10}(PO_4)_6(OH)_2$], as well as small amounts of non-crystalline amorphous $CaPO_4$ and other minerals (Mescher, 2009a). The organic component comprises bone cells (osteoblasts, osteocytes, and osteoclasts), collagen fibres as well as a multitude of ground substance constituting proteins such as proteoglycan aggregates and multiadhesive glycoproteins (Mescher, 2009a).

Animal bone varies to human bone in terms of histological structure, specifically in terms of osteon organization (Hillier and Bell, 2007). These differences were particularly identified within the samples of the previously conducted animal study (Bacci *et al.*, 2014). Porcine bone demonstrated an appearance of principally primary osteons, identified as bone laid down in initial development with little to no large scale remodelling, organised in broad circumferential layers (Hillier and Bell, 2007; Currey, 2013). Smaller areas of densely organised secondary osteons were also observed, identified as units of mature bone deposition replacing primary osteons during remodelling processes (Hillier and Bell, 2007; Currey, 2013). The structure of porcine and other ungulate mammals has been defined as a combination of plexiform and secondary osteons of medium breadth (Martiniakova, 2006). Plexiform bone is characterised as a rapid deposition of bone in a block or brick-like organisation (Currey, 2013). This histology profile is typically identified in adult animalsduals. Contrastingly, in juveniles, the bone matrix is composed mainly of lamellar bone, primary osteons and plexiform bone, with minimal secondary osteon presence (Hillier and Bell, 2007; Martiniakova, 2006).

The proof of concept animal study detailed a great variation of traumatic effects, both in a macroscopic and microscopic state. Superficially, areas of damage varying both in size and frequency were observed on the posterolateral aspect of experimentally tested bones. This was coupled with short term increase in temperature with occasional expulsion of liquefied

marrow from within the marrow cavity of the bone through the nutrient foramen (Bacci *et al.*, 2014).

Extensive fracturing and fragmentation of the bone matrix at the microscopic level associated with specific patterns of current flow through and between osteonic units within the bone cortex (Fig. 1.3.2) (Bacci *et al.*, 2014) were classified as:

- Circumferential micro-fractures around osteons
- Straight micro-fractures within interstitial spaces
- Extending micro-fractures propagating from transverse canals
- Radiating micro-fractures from within osteon canals

These findings warrant an in depth investigation based on human tissue; where in addition to histological analysis bone tissues were analysed through micro-focus computed tomography (µCT), a non-invasive and quantifiable method. This method has been considered of outstanding value for non-invasive fossil specimen analysis (Carlson *et al.* 2003), as well as for the quantitation and visualization, in a 3D model, of fractures (Vandersteen *et al.* 2003; Sellers *et al.* 2003).

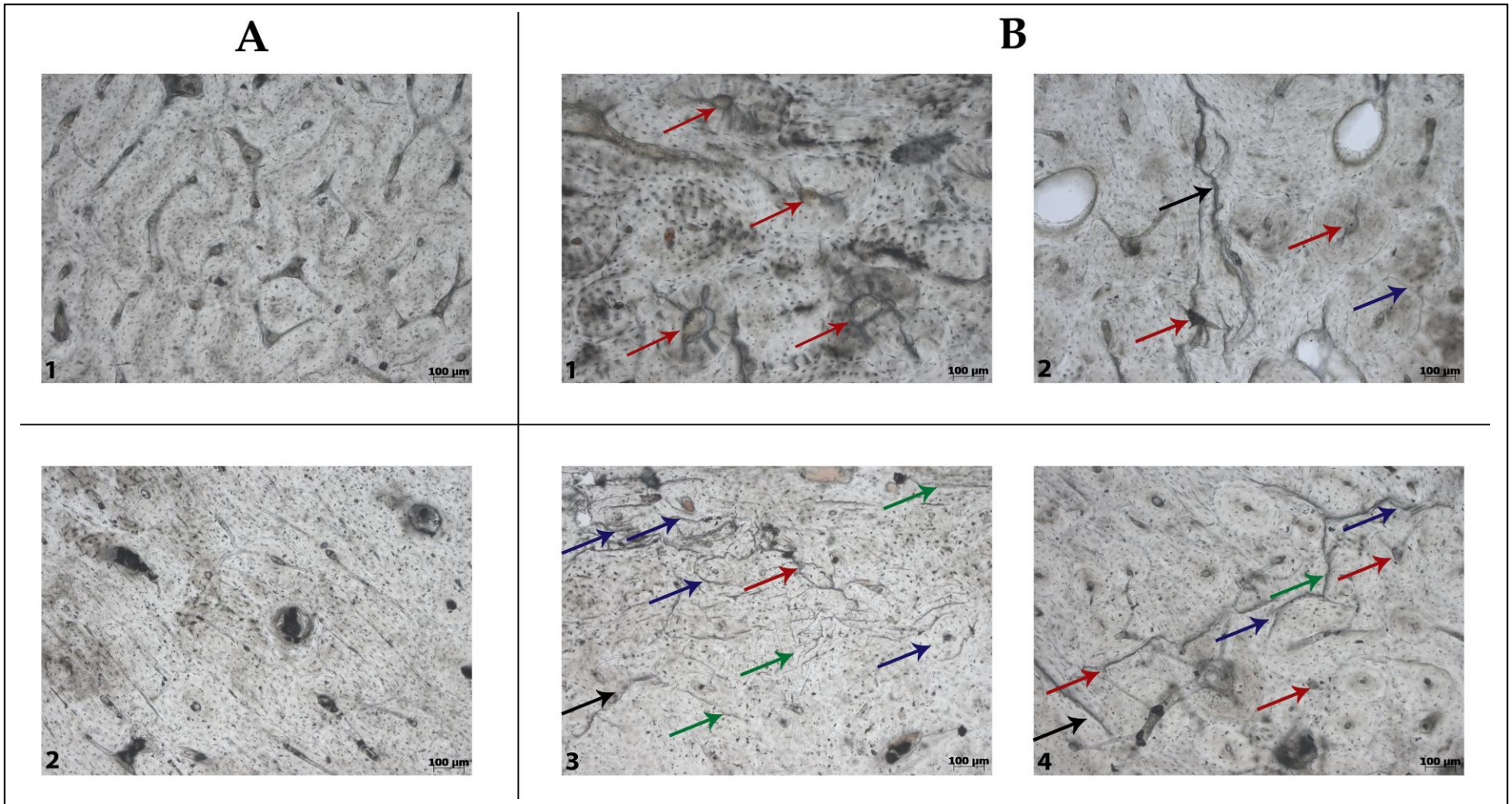


Figure 1.3.2: Comparison of control slides A1 (giraffe) and A2 (pig) to experimental slides B1, B2 (giraffe) and B3, B4 (pig) (Bacci *et al.* 2014)

B1 presents a characteristic pattern of outward radiating fractures from within the osteon canal (red arrows). B2 demonstrates some radiating fractures (red arrows), and an elongated fracture through multiple osteons (black arrow), as well as a single circumferential fracture around an osteon unit (blue arrow). B3 presents extensive disruption in the form of circumferential fractures around osteons (blue arrows), straight fractures through interstitial matrix (green arrows), radiating fractures (red arrow), and an extending fracture through a transverse canal (black arrow). B4 demonstrates radiating (red arrow), circumferential (blue arrows), and interstitial (green arrows) fractures.

1.4 Experimental Design Concerns

A constant concern in forensic anthropology, and particularly forensic taphonomy, is equifinality (Lyman, 2004). Equifinality is defined as a particular outcome being achieved as a result of multiple possible scenarios from different initial states (Bertalanffy, 1950). Commonly, multiple different taphonomic hypotheses can be identified as isotaphonomic either due to statistical reliability of a differentiating test or mistakenly, due to equifinality (Lyman, 2004). This translates into a great risk for accurate taphonomic interpretation, since a particular course of events may have resulted in a particular outcome, various and multiple scenarios could have created an identical taphonomic outcome. Hence, consideration of equifinality while attempting to understand and develop forensic techniques is of paramount importance.

Further concerns arise since all human cadavers used for research at the University of the Witwatersrand are embalmed, for prolonged preservation and teaching. It thus became necessary to investigate whether the electrical properties of embalmed tissue are markedly different, and to identify the limitations posed by the fixing agents. Embalming-induced alterations in bone have been investigated previously. Physical properties of animal and human bone between embalmed and unembalmed specimens were not significantly different in short term embalming procedures (McElhaney *et al.* 1964; Ohman *et al.* 2008). A greater amount of variation within samples than between them, was also noted (McElhaney *et al.* 1964; Ohman *et al.* 2008). Further unpublished research, carried out by Sutherland in 2009, demonstrated the lack of significant variation in regards to heat modification between embalmed and unembalmed animal bone. While it thus was expected that no significant differences should exist between embalmed and unembalmed hard tissues in regards to high intensity electrical stimulus either, embalming fluid properties were tested as part of this study to eliminate possible limitations created from the use of embalmed remains.

1.5 Aims and Objectives

The aims and objectives of this study included:

1. Characterisation of high energy electrical modification to human tissues.
    a. Observe patterns of electrical disruption on the gross human elements through macroscopic analysis followed by bone histomorphometry and histologic analysis of ground sections with characterisation and quantification of traumatic defects.
    b. Track, characterise, qualify and quantify changes in cortical bone in macro- and micro-structure using μCT and histomorphometry, to evaluate fracture formation and connectivity.
    c. Analysis, comparison, and evaluation of the μCT images and the corresponding ground sections.
2. Definition of the mechanisms of injury involved in bone micro-trauma within the experimental scenario.
    a. Defining the typology of induced micro-fractures.
    b. Identification of relationships between high voltage currents and induced trauma.

2 MATERIALS AND METHODOLOGY

Ethical clearance for this study was granted by the Human Ethics Committee under the waiver W-CJ-140604-1 for research conducted on human cadavers donated to the School of Anatomical Sciences, Faculty of Health Sciences, University of the Witwatersrand (Appendix G).

In brief, bone tissue was extracted from human embalmed cadavers (School of Anatomical Sciences, Faculty of Health Sciences, University of the Witwatersrand) and high amperage currents, of varying intensities, were applied via an impulse generator (High Voltage Laboratory, School of Electrical and Information Engineering, Faculty of Engineering and the Built Environment, University of the Witwatersrand). Additionally, embalming fluids were tested for their basic electrical properties under high voltage stresses and compared to isotonic saline. Bone samples were monitored before and after electrical treatment morphologically, with the use of micro-focus computed tomography (Radiology Unit, Nuclear Energy Corporation of South Africa) as well as histologically (School of Anatomical Sciences, University of the Witwatersrand). Micro-focus computed tomography (µCT) data was reconstructed and analysed three dimensionally with Amira 4.5.4. Histological and histomorphometric analyses were performed through photomicrograph acquisition using the CellSens 20 software. The electrically treated samples were compared to a cohort of untreated control samples.

2.1 Sample Acquisition

For the purposes of this study, the lower limbs of four cadavers were obtained from the School of Anatomical Sciences, Faculty of Heath Sciences, University of the Witwatersrand (Table 2.1). From each lower limb, both left and right, two bone blocks were extracted from the femur and two blocks from the tibia. The exclusion criteria consisted of bone elements modified by any previous surgical procedure or any signs of ante-mortem skeletal trauma. One of the

bodies presented ante-mortem trauma and a surgical implant for orthopaedic repair in the superior femur. As such, in that particular case, a block at the level of the proximal femoral diaphysis was impossible to extract, resulting in a total sample size of 31 blocks, 3 of which were randomly selected to be used as controls, while 6 blocks were reserved for future studies, leaving a total of 22 blocks that were used in the experimental procedure.

Table 2.1 Details of cadaveric sample pool

Shown here are each cadaver's respective age, sex, race, weight and height at death, in kilograms and metres respectively, as well as cause of death (COD). COD legend: Unk = Unknown; NC = Natural Causes; MI = Myocardial Infarction.

AGE	SEX	RACE	WEIGHT	HEIGHT	COD
92	F	WHITE	73	1.61	Unk
ca. 60	M	WHITE	58	1.84	NC
56	M	WHITE	81	1.87	MI
60	F	WHITE	41	1.67	NC

The femora and tibiae were extracted through manual dissection. In the anterior aspect, this was procedurally conducted by performing an oblique section immediately distal to the inguinal ligament. The underlying musculature was cut to expose the epiphysis of the femur, bringing into view the anterior ligaments of the hip joint. This allowed for a direct section through the iliofemoral and pubofemoral ligaments to anteriorly separate the femur from the acetabulum. Posteriorly, the iliac crest was palpated and a transverse section was performed along its margin. A sagittal section along the sacral part of the supraspinous ligament to the coccyx and circling around the labia majora/scrotum was then performed. The acetabulofemoral joint ligaments were then separated from the *os coxae* and the ischiofemoral ligament was sectioned to release the posterior aspect of the head of the femur. Lastly, the ligament of the head of the femur was cut to completely detach the femur from the acetabulofemoral joint.

The limbs were then de-fleshed via dissection, separating the femur and tibia from surrounding soft tissues. The de-fleshing procedure was carried out via a coronal section on the medial aspect of the thigh, cutting through the adductor muscles until the femur was reached.

Successively the muscles attaching to the posterior and superior aspect of the diaphysis were sectioned as close to the bone as possible without causing artefactual damage. The same procedure was carried out with the tibia, starting from the medial aspect with a coronal section all the way to the bone and procedurally severing all muscle attachments on the bone. The patellar ligament was severed from the tibia and left attached with the patella in it, on the quadriceps muscle. An initial section along the medial aspect of the thigh and leg was done. The medial collateral ligament was then cut, while the lateral collateral ligament was cut once the bones were extracted. Once both bones were entirely detached from surrounding soft tissues, the tibiofemoral joint was flexed to expose the cruciate ligaments and allow their sectioning. The tibiae were separated from the talus, following de-fleshing and disarticulation from the femora, firstly by sectioning the medial deltoid ligament in the medial aspect, across all four parts of it: anterior and posterior tibiotalar, tibiocalaneal, and tibionavicular. In the lateral aspect, a section following the shape of the lateral malleolus of the fibula was done through all three components of the lateral collateral ligament of the ankle, as well as the superior fibular retinaculum, effectively disarticulating the leg from the talus. The fibulae were separated from the tibiae by sectioning the proximal and distal, anterior and posterior tibiofibular ligaments, followed by a curved section tracing the lateral border of the tibiae across the leg to separate the interosseous membrane and ligaments.

From each de-fleshed femur and tibia, two 2cm cylindrical blocks, per bone, using an EXAKT 312 Pathology Saw, were extracted at the standardised lengths A, B, C and D irrespective of total bone length due to the lack of specific landmarks on the bone diaphyses not allowing a more standardised locale of extraction (Fig. 2.1.1). The pathology saw is routinely used to cut bone sections for pathological analysis and is unlikely to induce artefacts as it operates with constant water lubrication and uses a diamond encrusted blade to allow for smooth sawing of the bone material along the intended sectioning line. The aim of this study was to determine the absolute presence or absence of trauma and its patterns and morphology in relation to high voltage high amperage currents. Since variation between different bones, individuals and

ages was not part of its aims, and due to the limited availability of cadaveric material for this study, both femora and tibiae as well as the different extraction sites were grouped as long bone, bone blocks, effectively increasing the sample size of the study.

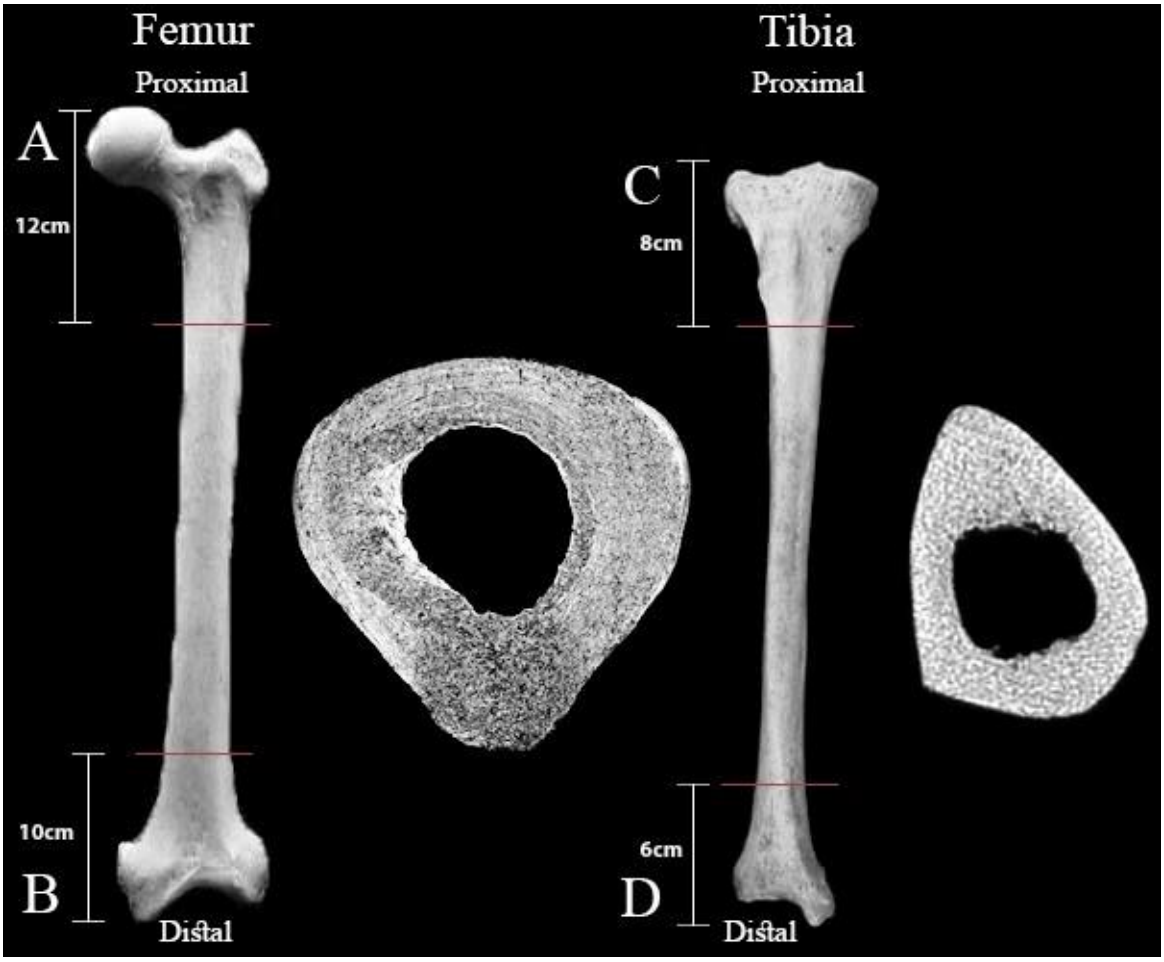


Figure 2.1.1: Schematic of bone block extraction from femora and tibiae

This schematic outlines the block extraction procedure post-dissection and pre-current application. The red lines indicate the levels of sectioning. The white bracketed lines indicate the standardised lengths labelled as A, B, C and D.

2.2 Electrical Testing Experimental Design

A high voltage impulse generator with the capacity to generate an 8/20μs impulse current of up to approximately 15kA was used for current application to the specimens (Fig. 2.2.1). The impulse generator (Fig. 2.2.2) (courtesy of the High Voltage laboratory, School of Electrical

and Information Engineering, University of the Witwatersrand) was assembled within the Human Identification Unit laboratory, School of Anatomical Sciences, University of the Witwatersrand. The 8/20μs impulse generator delivers the current with an 8μs rise, defined as the time necessary for accumulation of the peak charge, and a 20μs transmission time (Kind, 1978). The testing process was carried out according to predefined charging potentials, at 3.5, 4, 6, and 6.5 kV. These testing charging potentials were specifically selected, as in the trial experiments, higher charging potentials demonstrated significant amount of damage and concerns in terms of sample viability for the remainder analytical processes. Measurements of the peak voltage and peak current intensities, as well as its passage through the test specimens, were recorded through a GRS-6052A oscilloscope from GW Instek (Fig. 2.2.2). Peak voltage is defined as the peak of the residual voltage over the testing area following the electrical system completion over a particular trial, and it relates directly to the residual electric field over the testing area (Hauschild and Lemke, 2014). The peak current is defined as the peak effective current transferred through the testing material, usually as breakdown of the insulating nature of the material occurs (Hauschild and Lemke, 2014).

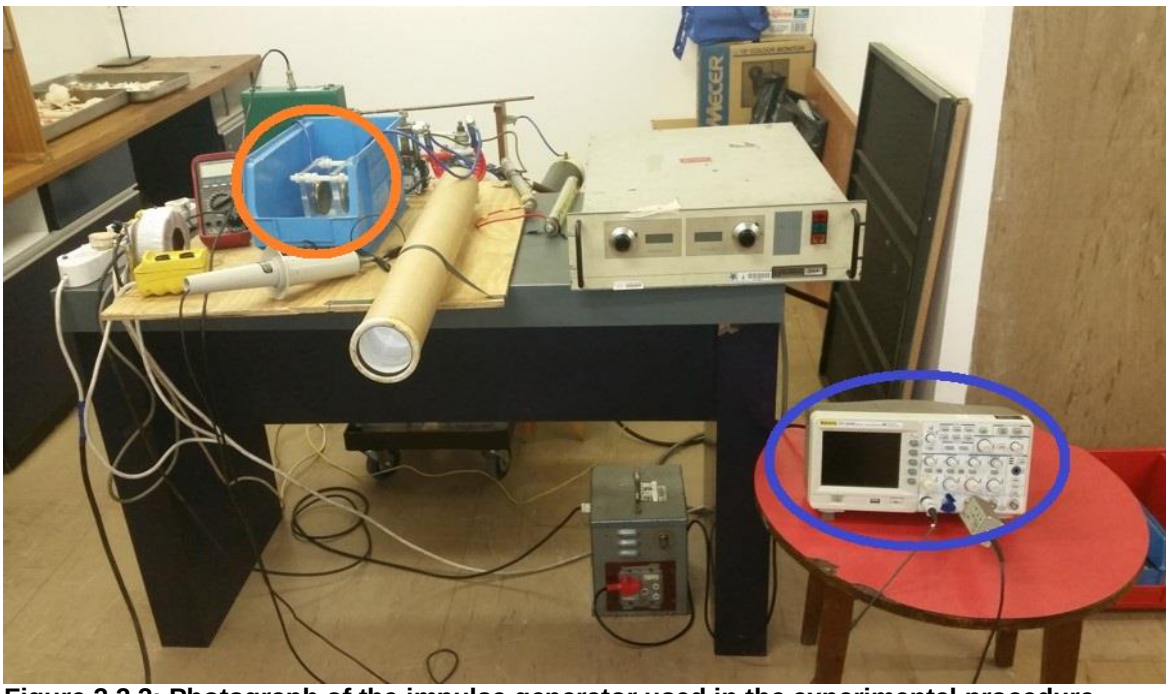


Figure 2.2.2: Photograph of the impulse generator used in the experimental procedure

This photograph shows the impulse generator with the oscilloscope a safe distance from the actual high voltage area, circled in blue, and the testing area circled in orange.

2.3 Fluid Electrical Property Testing

Firstly, since test samples were extracted from embalmed cadavers, a series of electrical tests were conducted to determine whether, and to what extent, used and fresh embalming solution conduct electricity when compared to baseline tests on an isotonic saline solution (fluid composition included in Appendix A). The solutions' pHs were firstly measured as an indicator of free H^+ ions. The electrical fluid tests were conducted identically to the 8/20μs impulse generator tests described above (section 2.2), except the fluids were contained in a 3cm total diameter (2.4cm internal) polymethyl methacrylate (Perspex©) tube sealed on both sides by brass cylindrical electrodes with a 1cm gap between the two electrodes, attached on the current exit side to a 10Ω shunt resistor (Fig. 2.3.1).



Figure 2.3.1: Photograph of the experimental design for fluid electrical property testing

Experimental design consisted of a test fluid filled Perspex© tube with sealing electrodes on either side, circled in orange, and a voltmeter attached to those electrodes to measure the voltage input into the fluid. On the right a wire connects the electrode to a 10 Ω shunt resistor, circled in blue, where a separate voltmeter measured the shunt voltage across it.

Based on these measurements the volume of fluid tested each time was approximately 4.52ml. The current was applied to the electrode distant from the shunt resistor so that the current had to flow across the fluid then through the resistor. The voltmeters over the electrodes and the shunt resistor yielded the voltage input in the fluid and the shunt voltage over the resistor once dispersed through the fluid, respectively. These measurements were then analysed to identify the resistivity of the fluids to current flow. Further tests were then conducted with an impulse current being applied to additional fluid samples and connected to

a GW Instek, GRS-6052A oscilloscope to measure and observe current intensity and the extent and trend of current passage through the fluids.

2.4 Bone Samples Current Testing Procedure

2.4.1 Provisional testing of current application to bone samples

A preliminary set of trials were conducted on five samples (n=5) to observe equipment functionality, adequate interaction between the bone and the impulse generator, and current passage through the specimens. The specimens used in this set of trials were selected randomly. Two different modes of current application were used which we termed parallel plate current application mode and wire-directed current application mode. In the first mode, parallel plate current mode (PPM), the samples were placed between the brass plates with the proximal aspect of the bone block directed at the current's entry point (Fig. 2.4.1.1). Different charging potential thresholds of 5kV (n=1), 8kV (n=2), and 10kV (n=2) were applied. Charging potential (CP) is defined for the purpose of this study as the approximate potential difference charged over the capacitor bank of the impulse generator prior to current application. It is commonly referred to as charging voltage in the context of impulse current testing (Schon, 2013). The positioning remained constant throughout all tests. A cohort of samples were experimented upon with the wire-directed current mode (WDM), consisting of an arrangement of 6 asymmetrically placed steel wire segments inserted below the cortex and within the trabecular bone matrix of the blocks, in order to direct the current in close proximity to the bone tissue, prior to placement between the parallel plates (Fig. 2.4.1.1). One specimen was covered with insulation tape superior to the cortex, while still permitting the cross-sectional surfaces of the bone sample to be in full contact with the brass plates on either side. These alternative methods of current application were trialled and used to direct the current through the bone itself, as the surface area of the plates was not fully covered by the bone's cross-sectional area, leaving the possibility that current would travel through the air rather than the bone.

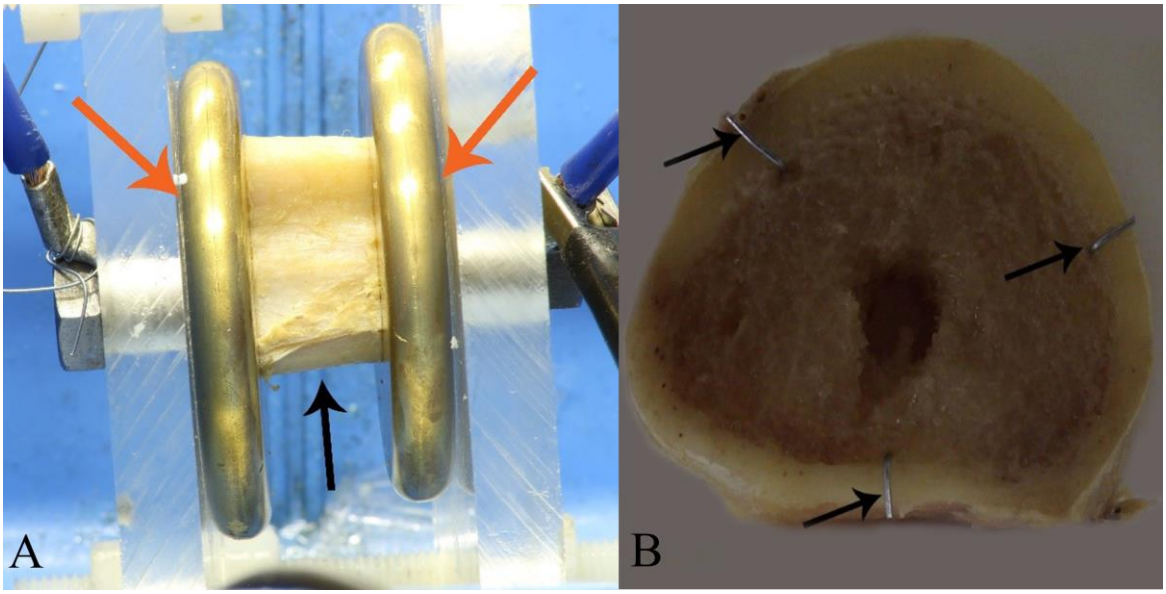


Figure 2.4.1.1: Photographs of parallel plate arrangement (A) and wire-directed for experimental current application (B)

In image A, brass plates (orange arrows) were arranged parallel to one another on a sliding Perspex platform tightened by plastic lug nuts. Bone specimens (black arrow) were placed in between the brass plates and held in place by tightening the sliding Perspex plates. In image B, steel wire L-shaped brackets (black arrows) were inserted immediately below the cortex within the trabecular bone matrix to assist current transfer through the bone samples, prior to positioning between the plates.

2.4.2 Parallel plate current mode

Parallel plate current application was carried out with a cohort of nine blocks (n=9). These bone blocks were placed flat between the brass plates (Fig. 2.4.1.1 A). The charging potentials tested were 3.5kV (n=3), 6.5kV (n=3), and 10kV (n=3) with three representative blocks, one from each of the younger cadavers, used for each discharge intensity.

2.4.3 Wire-directed current mode

For the wire-directed current application mode, a cohort of eight bone blocks was used (n=8). The testing method consisted of inserting six steel wire brackets, three on each side, directly internally to the bone cortex (Fig. 2.4.1.1 B), before placing the sample between the brass

plates for current application (Fig. 2.4.1.1 A). These wire brackets were inserted as a direct current pathway into the bone. For this set of tests the impulse generator was charged to 2kV (n=3), 4kV (n=2) and 6kV (n=3). Lower charging potential thresholds were used in this set of tests as opposed to the parallel plate of testing to preserve the integrity of the specimens, as trial tests using wire-directed current application caused extensive macroscopic damage and may have inhibited further microscopic analysis. Of all the iterations of current application these two appeared the most functional and likely circumstances in a real life scenario.

2.4.4 Photography of Experimental Current Application Procedures

During the experimental current application process the bone specimens were documented through eight second long exposure photography (Canon EOS 7D), to identify current attachment process and pathway. Prior to and following current application, the specimens were photographed in their unaltered and then electrically treated states in order to identify signs of macroscopic disruption.

2.5 Bone Block Processing

All 22 bone block specimens, as well as the three control specimens not subjected to an impulse current, were processed in the following manner. Four sections were obtained from each block (n=100) via sectioning with a high speed Clarke® CRT40 - 40pce rotary tool equipped with DREMEL® cut-off wheel No. 409. Following sectioning, mechanical removal of any remaining overlying soft tissue took place and the sections were stored in glass bijou bottles with distilled water. Sections were then manually ground down to usable thin sections on 220 grit waterproof carborundum paper while lubricated with 10-20ml distilled water as per Maat *et al*'s (2001) ground bone thin section method. During this process section thickness was monitored using light microscopy. Specifically, sections were suspended in distilled water to prevent dehydration and damage from the radiation of the microscope light source. Once the overall thickness of the section permitted resolution of histological features, the section

was rinsed thoroughly thrice in distilled water and placed in a fresh change of distilled water to prevent dehydration prior to staining or mounting.

Half of the thin ground bone sections (n=50) were then left unstained for visualisation of normally appearing bone histology and relative experimentally induced tissue disruption, while the other half (n=50) stained with a modified version of Goldner's trichrome stain. This version of the stain consisted of Methyl Blue as a mineral stain as opposed to Light Green, traditionally used in Goldner's trichrome (Sterchi, 2013). Furthermore, Orange G Molybdate which stains osteoid specifically, was excluded since it consistently disrupted sample clarity by forming crystals during the staining procedure.

The staining procedure was conducted on free unmounted ground sections. For all wash steps sections were placed within embedding cassettes and for staining and rinses sections were placed in 35ml polytop bottles on a Stuart Scientific roller SRT 1 for the required time. The staining process involved firstly washing the samples in running tap water for 15 minutes to remove any remaining debris from section grinding. Sections were then stained with stable iron hematoxylin for 1 hour. Samples were then washed under running tap water for 10 minutes, followed by one rinse in distilled water for 5 minutes. Sections were then quickly rinsed in 1% acetic acid for 15 seconds, stained in Fuchsin-Ponceau (appendix A) for 5 minutes then rinsed in 1% acetic acid for 15 seconds. Subsequently, sections were rinsed in distilled water for 5 minutes prior to rinsing in 1% acetic acid for 15 seconds and staining in Methyl Blue (appendix A) for 3 minutes. This was followed by a series of rinses in three changes of 1% acetic acid for 15 seconds each. Lastly, sections were rinsed in distilled water for 5 minutes and then left overnight in xylene to impregnate to facilitate mounting. Any form of quick dehydration was avoided as it was found to damage the surface of the bone.

Following staining, the sections were mounted, cover-slipped with Entellan©, and viewed using light microscopy to establish the extent and typology of electrically-induced damage to

tissue. Additionally, photomicrographs were taken of observed alterations to the bone tissue using an Olympus iX51 Inverted Microscope.

Generation of artefacts in the bone processing was considered and excluded based on the identification of particular types of artefactual fracturing within our previous study (Bacci *et al.* 2014). Those artefacts were induced in the process of section extraction at the edges of the section where the semi-circular sections were separated with leverage pressure and not by sectioning. That type of artefacts were concentrated solely on the areas of leverage driven separation and consisted of extensive multidirectional fragmentation of the edges of the sections. This was considered and hence the sections were observed at a level beyond the areas of the edges in order to attempt documenting only fractures relevant to internal damage, as well as by a different sectioning method whereby the section was bisected more efficiently with the rotary tool and not leveraged out of a block. Additional artefacts observed in the staining procedure were induced by rapid dehydration of bone sections and presented as superficial fracturing involving the entire section's surface. These were distinguished by other micro-fractures by their strictly superficial presence and the occurrence only after the dehydration step of the staining process. These were avoided by not dehydrating the stained sections but rather directly immersing them in xylene overnight prior to mounting. Also for the sake of avoiding interference from the staining processing, measurements were taken only in unstained specimens. Furthermore, control sections demonstrated virtually no fracturing indicating that artefacts were unlikely and controlled for.

2.6 Multi-disciplinary Histological Analysis

Firstly, a series of the most qualitatively significant images were taken and tabulated for observation. Qualitative assessment of micro-fractures allowed for the development of a classification system, observationally adapted from Brain's (1993) work on burnt bone analysis, where four different cohorts were identified based on shape, location, and appearance, and termed fracture typology (FT): circumferential, radiating, irregular, and circumferential irregular, and will be explained later. Additionally, for quantification of alterations, a set of 3 photomicrographs from each section with representative cohorts of charging potentials from both PPM and WDM specimens were taken. Due to time and laboratory constraints a representative sample of 15 blocks, including the 3 control blocks, were chosen for quantitative analysis. The charging potentials at which these selected blocks were experimented upon, included 3.5, 4, 6, and 6.5kV; table 2.6.1 outlines the resulting ranges of peak residual voltage and peak current.

Table 2.6.1: Outline of resulting peak residual voltages and peak currents for each charging potential

Each charging potential is tabulated here with their respective minimum, maximum, and mean peak residual voltage (pV) and peak current (pC).

Charging Potential (kV)	Minimum pV (kV)	Maximum pV (kV)	Mean pV (kV)	Minimum pC (kA)	Maximum pC (kA)	Mean pC (kA)
3.5	3.28	3.84	3.65	0	0	0
4	4.24	4.28	4.26	1.12	1.28	1.20
6	6.24	6.56	6.43	6.72	8.72	8.01
6.5	1.12	7.04	4.97	9.28	9.44	9.36

To standardise the imaging a manual multi-dimensional image acquisition (manual MIA) technique available on CellSense software (Olympus iX51, v. 10) was used to obtain a whole

slide image. Thereafter an overall length measurement was conducted and the entire section subdivided in tenths. Photomicrographs were thus obtained of the field of view at the first, the fifth and the ninth interval. Specific measurements were thereafter taken at these standardised locations. These measurements included the total bone area (TBA) defined as total observable bone area in a particular field of view and the number of fractures identified (FN). Furthermore 4 measurements were obtained from each individual fracture: the fracture area (FA), fracture length (FL), fracture width (FW), and fracture perimeter (FP). The FA was obtained by demarcating the outer borders of the fractures manually through the software's closed polygon measuring tool (Fig. 2.6.1). The FL was measured, using a polyline measuring tool, along the midline of the entire extent of individual fractures. The FW was measured using the arbitrary line tool at the approximate midpoint of the fracture. The FP was automatically calculated by the software when FA was manually measured.

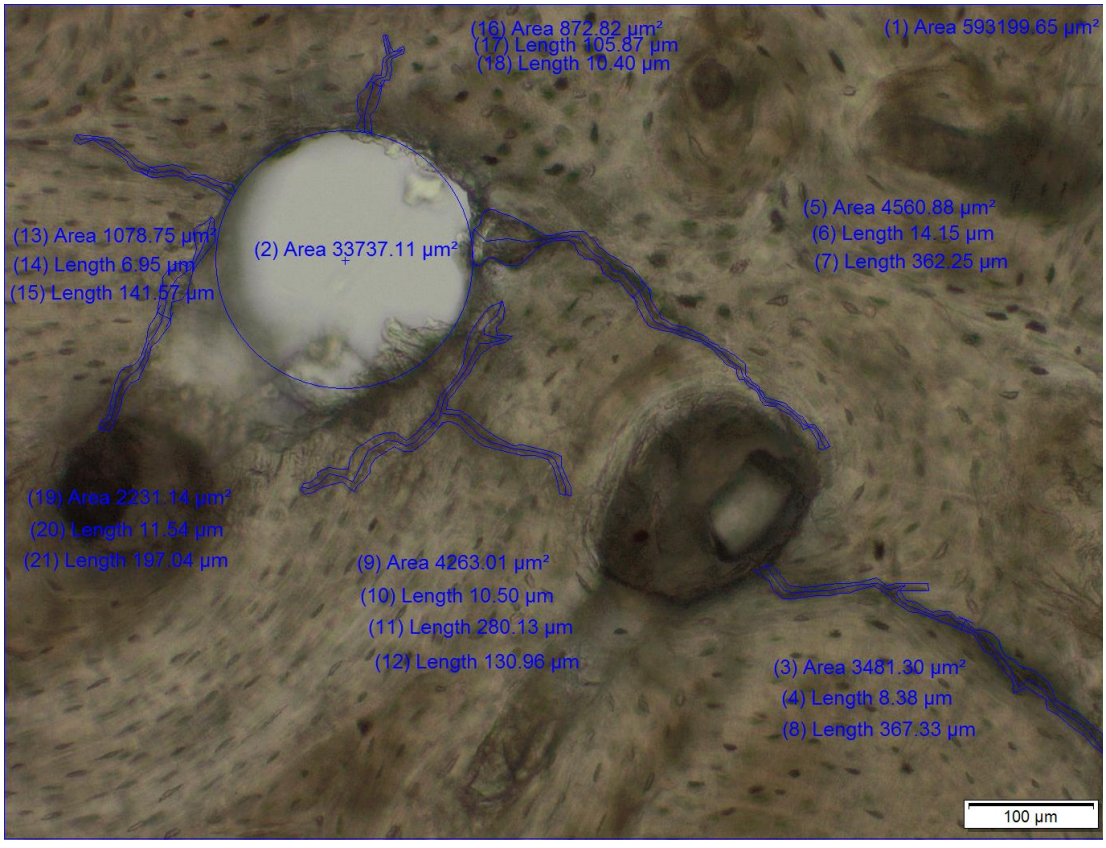


Figure 5.6.1: Example of fracture measurement procedure

Measurements of fracture length and area demonstrated for radiating and irregular fractures with perimeter calculated automatically from the closed polygon tool used to measure the areas.

Statistical analysis was done via Intra-Class Correlation tests for repeatability purposes, outlining both intra- and inter-observer error, carried out on SPSS (v. 20). Kruskal-Wallis ANoVA by ranks (KWA) was used to identify differences between micro-fracture dimensions and the factors responsible for the damaged observed, in terms of charging potential, mode of current application, peak residual voltage, and peak current. KWA was conducted on Statistica (v.12).

As part of the investigative process, Principal Component Analysis (PCA) was also conducted to allow dimension reduction for comprehension of hard to visualise multidimensional variables. PCA was employed to demonstrate trends by plotting the regression factor scores of the extracted components in scatterplots.

Difference of opinion exists amongst statisticians as to whether PCA can successfully accommodate categorical data (binary, scalar etc.) in conjunction with conventional continuous data (Andrews and Williams, 1973; Dryden et al., 2009; Harris, 1975). Standard PCA assumes linear relationships between numeric variables, and it is assumed that categorical variables are optimally quantified in the specified dimensionality, and as a result, nonlinear relationships between variables can be modelled. As PCA is really analysis of the eigenvectors of the covariance matrix it has been demonstrated that using mixed variables would yield results comparable to those obtained from a Multiple Correspondence Analysis (due to the fact that factor scores and eigenvalues are linearly related), but that results need to be interpreted with caution (as is the case in many applications of standard PCA) but are useful as a summarizing method (Harris, 1975).

Another option is to use Categorical Principal Components Analysis (CATPCA) which uses categorical variables applied to the correlation matrix (Linting and van der Kooij, 2012). However, CATPCA cannot accommodate continuous data in addition to categorical data, and as such this dissertation utilises standard PCA in two iterations –continuous alone, and continuous and categorical together in order to summarize and investigate the pattern of

variation within the experimental dataset, with appropriate comparison of the two sets of analyses, conducted on SPSS (v. 20). The iteration inclusive of purely continuous variables consisted of the fracture dimension data (FA, FL, and FP or TFA and TFA/TBA) as well as the peak residual voltages (pV) and peak currents (pC). Fracture width was not included in the statistical analysis as it was recognised an unreliable arbitrary measurement. The second iteration was inclusive of the same data, as well as three categorical variables: mode of current application (Mode), charging potential (CP), and fracture typology (FT). Lastly, a series of Spearman's Correlations were carried out (SPSS v. 20) to identify underlying correlations not visible in other aspects of statistical analysis.

2.7 Micro-focus Computed Tomography

The experimental and control bone blocks were assessed using a Nikon XTH 225 ST micro-focus computed tomography (µCT) scanner, based at the Nuclear Energy Corporation of South Africa (NECSA), prior and subsequent to current application, to detect anomalies in the three-dimensional tissue structure. The resulting pre- and post-current application µCT scans were then analysed using volumetric reconstruction software (Amira 5.4.5). Visualisation of fracture formation and electrically-induced shape distortion would have been done through preparation of volume rendered images with Amira (5.4.5). Additionally, through segmentation of the ultrastructure, it was envisioned that fracture orientation, width, area, volume, aperture, and variability in induced typology could have been visualised and measured. However, µCT resolution was unable to demonstrate any form of micro-fracturing, hence not allowing further three-dimensional analysis. The µCT resolution is directly dependent on scanned sample physical size as a larger sample requires a larger spread of the X-ray beam, thus a smaller sample would allow for a better resolution (Buzug, 2008). Due to this revelation, a second set of trial scans were conducted on five processed and mounted bone thin sections to attempt a better resolution with the possibility of allowing micro-fracture identification.

3 RESULTS

3.1 Electrical characteristics of embalming fluid compared to isotonic saline

The mean calculated pH values for the isotonic saline, used and fresh embalming solutions were 6.18, 5.20 and 2.80 respectively. The low voltage impulse current tests, demonstrated a reduced resistance to current flow in the isotonic saline when compared to the embalming solutions, both used and fresh. Delimitation of the resistivity of the fluids was important as it could potentially affect how embalmed bone reacted to the current, with a possibility of increased thermal disruption and a decreased electrical disruption. However, the used embalming fluid appeared to be slightly less resistant than fresh fluid. The measured shunt voltages, the voltages observed over a stock resistor with a defined resistivity of 10Ω, showed a consistent increase throughout all fluids; however, they remained considerably lower in both embalming fluids (Fig. 3.1.1).

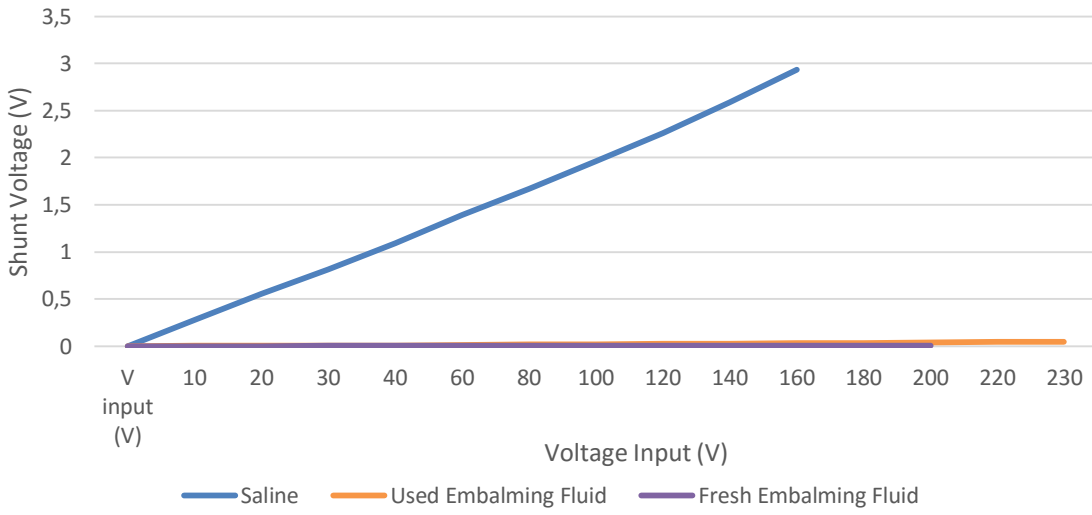


Figure 3.1.1: Graphical representation of shunt voltage over voltage input across isotonic saline, used embalming fluid and fresh embalming fluid

The shunt voltage increased steadily over the isotonic saline (blue), approaching almost 3V at a 160V input. Both used and fresh embalming solutions (orange and purple respectively), demonstrated a marginal increase over the higher ends of the voltage input. A maximal shunt voltage of 0.044V at 230V input was reached in the case of the used embalming fluid and 0.007V at 200V in the fresh embalming fluid tests.

The percentage increase in shunt voltage (PISV) was calculated, which demonstrated the increase of shunt voltage as a percentage of the previously observed shunt voltage value (voltage over the shunt resistor), summarizing the nature of the isolating properties of the material. The PISV consistently diminished as the voltage input escalated for all fluids (Fig 3.1.2). The isotonic saline resulted in a well outlined pattern of decrease in PISV with total voltage, hence the tests were interrupted at 100V. In the embalming fluids, PISV presented a slightly less consistent nature due to an incrementally slower corresponding increase of shunt voltage, but nonetheless appeared to taper out to a more consistent increase in extended higher ends of the test (Fig. 3.1.2). This occured particularly in the case of the fresh embalming fluid.

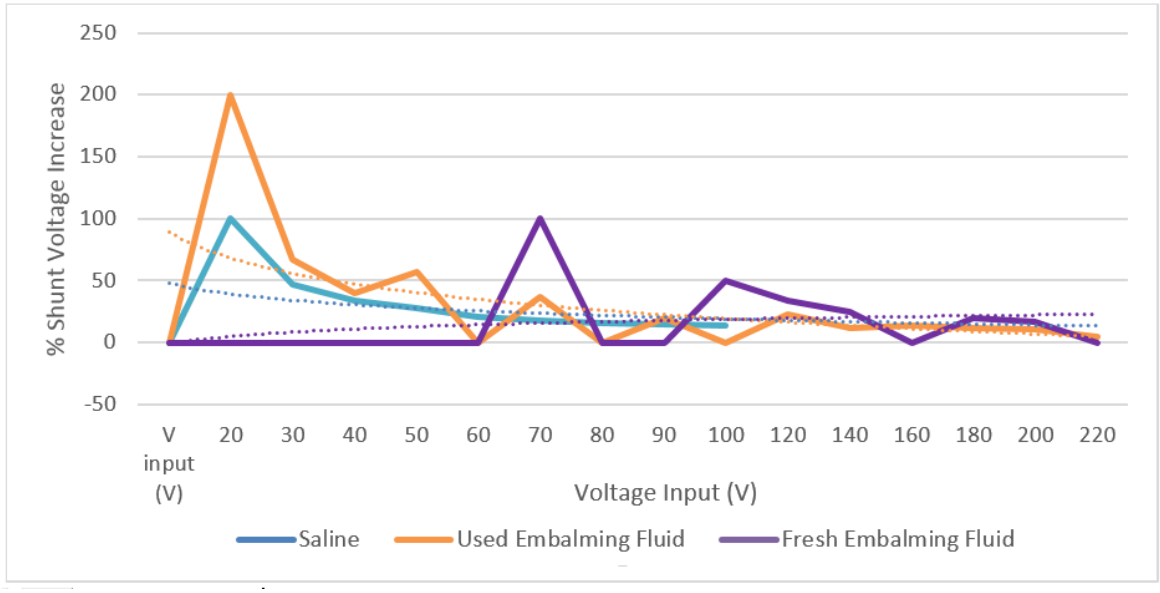


Figure 3.1.2: Graphic representation of percentage increase in shunt voltage against voltage input in regards to isotonic saline, used embalming fluid and fresh embalming fluid

Percentage increase in shunt voltage yielded a relatively similar pattern, with isotonic saline (blue), sharing a similar curve to used embalming fluid (orange), particularly observable in the respectively coloured dotted trend lines. The fresh embalming fluid (purple), appeared similar in nature however its trend line does not match the previously discussed fluids. This is explained by the delayed appearance of a shunt voltage due to its higher resistance.

The overall trends in shunt voltage percentage increase were relatively similar in the case of the isotonic saline and the used embalming fluid; however the fresh embalming fluid displayed a contrary trend. This was evidenced by the corresponding logarithmic trend lines superimposed in the graph in figure 3.1.2. This contradiction is present due to the delayed occurance of a voltage over the shunt, due to the increased resistivity of the fresh embalming solution.

A relationship was hence identified between pH and resistivity of the fluid, a low pH was consistent with a more current resistant fluid, as seen when comparing the pH of isotonic saline of 6.18, to the other solutions' 5.20 (used embalming fluid) and 2.80 (fresh embalming fluid). Further impulse current tests yielded oscilloscope data that revealed the current passage through these solutions. The current format was revealed in the shape of the graph, which demonstrates current passage through all fluids regardless of their resistivity as seen in figures 3.1.3 through 3.1.5.

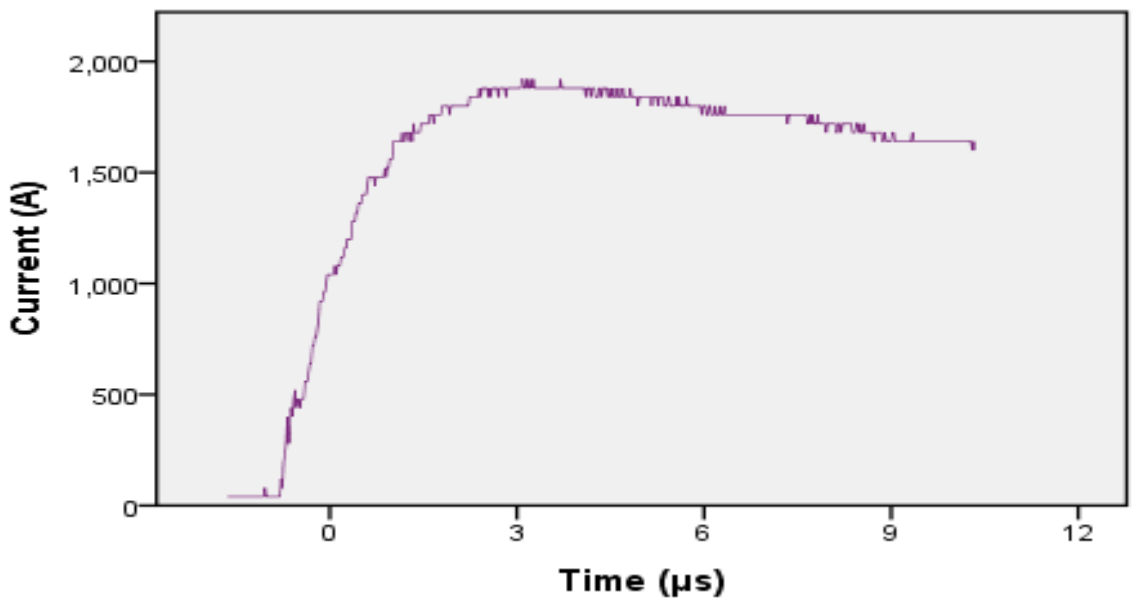


Figure 3.1.3: Graphical representation of oscilloscope data for current application to isotonic saline solution at 2kV charging potential

The line graph is given as a function of current (A) over time (µs) and demonstrates the pattern observable during current application on isotonic saline solutions resulting in current transfer through the fluid. This is shown here as a rapid rise of the current at time 0 and a slower release of the current through the sample captured by the oscilloscope up to approximately 10µs.

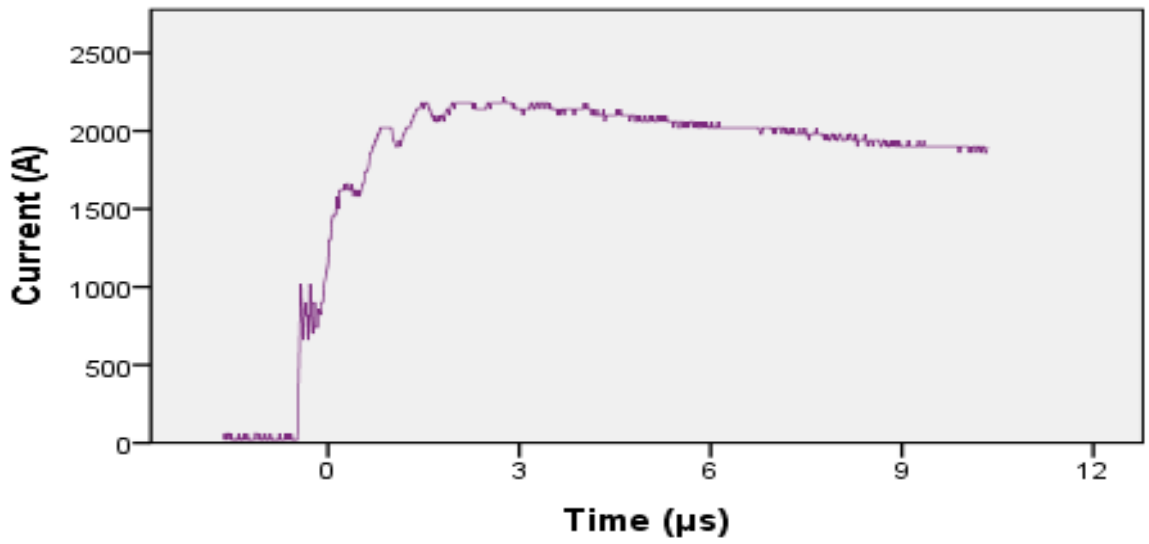


Figure 3.1.4: Graphical representation of oscilloscope data for current application to a used embalming solution at 2kV charging potential

The line graph is given as a function of current (A) over time (µs) and demonstrates the pattern observable during current application on used embalming solutions. This is shown here as a rapid rise of the current at time 0 and a slower release of the current through the sample captured by the oscilloscope up to approximately 10µs.

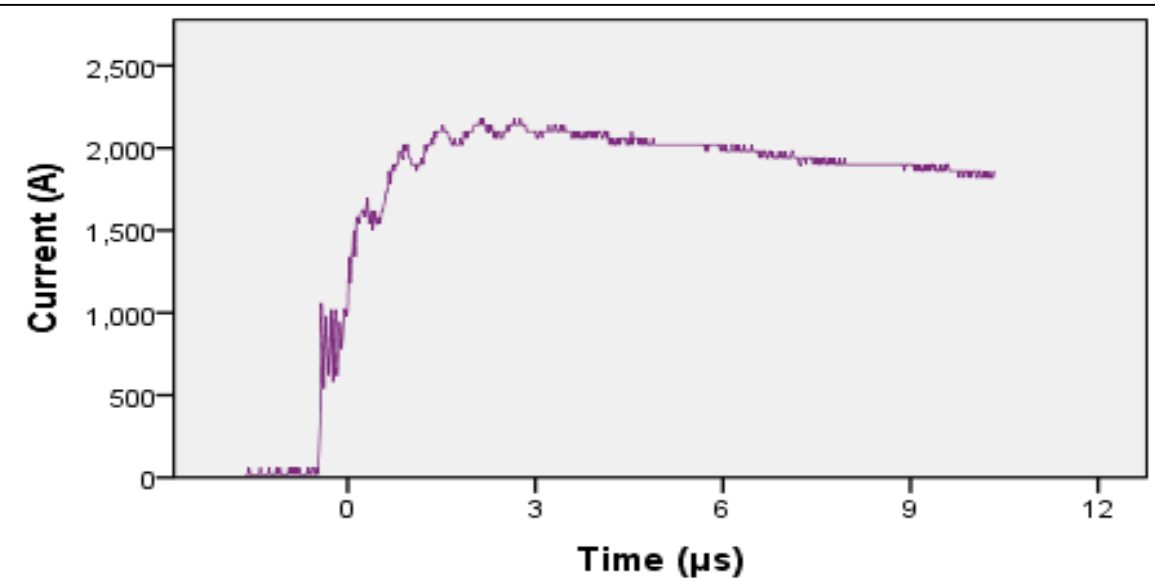


Figure 3.1.5: Graphical representation of oscilloscope data for current application to a fresh embalming solution at 2kV charging potential

The line graph is given as a function of current (A) over time (µs) and demonstrates the pattern observable during current application on fresh embalming solutions. This is shown here as a rapid rise of the current at time 0 and a slower release of the current through the sample captured by the oscilloscope up to approximately 10µs.

All data from the fluid tests are virtually identical in terms of current transmission and dissipation pattern. Demonstrating that high voltage impulse currents are able to traverse the indicated media regardless of their resistivity.

3.2 The Macroscopic Effects of a High Voltage Impulse Current on Bone

During both modes of current application tests, the long exposure photography captured the current flashing in the proximity of the plate to bone contact surface in eight specimens (Fig. 3.2.1 B). This resulted in an accompanying slight darkening and charring of the bones in the regions adjacent to the spark attachment (Figs. 3.2.1; 3.2.2). Singeing of overlying soft tissue and cortical bone borders was observed in these samples in the current application process (Fig. 3.2.2). This occurred over a greatly varied range of charging potentials (3.5 to 8kV) and different peak currents (0 to 11.5kA) and peak voltages (3.84 to 8.3kV).

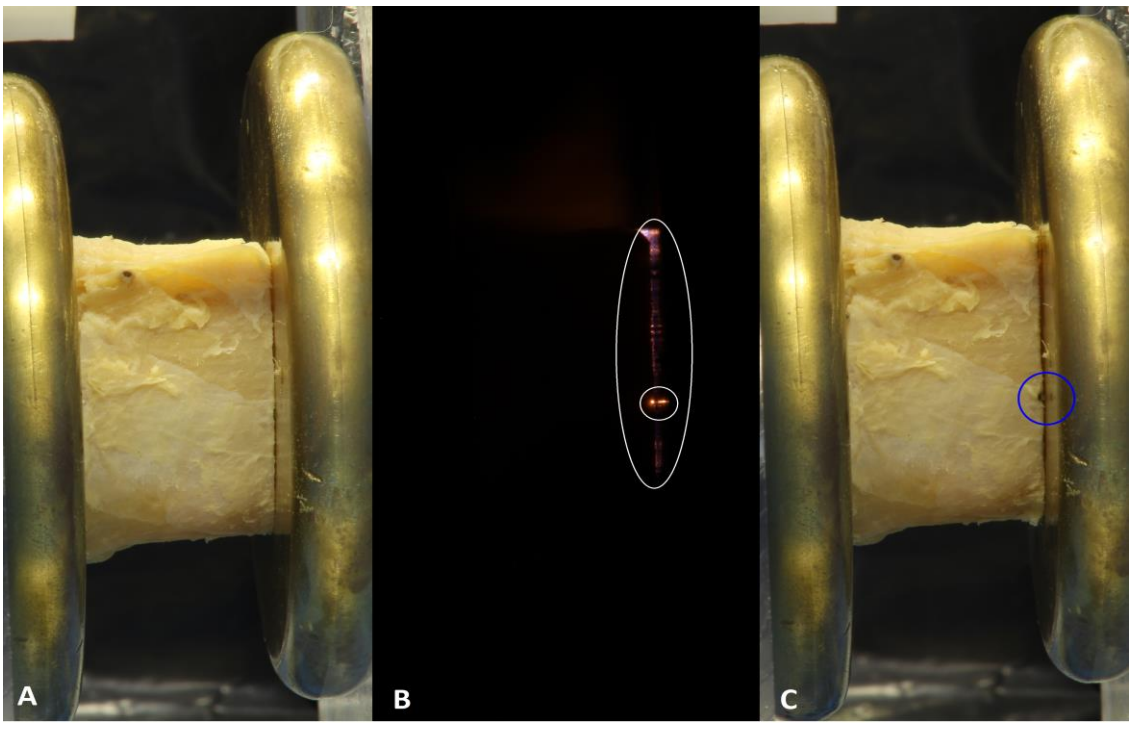


Figure 3.2.1: Long exposure photographs of observed flashing before (A), during (B) and after (C) current application

Image A shows the initial state of the sample experiencing a WDM current, image B demonstrates presence of sparking (white ellipse) as the current crosses the sample, and a brighter spark (white circle). The resulting singeing caused by the brighter spark (white circle) on the bone and soft tissues is outlined in image C (blue circle), displaying the post-current treatment sample.

In these cases it may be possible that the majority of the current discharged through the air, from plate to plate, without coming into contact with the bone specimens. However, in three of these specimens another form of damage was observed, as partial detachment of the residual soft tissue covering the bone. This appeared to occur in close relation with the current passage (Fig. 3.2.3). The current in the first two specimens was withstood by the isolating nature of the specimen and did not transfer through the specimen entirely. The other specimen presenting this type of damage was tested under a pV of 10.2kV with a generated pC of 14.4kA.

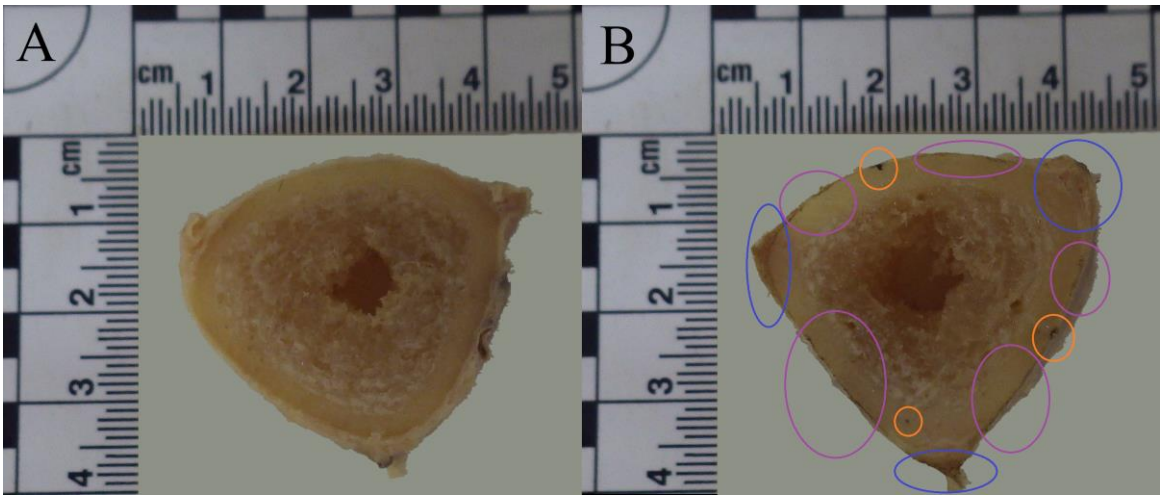


Figure 3.2.2: Before (A) and after (B) photographs indicating extent of singeing on one of the bone

Image A represents the sample before WDM current application and image B demonstrates the effect of the current on the sample. The purple ellipses highlight the areas of slight singeing occurring along the outer borders of the cortex, the orange circles indicate the points of attachment of the brighter sparks which resulted in a greater extent of burning and the blue ellipses demonstrating soft tissue singeing.

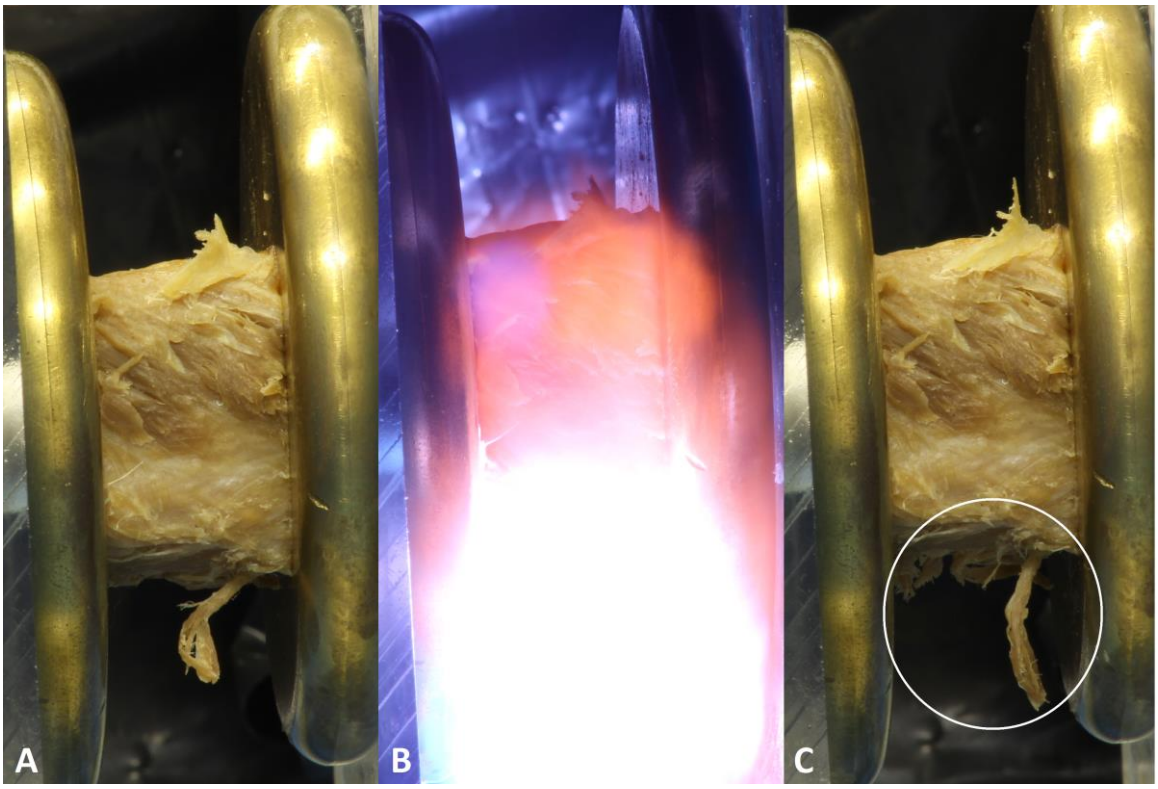


Figure 3.2.3: Long exposure photographs of a sample that exhibited a bight current flash-over, before (A), during (B) and after (C) current application

This sequence of images of a PPM treated sample, demonstrates the highly likely external passage of current in image B and the white circle in image C depicts the detachment and the damage to the muscle tissue overlying the bone in close proximity to the current flash.

Other than the above mentioned cases the majority of the specimens demonstrated no sign of macroscopic modification. However, during the testing process three out of twenty two bone blocks fractured on current application. One of the three samples, that experienced an impulse current through the WDM at 6kV charging potential, fractured longitudinally into two, almost equivalent in size, fragments (Fig 3.2.4). The peak voltage generated (pV) during the test was 6.24kV while the peak current traversing the bone (pC) was 6.72kA. A second sample, also experimented upon with WDM at 6kV burst into multiple fragments (Fig 3.2.5). During the test on this block the pV was 6.56 kV while the pC was 8.6 kA. It is worth noting that the metal wire elements were accounted for in both of the directed current tests, suggesting that the current did not react with the wire but rather with the bone itself.

Furthermore, the extreme fracturing occurred solely on specimens extracted from the oldest female individual. The only other specimen to present extreme damage was the unique sample in the preliminary tests that was enclosed in insulation tape and subjected to a charging potential of 10kV (Fig 3.2.6). This specimen appeared to explode upon current application with rapid disintegration and deflagration. The mechanism of this explosive event may have been the result of ignition of volatiles. Regardless of the precise mechanism this event resulted in the greatest extent of macroscopic damage. This is seen in the extensive fracturing of the sample in multiple small fragments and liquefying of most of the marrow (Fig. 3.2.7). The pV and pC for this test were not captured as they exceeded the expected testing range of the oscilloscope for this test.

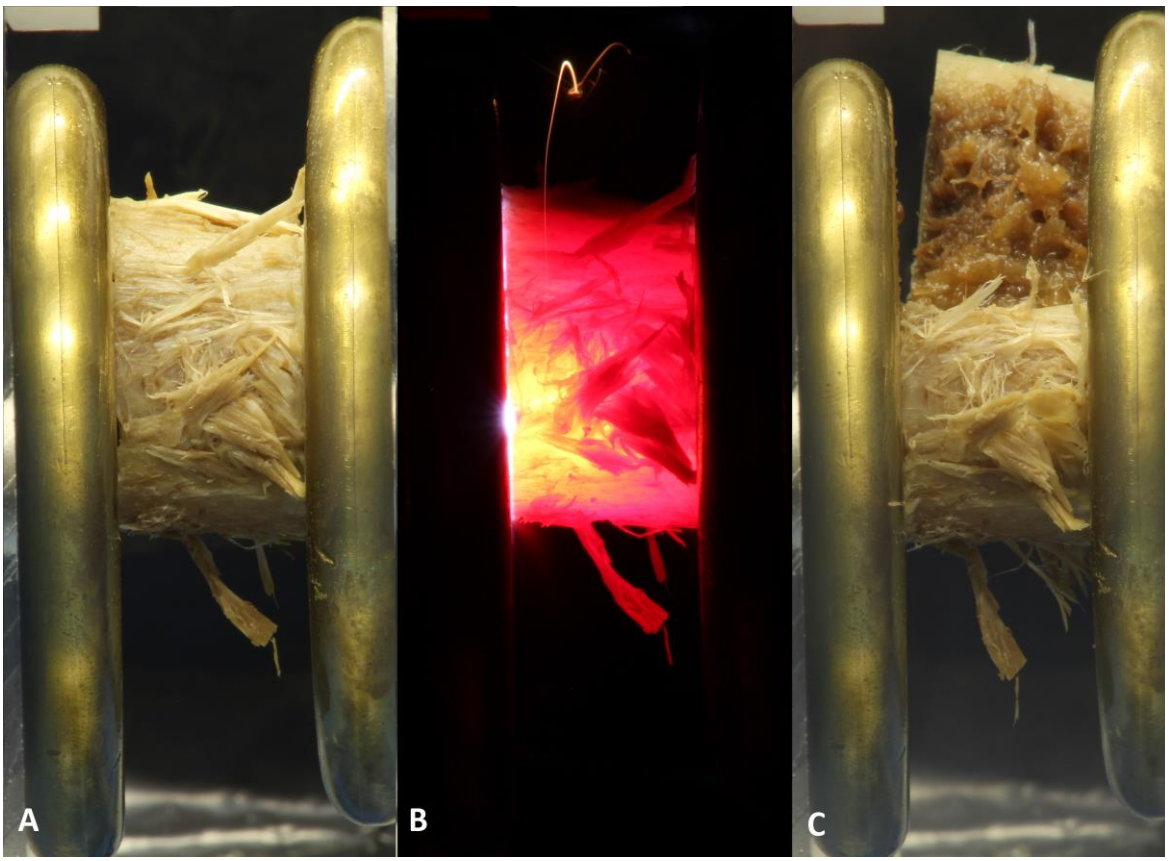


Figure 3.2.4: Long exposure photographs of the specimen before (A), during (B) and after (C) current application

Image A shows the sample prior to WDM current application, while the current passage becomes evident in image B by the bright flash internal to the bone block. Image C demonstrates the extensive instant damage experienced by the sample upon current application.

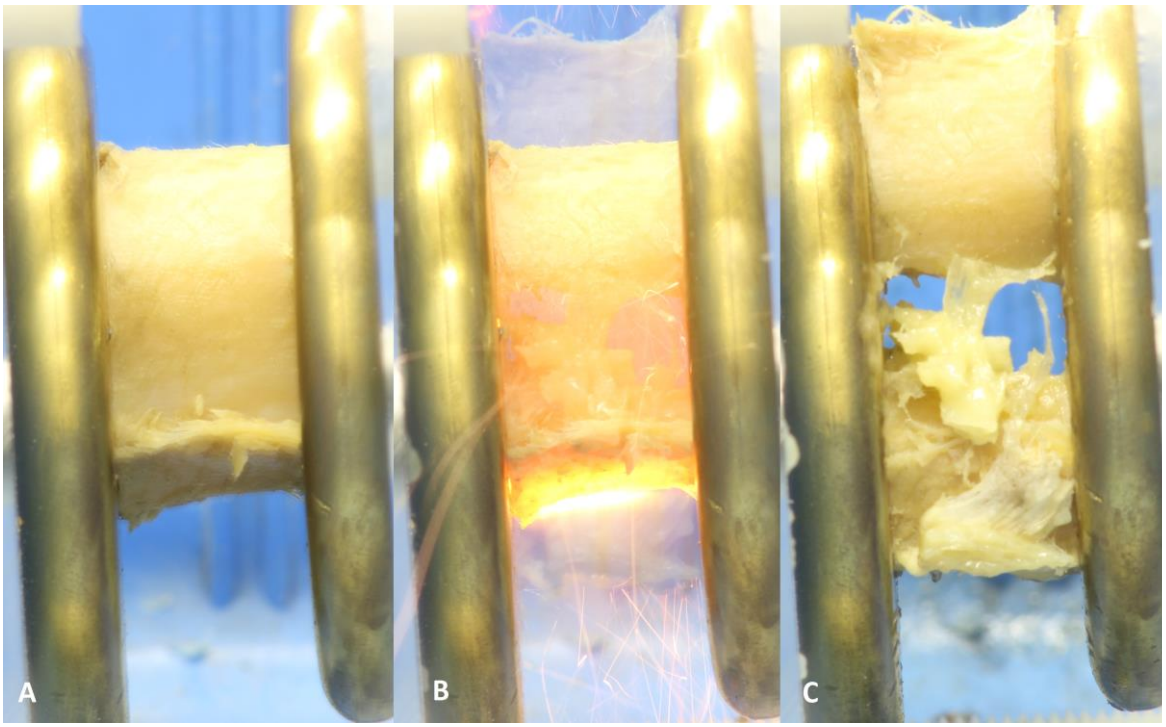


Figure 3.2.5: Long exposure photographs of specimen before (A), during (B) and after (C) current application

Image A displays the initial sample state, image B demonstrates WDM current passage and instant fragmentation of the sample while image C shows the resulting fragments held together by periosteum and any overlying connective tissue remnants.



Figure 3.2.6: Long exposure photograph of 10kV current application on tape covered sample

The current reacted explosively when confined within the bone by the insulation tape, resulting in ignition of volatiles.



Figure 3.2.7: Photograph of the tape enveloped specimen post current treatment

Sample clearly completely fragmented into multiple small pieces.

3.3 Qualitative Observations of Bone Microscopic Structural Modification

Qualitative assessment of photomicrographs led to the identification of a series of micro-fractures in sections taken from samples that experienced any form of current application, contrasting to control sections. The micro-fractures types were named according to their natures: short interstitial micro-fractures, radiating micro-fractures, circumferential micro-fractures, irregular unspecific micro-fractures and circumferential irregular micro-fractures.

Short interstitial micro-fractures are described as fractures that began and extended solely within the interstitial lamellae of the bone, usually being hardly visible and rarely curved. These fractures were identified in all current treated sections as well as the control sections originating from the older female individual, suggesting innate age related weakening of the mineral matrix of the specimens. These sections were thus excluded from quantitative analysis. The remaining fracture typologies were not observed in control sections and hence were considered as characteristic of current damage.

Radiating micro-fractures consisted of continuous fractures extending from the osteonic canal, usually in a straight or slightly undulating manner, on occasion extending beyond cement lines and joining other radiating fractures from neighbouring osteonal units. These fractures were observed in multiple sections; however, they were more extensive and better defined in samples experiencing a greater current and exposed to wire-directed current application (WDM) as opposed to parallel plate current (PPM).

Circumferential fractures consisted of short curved fractures initiating and extending within the concentric lamellae of an osteon unit, in certain cases running almost the entire length of the lamella. These micro-fractures appeared more consistently despite variations in mode of current application.

Circumferential fractures that extended beyond the concentric lamellae and further than the cement line were termed circumferential irregular. This type of micro-fracture appeared as often as circumferential ones but more commonly at higher current intensities.

Lastly, irregular micro-fractures consisted of any fracture that did not fit under the pre-defined parameters described previously, mainly consisting of elongated straight or stepped micro-fractures extending through cement lines, in between concentric lamellae but never through osteon canals. They were also mainly observed in specimens that had higher current intensities applied to them.

Bright field microscopy demonstrated micro-fracturing in the most unmodified and adequate way both in the case of stained and unstained sections (Table 3.3.1A and B). Polarised light observations appeared to create seemingly granular interference across the sections, making quantitative and occasionally even qualitative analysis difficult (Tables 3.3.1A and B). Control sections are shown first in Table 3.3.1A followed by a sample that experienced a 3.5kV charge with the parallel plate mode and demonstrates the radiating fractures observed particularly well, as they radiate outwards from within the osteon canals. Radiating micro-fractures are exemplarily demonstrated also in the sample that experienced a wire-directed current at 6kV (Table 3.3.1B). Circumferential fractures are well represented in both the sample that experienced a 3.5kV parallel plate charge as well as the one that experienced a wire-directed 4kV charge, as extending in between the concentric lamellae of osteon units. Circumferential irregular fractures are observed in the sample that was submitted to a 4kV charge, where circumferential fractures extend beyond the concentric lamella they began in. The sample that underwent a wire-directed current application of 6kV demonstrates a prominent fracture classified as irregular as it is inconsistent with other observed patterns.

Stained sections demonstrated presence and extent of micro fracturing more evidently than unstained sections. However, it evidenced a certain extent of surrounding micro fracturing and increased the perceived micro-fracture area (Table 3.3.2), making accurate and precise measurements for quantitative analysis difficult to obtain.

It needs to be noted that the images presented here were enhanced through the use of Photoshop CS6, to allow optimal contrast for detail presentation. The unstained specimen

photomicrographs were converted into greyscale, whilst the stained section photomicrographs were enhanced by increasing contrast and adjusting brightness to a uniform level across all images. The original pictures are included in appendix B.

Table 3.3.1A: Representative Photomicrographs of Unstained Section Photomicrographs

Each representative section is tabulated by charging potential applied to the particular block, as well as the mode of current application used. All images were obtained at 10x magnification and the scale bar depicts a range of 100µm. A photomicrograph under bright field and polarised light are demonstrated for the same field of view (FOV). Control microphotographs indicate no fracturing to any extent and demonstrate normal bone histology. At 3.5kV parallel plate current application some small radiating micro-fractures (orange arrows) are extending from an osteon canal. In the same images circumferential (blue arrows), and circumferential irregular (white arrows) micro-fractures are also observed. At 4kV wire-directed current application circumferential and circumferential irregular fractures are visible. The extent of disruption appeared greater in specimens subjected to WDM rather than PPM, even at comparable charging potentials.

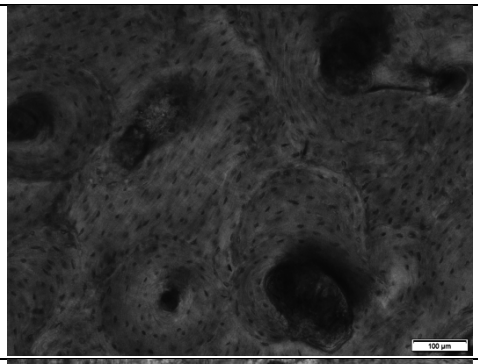
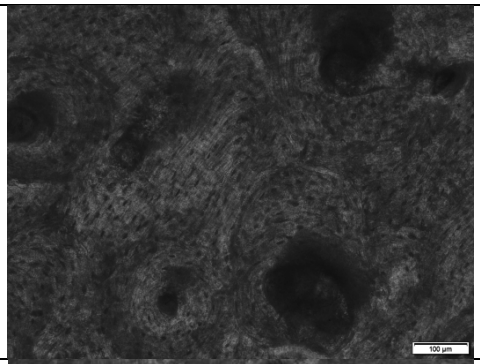
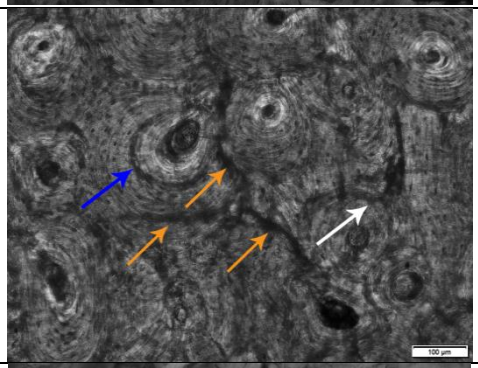
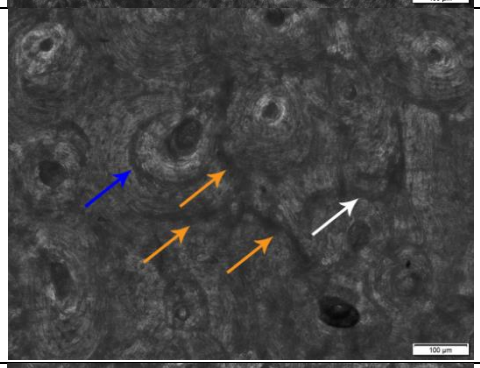
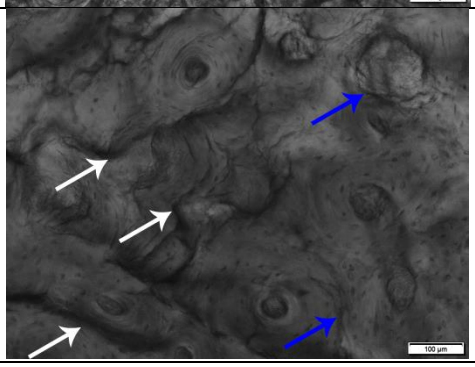
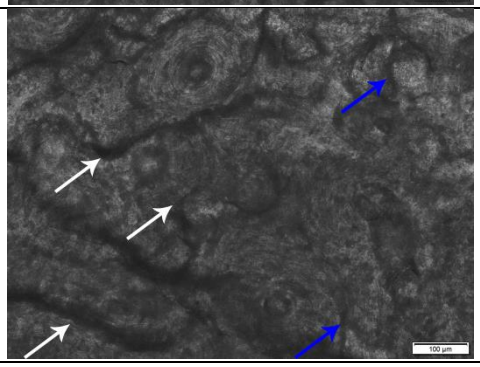
Charging Potential and Mode	Bright Field	Polarised Light
Control		
3.5kV Parallel Plate Current		
4kV Wire-Directed Current		

Table 3.3.1B: Representative photomicrographs of unstained section photomicrographs

Each representative section is tabulated by charging potential applied to the particular block, as well as the mode of current application used. All images were obtained at 10x magnification and the scale bar depicts a range of 100µm. A photomicrograph under bright field and polarised light are demonstrated for the same field of view (FOV).Distinct radiating micro-fractures are identifiable in the 6kV wire-directed current specimen. A greater extent of fracturing was observed at greater current intensities and through wire-directed current application, as evidenced by the increasing size and frequency of fractures and particularly irregular micro-fractures (magenta) at the 6kV wire-directed and 6.5kV parallel plate obtained microphotographs.

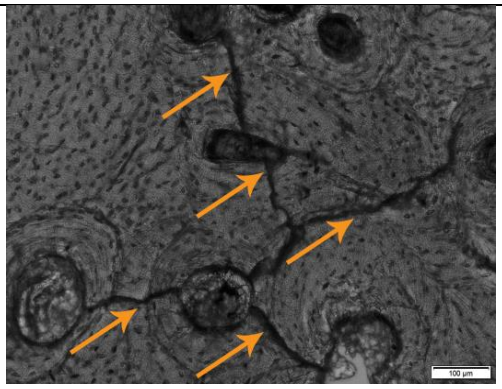
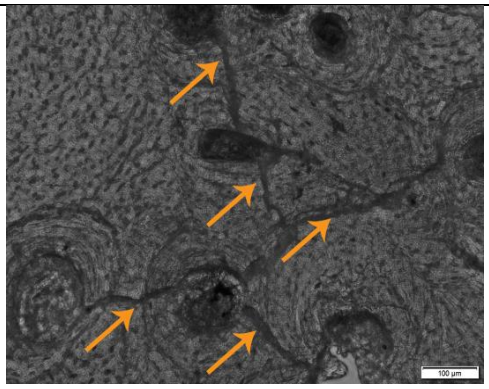
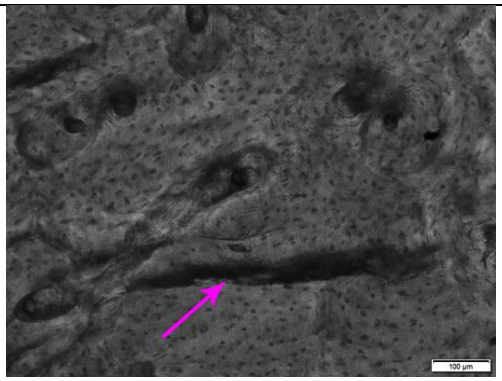
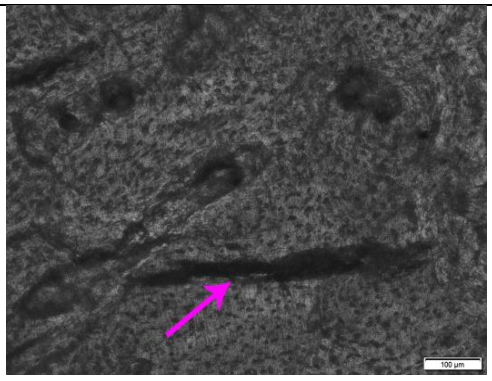
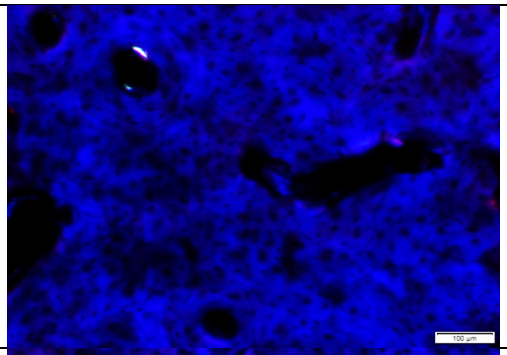
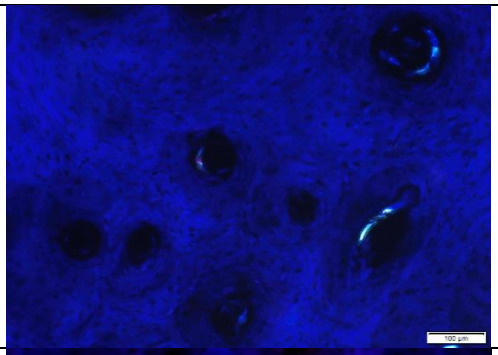
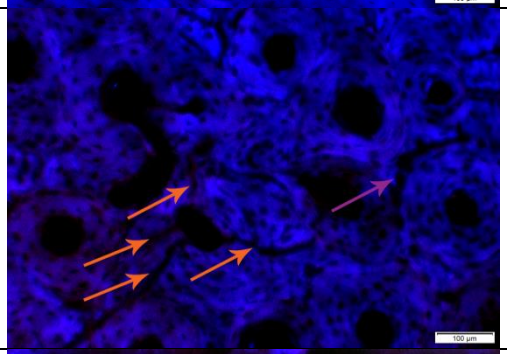
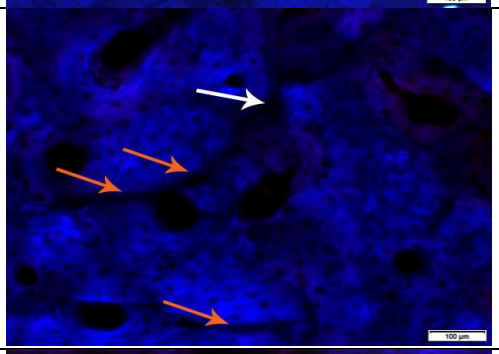
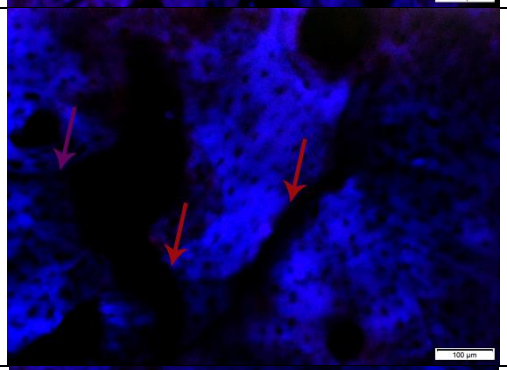
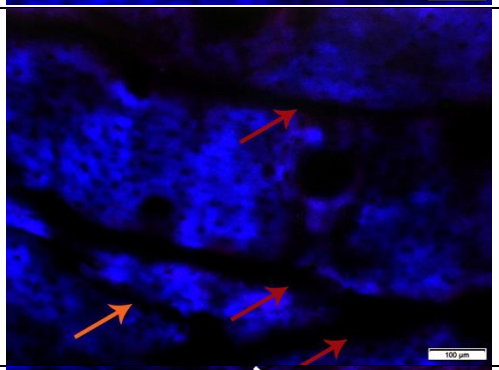
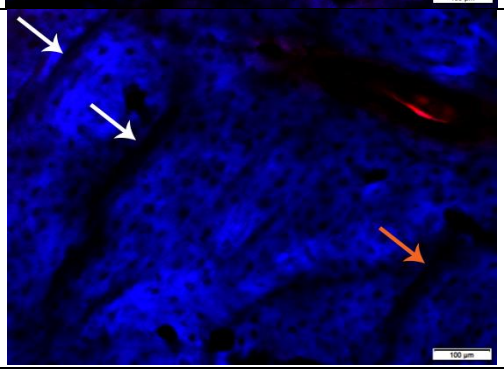
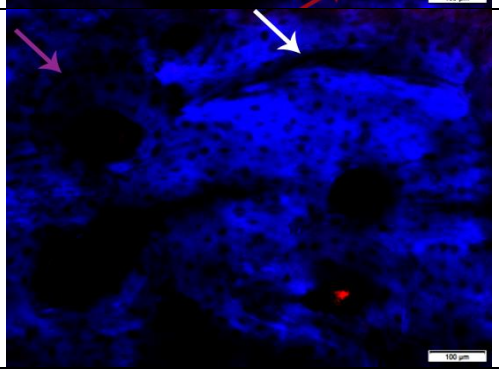
Charging Potential and Mode	Bright Field	Polarised Light
6kV Wire-Directed Current		
6.5kV Parallel Plate Current		

Table 3.3.2: Representative photomicrographs of stained sections

Each block is tabulated with the charging potential of that particular trial. Two photomicrographs under bright field are demonstrated for each stained specimen. All images were obtained at 10x magnification and the scale bar depicts a range of 100µm. The presence of fractures is highlighted here, despite the stain's increased difficulty in fine definition of detail in fracture sizes, the appearance of the fractures is more accentuated in stained samples. Radiating (orange arrows) and circumferential fractures (purple arrows) are observed across current intensities but more are evident at lower intensities; irregular (red arrows) and circumferential irregular (white arrows) micro-fractures appear with increased incidence at greater intensities.

Charging Voltage	First Photomicrograph	Second Photomicrograph
Control		
3.5kV Parallel Plate Current		
6kV Wire-Directed Current		
10kV Parallel Plate Current		

3.4 Quantitative Analysis of Microscopic Fracturing

Due to variable nature and statistical test requirements the data was split into two sets for statistical analysis. The first data set consisted of measurements and cohort classification according to individual micro-fractures. The second data set was comprised of the sum of all the micro-fracture areas (total fracture area, TFA) of each field of view (FOV) and the total number of micro-fractures present in each FOV. The two sets of analyses carried out will be hence referred to as either relevant to the individual micro-fracture measurements, or as pertinent to the total fracture areas. The descriptive statistics relative to the data analysed in the statistical analyses carried out are depicted in Appendix C.

Through a series of intra-class correlation tests measurement data was found to be consistent in terms of repeatability within a single observer, with statistical significance at a 95% confidence interval demonstrating a margin of accuracy ranging from a .861 lowest margin to a highest margin of 1.000, throughout all measurements. On the contrary, the accuracy of the measurements carried out by different observers was severely compromised by the lack of understanding of the nature and appearance of fracturing when compared to the natural histological appearance of bone. This is outlined by the fact that all measurement of fractures and their types do not correlate at all between observers, whilst the one measurement consistently evident and easy to identify, the total bone area (TBA), was accurately measured throughout observers, within a 95% confidence interval a lower boundary of .972 and a higher boundary of 1.000 was identified. The entirety of results of the repeatability tests are displayed in appendix D1 and D2.

3.4.1 Preliminary investigation of relationships between fracture measurements and controlled current outputs

The Kruskal-Wallis ANoVA (KWA) by ranks test was conducted on data obtained from individual fractures, grouped for: charging potential (CP) of the impulse generator for a particular trial, modality of current application (Mode), peak current transferred through the

specimen (pC), and peak residual voltage (pV) over the testing area after impulse current application.

When grouped for charging potential, significant differences were identified in fracture area (FA), fracture length (FL) and fracture perimeter (FP) (Appendix E1). Post-hoc tests were conducted to define the specific rank significant differences outlined by the KWA. These tests demonstrated the differences localized over CP of 4kV and 6kV, applied via wire-directed current application (WDM) for FA and FP (Fig. 3.4.1.1 and Fig. 3.4.1.2). Specifically, a CP of 6kV induced a significant increase in damage observed as delineated by FA and FP as opposed to CP at 4kV. In the parallel plate current application mode (PPM), no significant differences were found between variables and any of the CPs. The identified differences observed in WDM samples suggest a relationship between extent of damage and CP that is not readily evident in samples exposed to the parallel plate current mode.

Notably, differences were also identified between modes. Specifically, FL and FP were both significantly greater in 3.5kV (PPM) samples than in 4kV (WDM) samples (Fig. 3.4.1.2).

When considering the fracture type, it is important to note that there is no presence of circumferential irregular fractures in the 4kV WDM tests. The greatly reduced extent of fracturing (FA and FP) observed at 4kV signifies that as the charging potential increased the damage induced increased in the WDM group.

When considering the remainder of the KWA tests, with Mode, pV, and pC as the grouping factors, no other statistically significant differences were identified.

In the KWA analysis some variables (FW grouped for pC; FA and FW grouped for pV) yielded statistically significant results (H statistic); however, no differences were identified in the post-hoc analysis. This most likely occurred due to the high value of the H statistic, which measures the critical difference against which the standard deviation of the ranks are compared to in the post-hoc test *z'* scores to identify the differences (Chan and Walmsley, 1997). The large H value hence required a greater standard deviation difference between the ranks of the test to

classify a specific difference correctly (Chan and Walmsley, 1997). This is likely related to KWA tests not approximating the traditional Chi-squared distribution in small samples (defined as less than 5 entries per grouping variable) (Chan and Walmsley, 1997). This results in a severely decreased amount of degrees of freedom for the test and a decreased reliability on suppositions derived for those particular groupings (Chan and Walmsley, 1997). Hence, since data entries for each of the pC and pV groupings consisted of three for each group since three field of views were taken from each block, the resulting inconsistency between the KWA and the post-hoc test, was to be expected. The full tabulations of the individual fracture data set KWA results can be found in Appendix E2. KWA analysis conducted on the total fracture dataset revealed no statistically significant differences throughout the different groupings (Appendix E5).

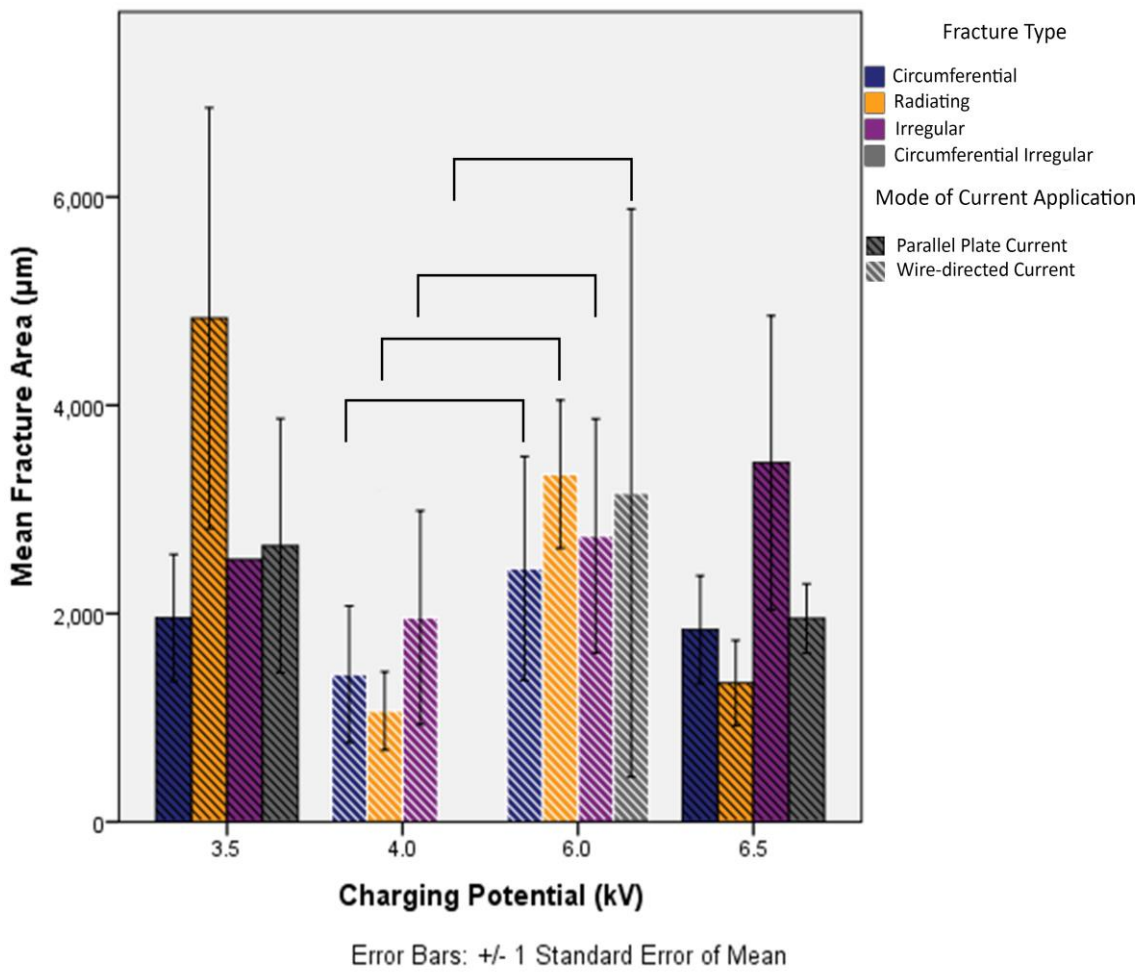


Figure 3.4.1.1: Graphical representation of mean fracture area against charging potential highlighted for fracture type

This bar graph demonstrates the significant differences identified for fracture area between charging potentials of 4kV and 6kV (overbar brackets). As the mode for both potentials was wire-directed, a greater weight on the CP intensity is suggested in WDM versus PPM. Noteworthy is also the lack of circumferential irregular fractures at 4kV, as well as the severely decreased extent of fracturing.

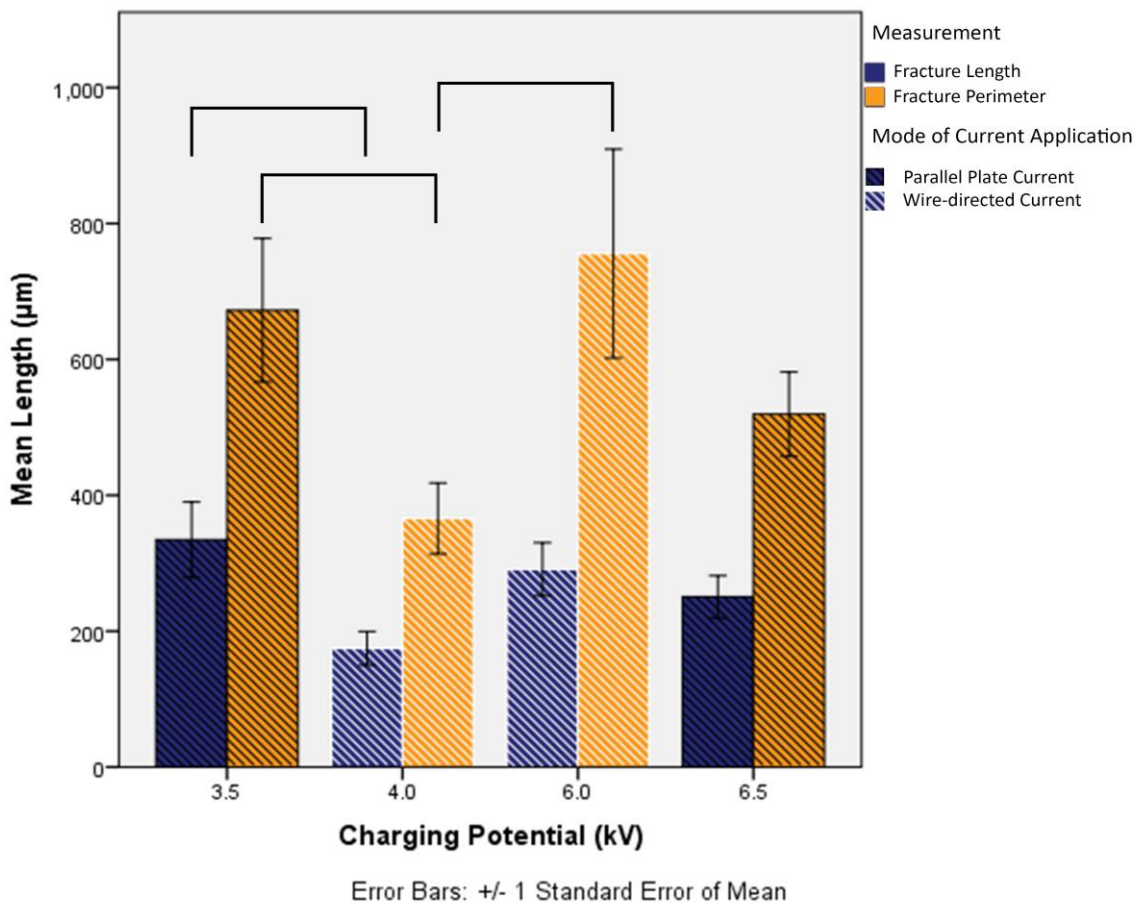


Figure 3.4.1.2: Graphical representation of mean fracture length and perimeter against charging potential

This bar graph demonstrates the significant differences identified for FL between charging potentials of 3.5kV and 4kV (overbar brackets) and for FP between 3.5kV and 4kV (overbar brackets), and between 4kV and 6kV (overbar brackets). CP of 4kV appears to differ the most between the other CP values visually as well as statistically, showing a considerably reduced extent of fracturing.

3.4.2 Evaluation of microscopic damage in relation to current, voltage and mode of current application through variable dimension reduction

The first iteration of principal component analysis (PCA) of the individual fracture data set extracted two principal components (PC). PC1, contributing to 51.224% of the variance, was composed of FA, FL, and FP. PC2 consisted of pV and pC, and contributed 23.125% of the variance (Table 3.4.2.1 and 2) resulting in a cumulative percentage of variance of 74.348% accounted for. PC1 was hence seen as extent of damage observed and PC2 as damaging force.

Table 3.4.2.1: Eigenvalues, respective percentage of variance and cumulative percentages of variance for the first iteration of PCA for the individual fracture data set

This table indicates the eigenvalues of each principal components (PC) as well as their respective variance contribution in the form of percentage, and the cumulative variance represented by multiple PCs. The eigenvalues were used as extraction criteria for the PCs, as only PCs with eigenvalues above 1.000 were extracted, leading to a set of two PCs being extracted. The cumulative variance of the first two and extracted PCs is 74.348%, which represents a substantial amount of the variance observed.

PC	Eigenvalue	Percentage of Variance	Cumulative Percentage of Variance
1	**2.561**	**51.224**	**51.224**
2	**1.156**	**23.125**	**74.348**
3	.838	16.760	91.108
4	.336	6.713	97.821
5	.109	2.179	100.000

Table 3.4.2.2: Principal component extraction with Varimax rotation and Kaiser Normalization of the individual fracture data set

Variables were extracted into two principal components, any Kaiser-Meyer-Olkin (KMO) value higher than .600 defined a strong association between that particular variable and the respective principal component. Values between .300 and .600 defined a moderate association between variables and principal components, while values below .300 a weak association. PC 1 resulted from the combined contribution of the different fracture measurements (FA, FL, and FP), PC 2 the pC and pV.

	Principal Component 1	Principal Component 2
FL	**.946**	-.056
FA	**.936**	-.101
FP	**.876**	.043
pC	-.069	**.765**
pV	.009	**.757**

Regression factor scores obtained from the PCA were plotted to demonstrate relationships (Fig. 3.4.2.1-2). A form of linearization is observable, most likely due to the small number of charging potential cohorts and the relative small sample size overall. Nevertheless, these images demonstrate that although differential experimental treatment was carried out, barring a few outliers, samples demonstrate a similar range of damage. However, small differences are observable pertaining to specific trials. The majority of low end (4kV) WDM resulting fractures, fall within the lowest ranges of observed damage (Fig. 3.4.2.1-2). Which supports

the previous KWA results demonstrating a significantly lower extent of fracturing for the WDM 4kV cohort (Fig. 3.4.1.1 and Fig. 3.4.1.2).

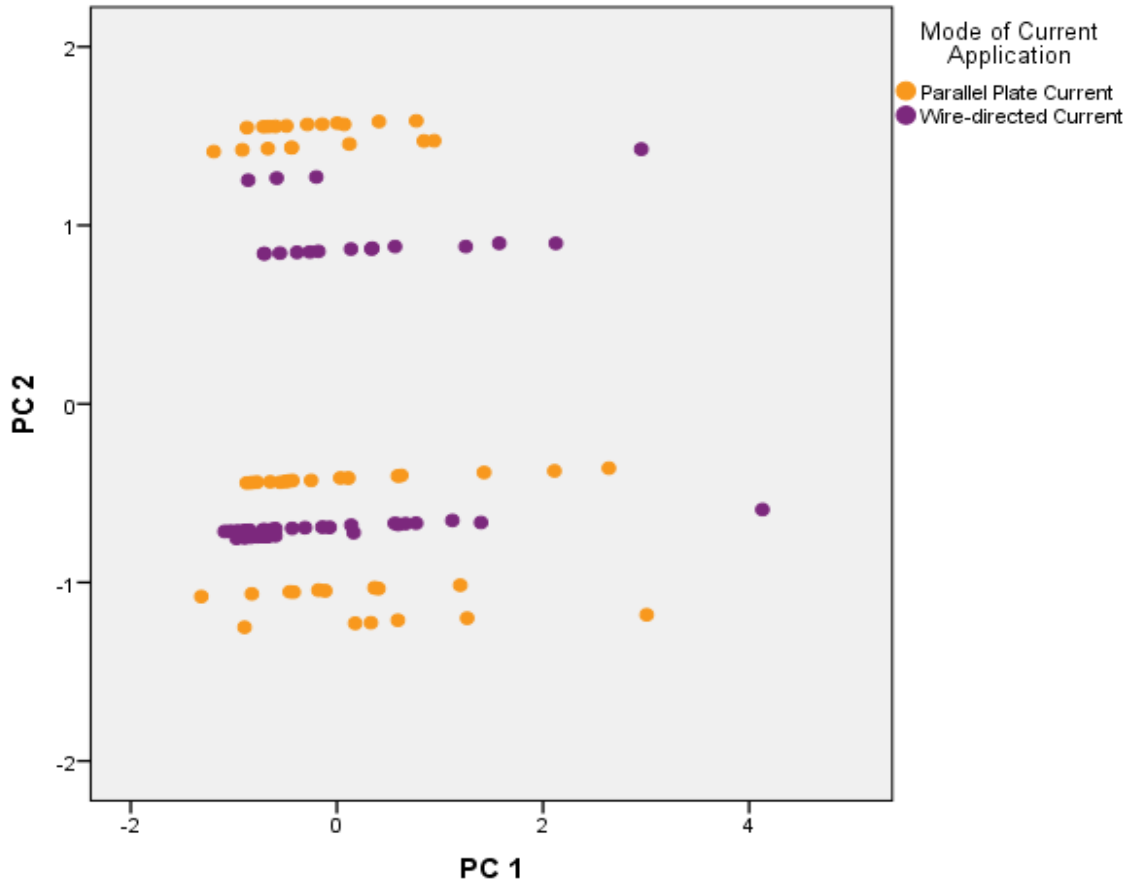


Figure 3.4.2.1: Scatterplot of the regression factor scores for PC1 against PC2 extracted from the individual fracture data set in the first purely continuous iteration and marked for mode of current application

This graphic of PC1 (FA, FL, and FP) against PC2 (pV, pC) demonstrates some linear clustering of observations of damage with relation to the modality of current application, evidenced by the orange data points representing samples which experienced plain parallel plate currents and the purple data points representing samples which experienced wire-directed currents. Noticeable is also the low extent of damage observed in low end WDM trials.

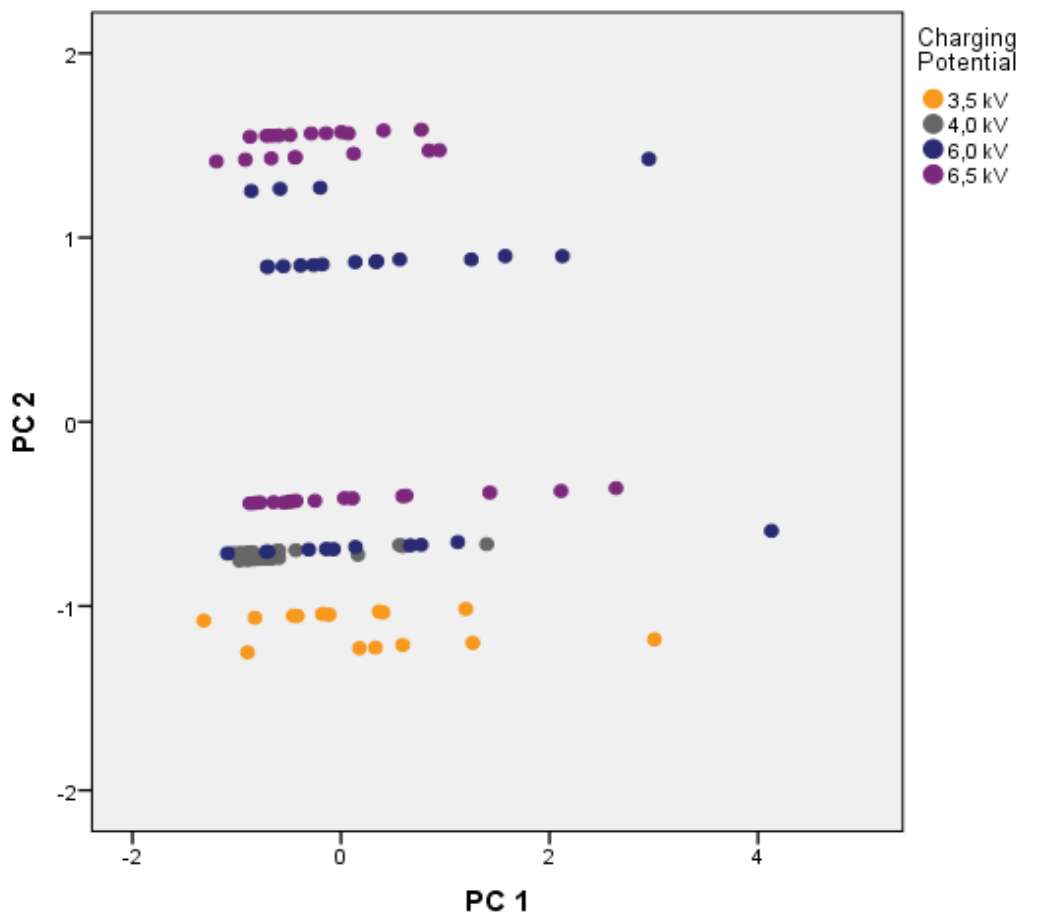


Figure 3.4.2.2: Scatter plot of the regression factor scores for PC1 against PC2 extracted from the individual fracture data set in the first purely continuous iteration and marked for charging potential

This graphic of PC1 (FA, FL, and FP) against PC2 (pV, pC) demonstrates some linear clustering of observations of damage with relation to the modality of current application, evidenced by the orange data points representing samples which experienced plain parallel plate currents and the purple data points representing samples which experienced wire-directed currents. Noticeable is also the lower extent of damage observed in the 4kV trials.

In the second iteration of the individual fracture data, PC1, which explains 32.835% of the total variance, consisted of contributions primarily from the FA, FL, and FP individual micro-fracture measurements (Table 3.4.2.3 and Table 3.4.2.4). PC2, which explains 26.924% of the variance, entailed the combined contribution of the pC, moderately of fracture type (FT) and partly a moderate and negative load of the mode of current application (Mode). PC3, explaining 15.518% of the variance, consisted of the combined contribution of peak voltage pV and a strong positive load of Mode (Table 3.4.2.3 and Table 3.4.2.4). Cumulatively all three

PCs explain 75.278% of the variance of the individual fracture data set, a considerable part of it (Table 3.4.2.3).

Table 3.4.2.3: Eigenvalues, respective percentage of variance and cumulative percentages of variance for the first iteration of PCA for the individual fracture data set

This table indicates the eigenvalues of each principal components (PC) as well as their respective variance contribution in the form of percentage, and the cumulative variance represented by multiple PCs. The eigenvalues were used as extraction criteria for the PCs, as only PCs with eigenvalues above 1.000 were extracted, leading to a set of three PCs being extracted, with a cumulative variance of 75.278%, which represents a substantial amount of the variance observed.

PC	Eigenvalue	Percentage of Variance	Cumulative Percentage of Variance
1	**2.627**	**32.835**	**32.835**
2	**2.154**	**26.924**	**59.760**
3	**1.241**	**15.518**	**75.278**
4	.874	10.922	86.199
5	.582	7.272	93.472
6	.338	4.226	97.697
7	.093	1.157	98.855
8	.092	1.145	100.000

Table 3.4.2.4: Principal component extraction with Varimax rotation and Kaiser Normalization of the individual fracture data set

Variables were extracted into three principal components, any Kaiser-Meyer-Olkin (KMO) value higher than .600 defined a strong contribution of a particular variable towards the respective principal component. Values between .300 and .600 defined a moderate contribution of variables to principal components, while values below .300 a weak contribution. PC 1 resulted from the combined contribution of the different fracture measurements (FA, FL, and FP), PC 2 consisted of peak current (pC) , moderately of fracture type (FT) and partially a negative loading of the mode of current application (Mode), and PC 3 included peak voltage (pV) and a strong positive loading of Mode.

	Principal Component 1	Principal Component 2	Principal Component 3
FL	**.946**	.035	-.134
FA	**.931**	.008	.011
FP	**.868**	.068	.048
FT	.257	.440	-.031
pC	-.092	**.951**	-.069
CP	.003	**.897**	.094
pV	-.086	.276	**.818**
Mode	.046	-.427	**.744**

PC1 was hence again identified as an overall estimation of extent of damage undergone by the bone tissue, while PC2 was identified as an estimation of the damaging force in the form of current delivery, and PC3 as the damaging force in terms of residual voltage and application. Regression factor scores obtained from the PCA were plotted and demonstrated the relationships between damaging force, mode of current application and extent of damage (Fig. 3.4.2.3-4), charging potential (Fig. 3.4.2.5), and fracture type (Fig. 3.4.2.6-7).

When arranged by mode, PCs yield little information in relation to damage observed in each case. The highest currents were achieved clearly with the parallel plate current tests, but seem to cause a comparable extent of damage to lower current observations (Fig. 3.4.2.3). Similarly, higher voltages were obtained with the wire-directed currents and damage varied similarly among different peak voltages (Fig. 3.4.2.4).

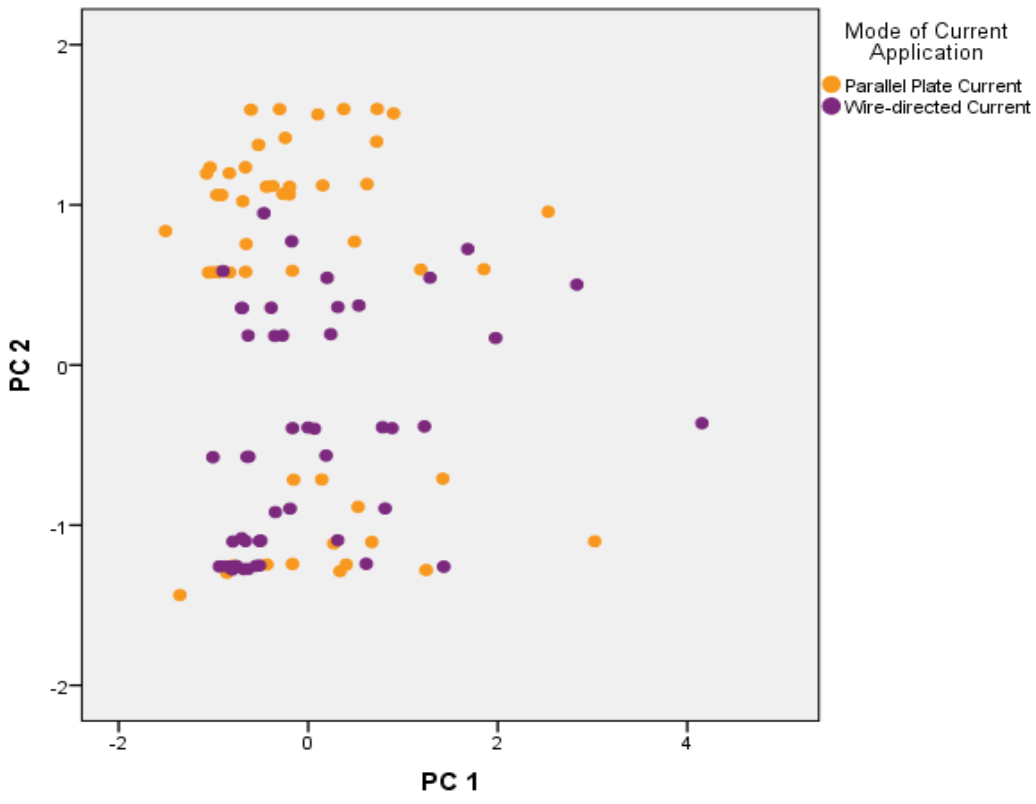


Figure 3.4.2.3: Scatterplot of the regression factor scores for PC1 against PC2 extracted from the individual fracture data set and marked for mode of current application

This graphic of PC1 (FA, FL, and FP) against PC2 (CP and pC) demonstrates some loose clustering of trial observations with relation to the modality of current application, shown by the orange data points representing samples which experienced PPM and the purple data points representing samples which experienced WDM. It is visible how the PPM tests yielded the highest peak currents despite the similar extent of damage observed across both modalities.

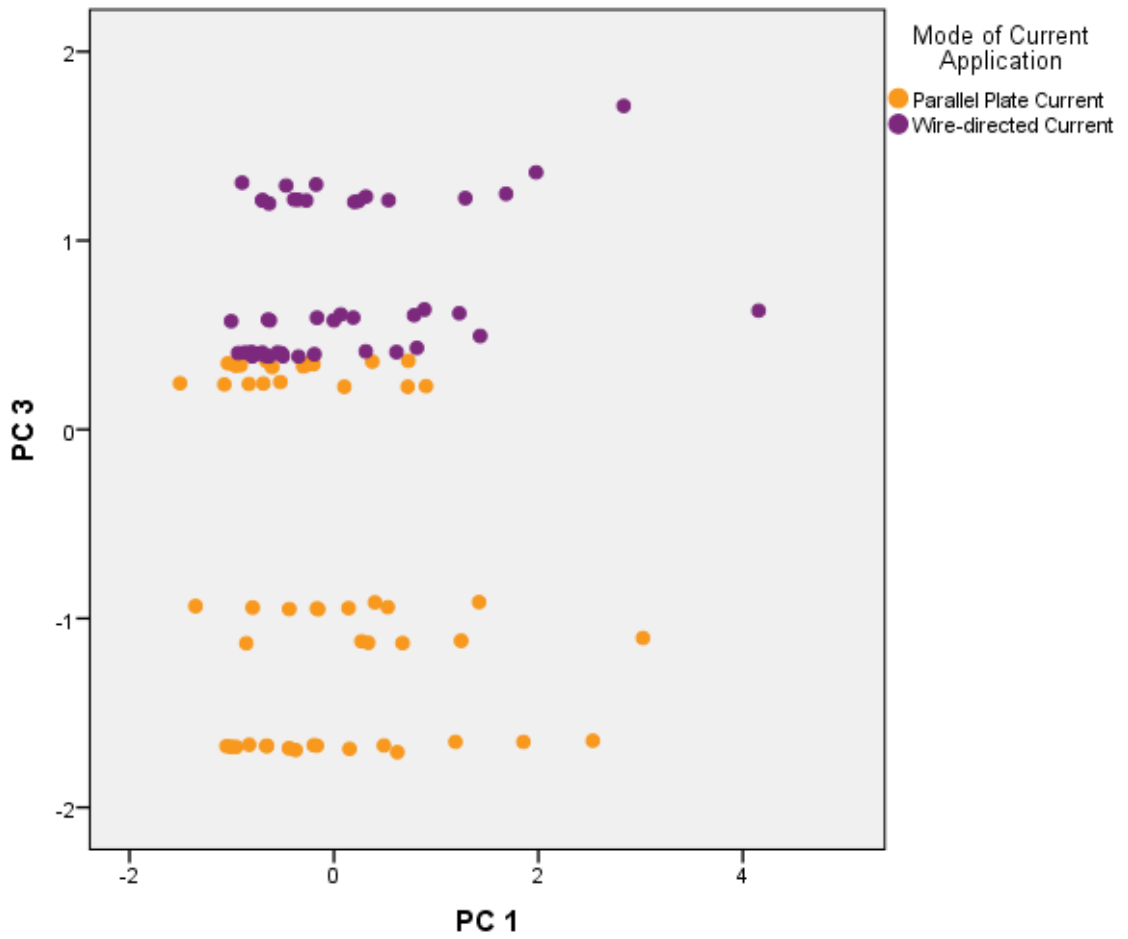


Figure 3.4.2.4: Scatterplot of the regression factor scores for PC1 against PC3 extracted from the individual fracture data set and marked for mode of current application

This graphic of PC1 (FA, FL, and FP) against PC2 (pV and Mode) establishes a separation of observations with relation to the modality of current application. This is evidenced by the orange data points representing samples which experienced plain parallel plate currents and the purple data points representing samples which experienced wire-directed currents. It occurs however, irrespectively of damage and appears more tied to the increased residual voltages and their relation to the modes of current application.

.

The observed clustering in figure 3.4.2.5 is most likely due to the staggered distribution of applied currents and mode of application, as it is influenced by PC2 which is tied to the current and the mode, rather than the fracture extent heavy PC1. The extent of damage seems relatively similar within the different CP trials evidenced by the majority of the points being in the lower half of PC1. Further highlighted is the much lower extent of damage of the 4kV trial group amassed mostly at the lowest end of PC1's scale. A greater amount of extreme damage observations do seem to occur more commonly within the highest two charging potentials

used (Fig. 3.4.2.5). When a comparison of PC1 and PC3 for CP is made, no insights into the nature of the data is achieved.

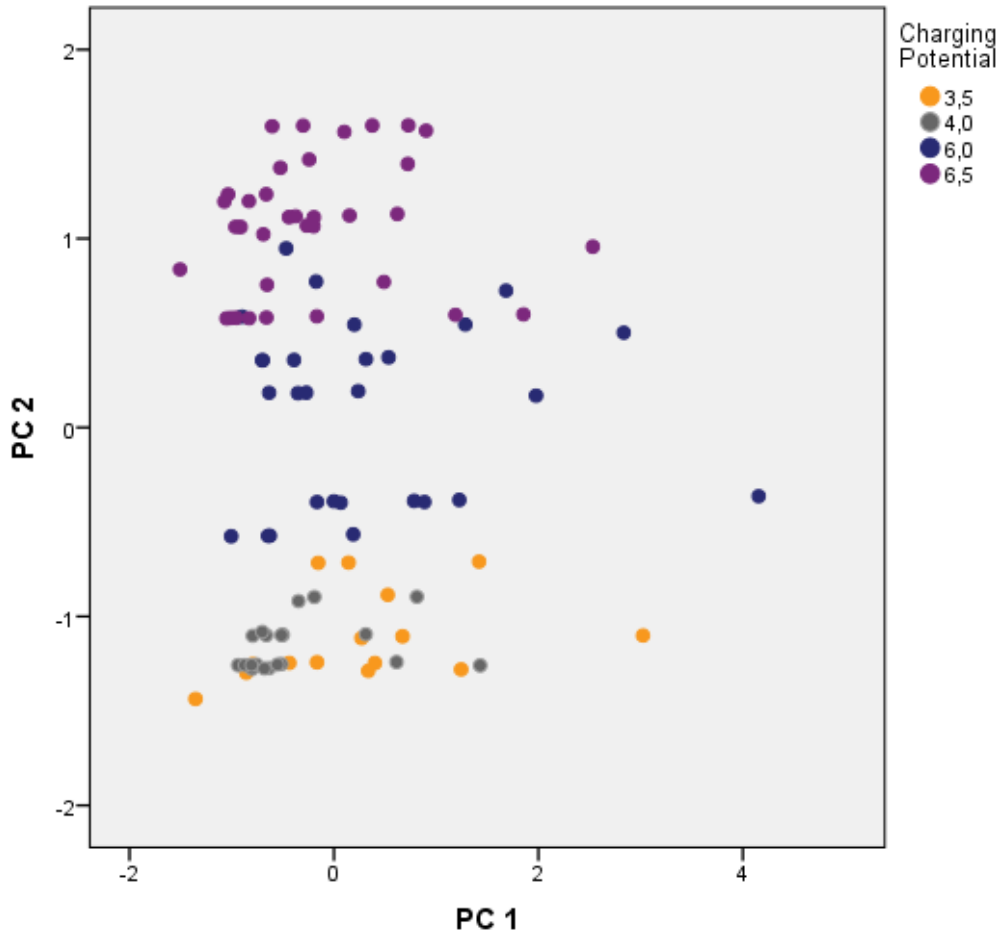


Figure 3.4.2.5: Scatterplot of the regression factor scores for PC1 against PC2 extracted from the individual fracture data set and marked for charging potential

This graphic of PC1 (FA, FL, and FP) against PC2 (CP and pC) demonstrates observations of damage with relation to the charging potentials utilised, a double clustering pattern is observed as a strong relationship exists between charging potentials and peak currents. Similar ranges of damage extent are observed despite varying CP trials. Previously observed decreased damage extent at the 4kV trial group is shown, as well as a greater presence of high damage outlies with the 6 and 6.5kV CP.

Micro-fractures appeared to form no particular clusters in terms of pattern investigation into typological classification. This unclustered appearance; however, suggests a slight shift in fracture typology as the damaging force increases, shifting from more occurrences of radiating and circumferential micro-fractures to less such occurrences and an increasingly irregular and circumferential irregular fracture occurrence as the damaging factors change (Fig. 3.4.2.6).

More irregularity in the fracture typology is particularly observed at higher current intensities (Figs. 3.4.2.6). Radiating micro-fracture appear to be the ones greater in size individually as observed. When compared in terms of PC1 against PC3, typology classification appeared to agree with the overall size difference between typologies. At higher residual peak voltages a greater frequency of radiating micro-fracturing is observed, possibly relating to mechanism of injury (Fig. 3.4.2.7).

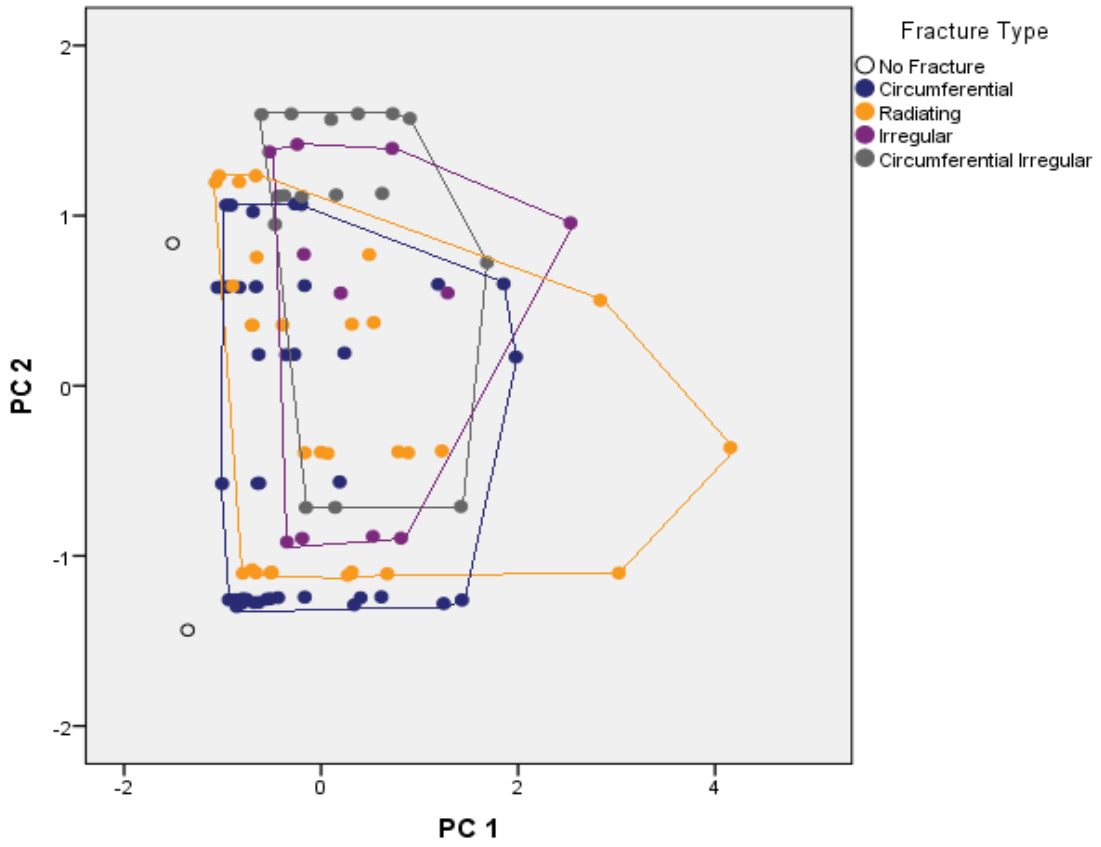


Figure 3.4.2.6: Scatterplot of regression factor scores for PC 1 and PC2 marked for fracture type for the individual fracture data set

This graphic of PC1 (FA, FL, and FP) against PC2 (CP and pC) evidences fracture typology in differing colours. Clustering is not evident for any type of micro-fracture observed, with radiating (orange) and circumferential (blue) fractures tending to greater sizes than irregular (purple) and circumferential irregular (grey). However, an increase in irregular and circumferential irregular micro-fracturing is observed at higher current intensities.

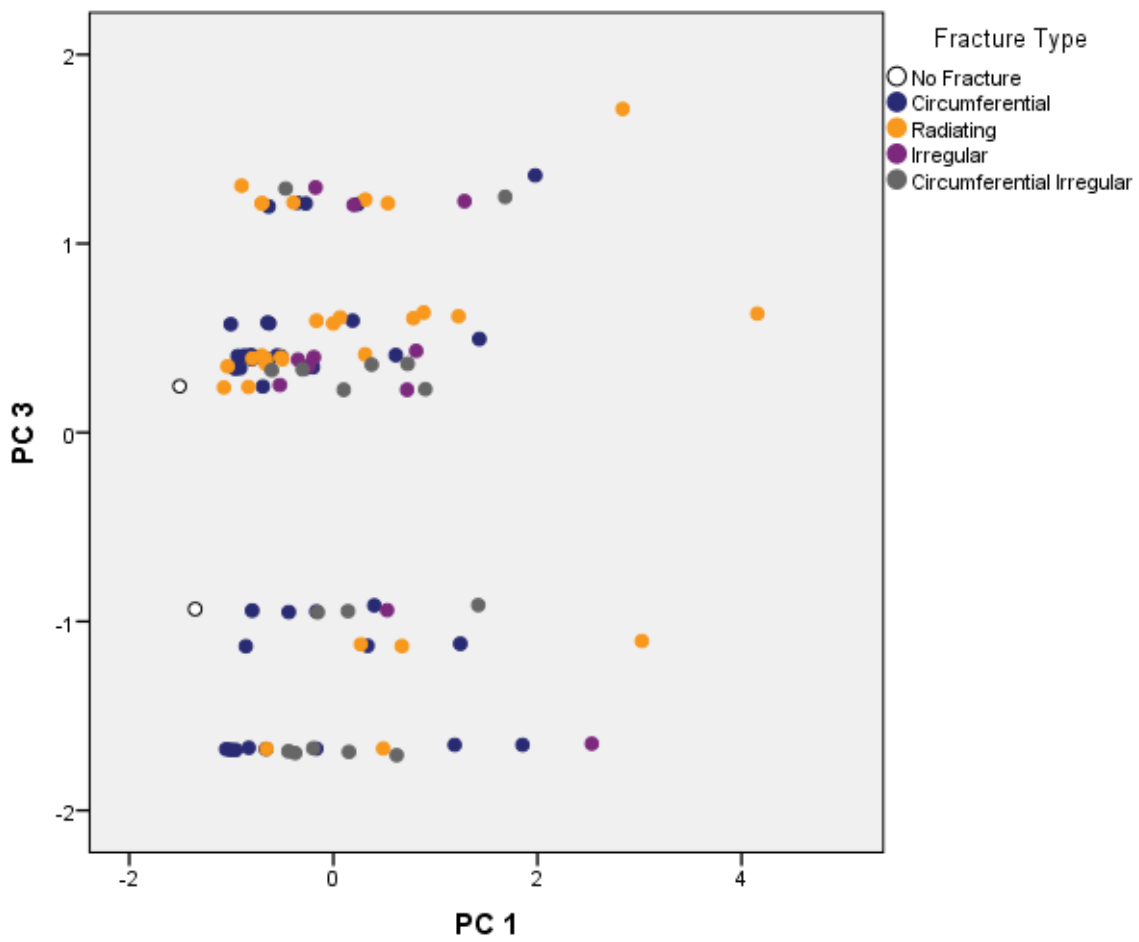


Figure 3.4.2.7: Scatterplot of regression factor scores for PC 1 against PC 3 marked for fracture type for the individual fracture data set

In this graphic of PC1 (FA, FL, and FP) against PC2 (pV and Mode), micro-fracture typology is evidenced in differing colours. No real clustering is observable in this graph, however, consistently with the previous graph, higher extents of damage are observed mainly among radiating micro-fractures. However, a tendency of radiating micro-fractures to occur at higher residual peak voltages is noticeable.

In the first, purely continuous, iteration of the total fracture area data set, which as previously mentioned consists of total fracture area (TFA), the ratios between total fracture area and total bone area (TFA/TBA), and fracture number (FN) from each field of view; two principal components were isolated. PC1, which accounted for 52.363% of the total variance, received contributions primarily from TFA and TFA/TBA. The second component (PC2) isolated, consisted of the peak current (pC) and peak voltage (pV), and accounted for 36.006% for a cumulative 88.369% (Table 3.4.2.5).

Table 3.4.2.5: Eigenvalues, respective percentage of variance and cumulative percentages of Variance for the total fracture data set's first iteration

This table indicates the eigenvalues of each principal components (PC) as well as their respective variance contribution in the form of percentage, and the cumulative variance represented by multiple PCs. The eigenvalues were used as extraction criteria for the PCs, as only PCs with eigenvalues above 1.000 were extracted, leading to a set of three PCs being extracted. The cumulative variance of the first two and extracted PCs is 88.369%, which represents a substantial amount of the variance observed.

PC	Eigenvalue	Percentage of Variance	Cumulative Percentage of Variance
1	**2.095**	**52.363**	**52.363**
2	**1.440**	**36.006**	**88.369**
3	.459	11.476	99.845
4	.006	.155	100.000

Table 3.4.2.6: Principal component extraction with Varimax rotation and Kaiser Normalization of the total fracture data set's first iteration

Variables were extracted into two principal components, any KMO value higher .600 defined a strong association between that particular variable and the respective principal component. Values between .300 and .600 defined a moderate association between variables and principal components, while values below .300 a weak association. PC 1 resulted from the combined contribution of the total fracture area (TFA) and the ratio between total fracture area and total fracture area and total bone area (TFA/TBA). PC 2 includes peak voltage (pV), and the peak current (pC).

	Principal Component 1	Principal Component 2
TFA/TBA	**.996**	.020
TFA	**.988**	.051
pC	-.166	**.877**
pV	.258	**.837**

Hence, as before, PC1 represents extent of damage, in the form of TFA and TFA/TBA, while PC2 represents damaging force in the form of pV and pC. As previously conducted with data from individual micro-fractures, scatterplots of PC1 against PC2 were constructed for the total

fracture data set and demonstrate the relationships between damage observed and charging potential (Fig. 3.4.2.8).

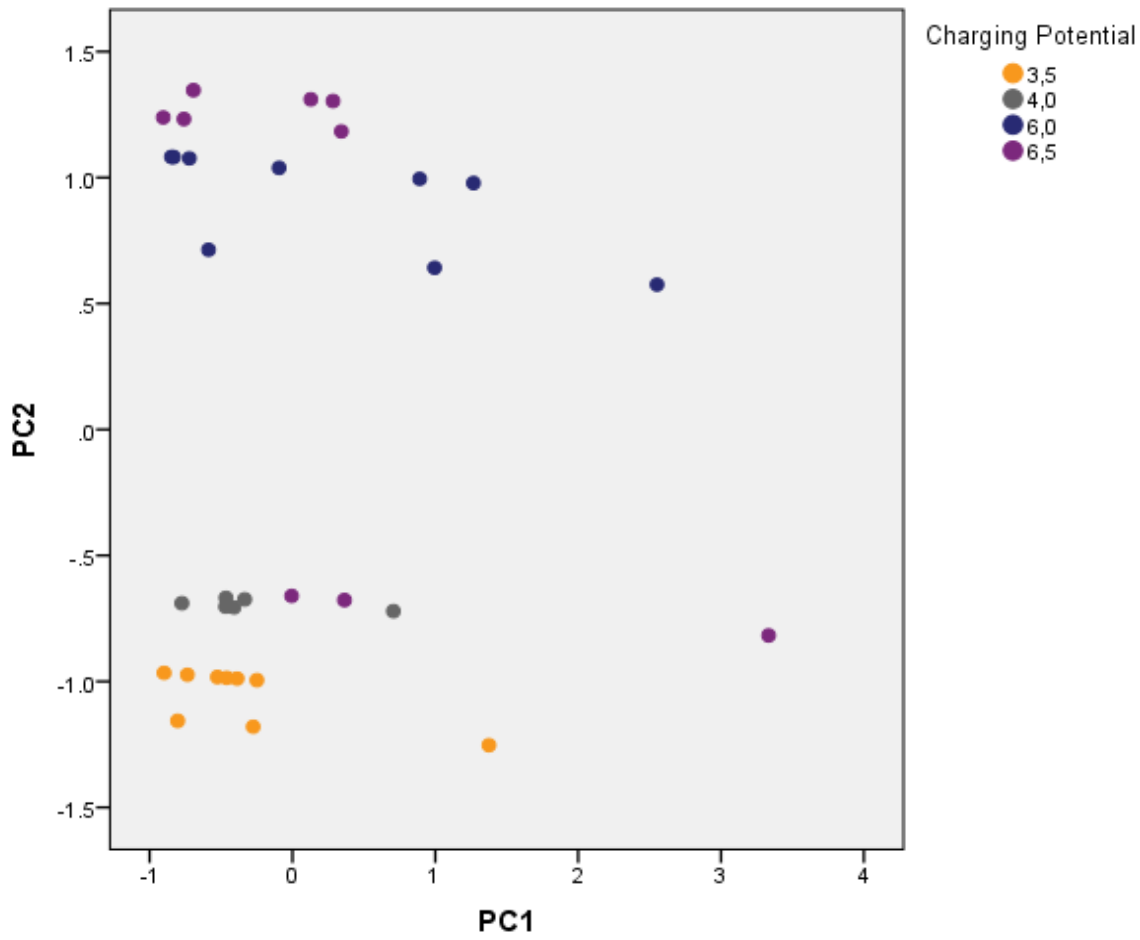


Figure 3.4.2.8: Scatter plot of PC1 against PC2, marked for charging potential, for the total fracture data set's first iteration

This scatter plot of PC1 (TFA/TBA and TFA) against PC2 (pC and pV) demonstrates the low end of observed damage at 3.5kV (orange), the tight clustering of damage observation at the 4kV trials (gray), the increased damage observed more consistently at 6kV (blue), and the spread of resulting voltage and currents outputs of the equipment at 6.5kV (purple).

In Figure 3.4.2.8 the range of damage observed seems to vary according to CP. The greater the CP, the greater the spread of the observed damage. The lower CPs demonstrate the lowest extents of damage observed, occurring at the lowest pV and pC combinations. This is particularly visible at 3.5kV as well as 4kV by the tight clustering and reduced damage extent, contrasted to the greater damage extent and variation at 6 and 6.5kV. The second PCA iteration yielded no new insights into the total fracture data set and was hence included in Appendix F.

To clarify underlying correlations, a Spearman's correlation was carried out, as the data was non-parametric (Table 3.4.2.7). A moderate positive statistically significant correlation was identified between fracture number and peak current (Fig. 3.4.2.9).

Table 3.4.2.7: Spearman's correlation test results on fracture number in the total fracture data set

This table depicts the correlation coefficients and significance level for fracture number (FN) against peak voltage (pV), peak current (pC), and mode of current application (Mode). Outlined in this table is the moderate correlation between FN and pC.

			FN	pV	pC	Mode
Spearman's rho	FN	Correlation Coefficient	1.000	.032	**.394**	.201
		Sig. (2-tailed)	.	.856	**.021**	.254
		N	34	34	34	34

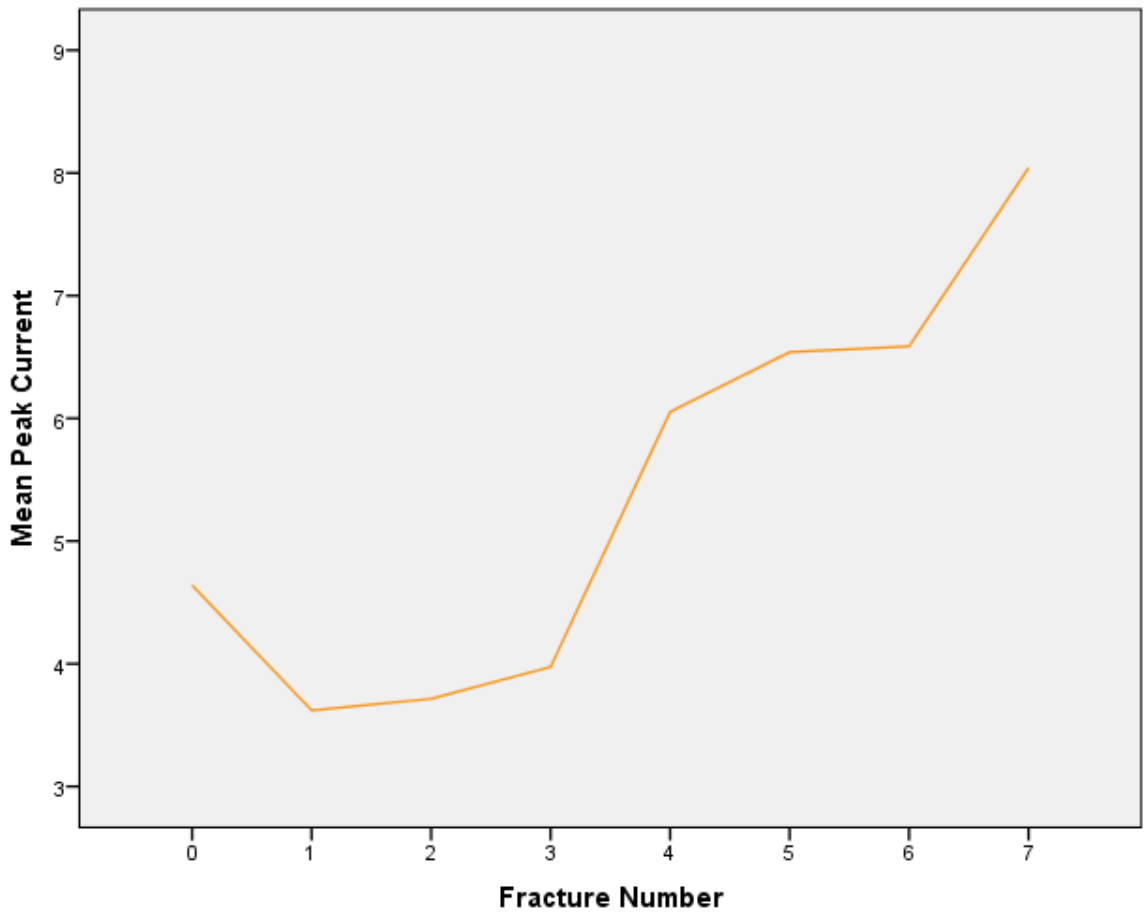


Figure 3.4.2.9: Line graphical representation of fracture number per field of view against mean peak current

This graph outlines a positive correlation between mean peak current and the number of fractures observed in each field of view documented.

Overall, damage appears to slightly increase with increasing current intensity regardless of mode of application. The typology of damage does appear to significantly change in regards to mode of current application; however, it also appears that certain typologies of micro-fracturing may be more likely to have increased sizes than others, mainly radiating micro-fractures demonstrating an increased likelihood to extend further. Conversely, a greater presence of irregularities in micro-fracturing typologies tend to be observed at higher current intensities. Furthermore, the correlation between peak current and fracture number indicates the relationships between damage and current.

3.5 Micro-focus Computed Tomography Observations

Micro-focus computed tomography (μCT) analysis yielded no real results, as the average resolution of the scans obtained from the 2cm diameter blocks, observed in the form of voxel size, was approximately 21μm while the average fracture width was well below that threshold as identified using microphotographs and CellSens software (Fig. 3.5.1).

Based on the resolutions obtained, block three-dimensional reconstructions (Fig. 3.5.2) and orthoslices (Fig. 3.5.3) were unable to demonstrate signs of micro-fracturing or any ultrastructure alteration. A series of five supplemental scans was thus carried out on the histologically processed and mounted thin sections. One was a control section and the remaining four were sections experimented upon at 4kV and 6kV WDM, and 6.5kV and 10kV PPM. These sections presented some of the most extensive micro-structural damage observed throughout all samples.

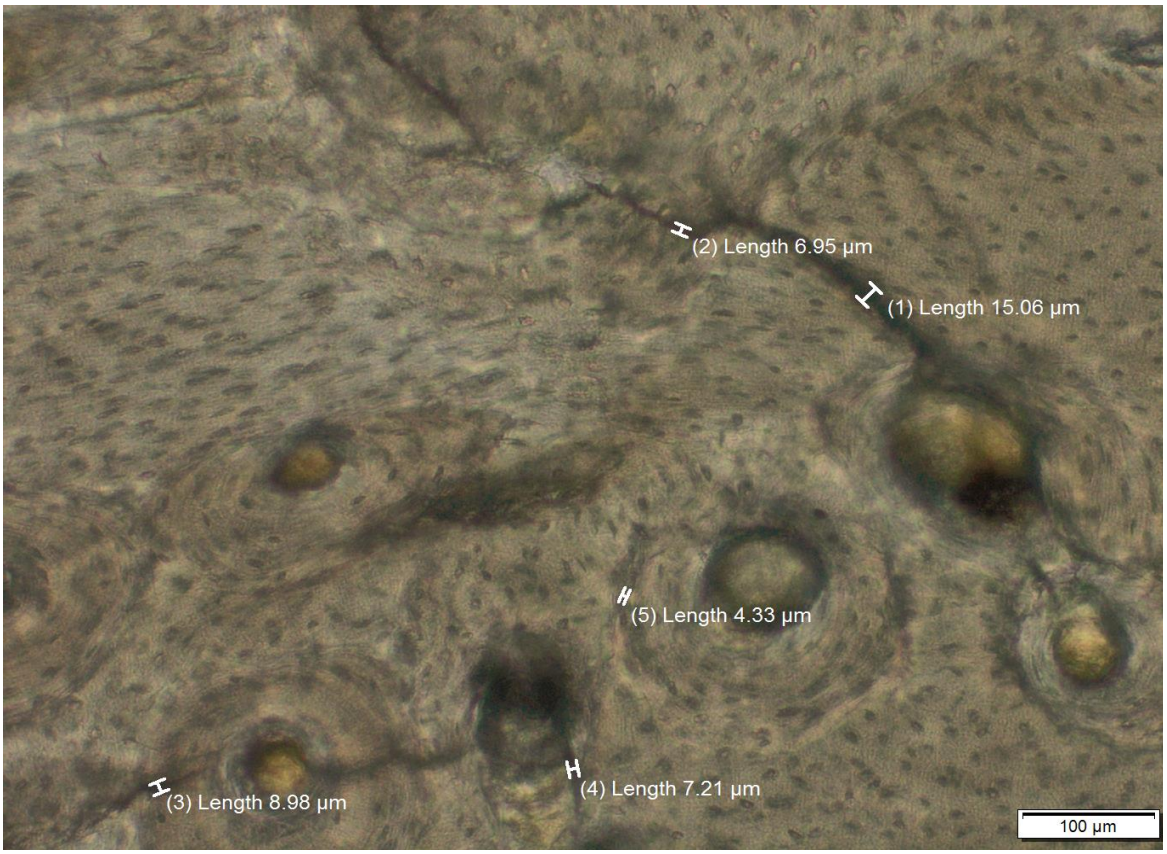


Figure 3.5.1: Photomicrograph of a representative field of view demonstrating average fracture widths (light microscopy)

Multiple fractures observed in this photomicrograph indicate widths (lengths as defined by software) of almost half the average resolution obtained in the process of micro focus computed tomography scanning procedures, ranging from as low as 4.33µm to 15.06µm.

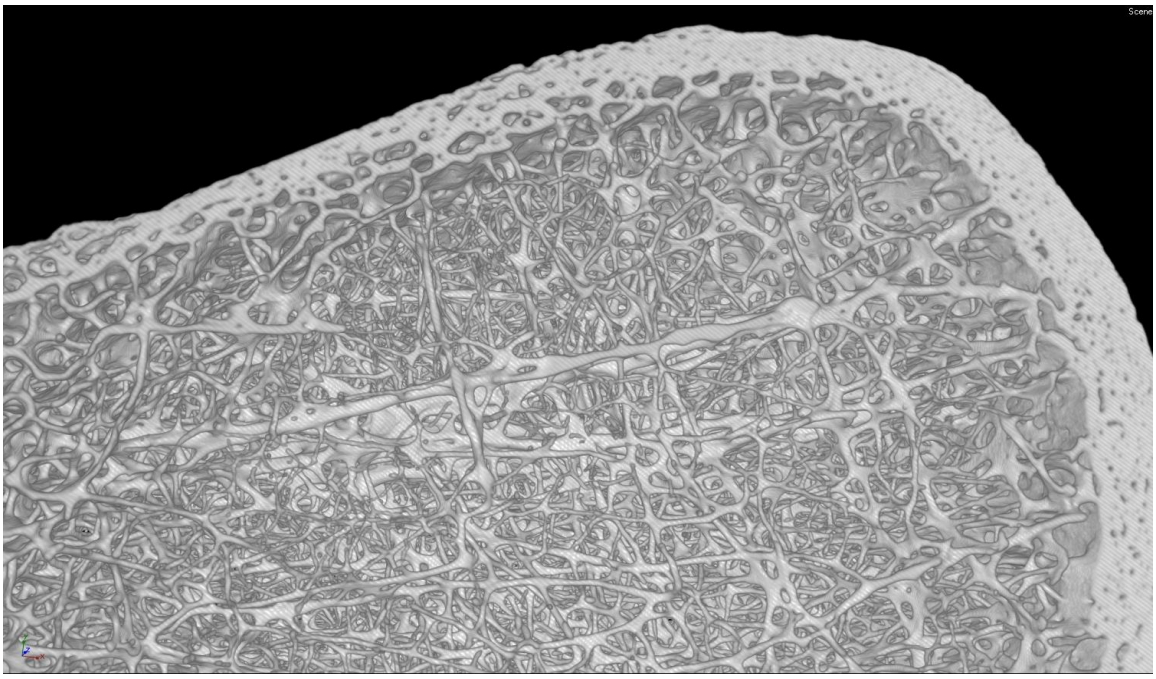


Figure 3.5.2: Close view of three-dimensional reconstruction of experimental bone block after being scanned with μCT

No signs of micro-fracturing are observed in 3D reconstructions, due to the inability of μCT to resolve the micro-fracturing, even in this 6.5kV PPM tested sample.

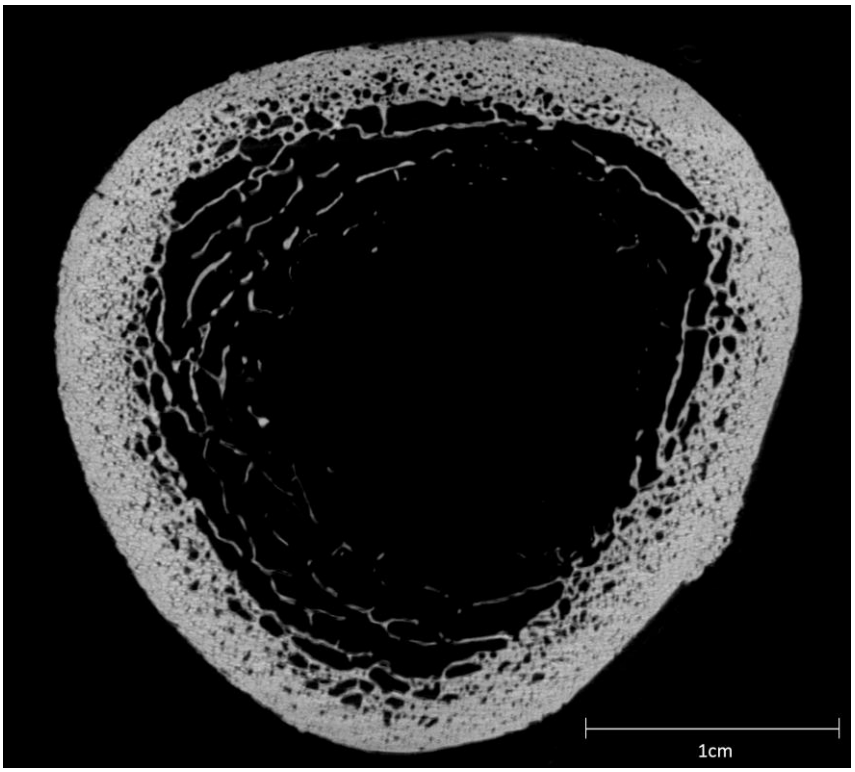


Figure 3.5.3: Orthoslice of experimental sample demonstrating results from post current application μCT

No signs of micro-fracturing are observable within the orthoslices of samples that experienced a 6kV WDM current, due to the insufficient resolution.

In thin section scans, the comparable density of the glass slide was too close to the cortical bone density, resulting in a visual intermingling of the two materials in orthoslices and three-dimensional reconstructions alike (Fig. 3.5.4). This resulted in an increased difficulty to resolve and extract whole view transverse orthoslices (Fig. 3.5.5), which was further compounded by the even higher density of the cover slip, obscuring a clear view of the bone section. An example of the orthoslice recoverable from reconstructions of each scan is presented in figure 3.5.5. Despite the more focused view, micro-fracturing could not be observed, despite these sections presenting with micro-fractures as identified through histological analysis. It is apparent that the heightened resolution obtained in these secondary scans (18.2µm) is still insufficient to resolve micro-fractures.

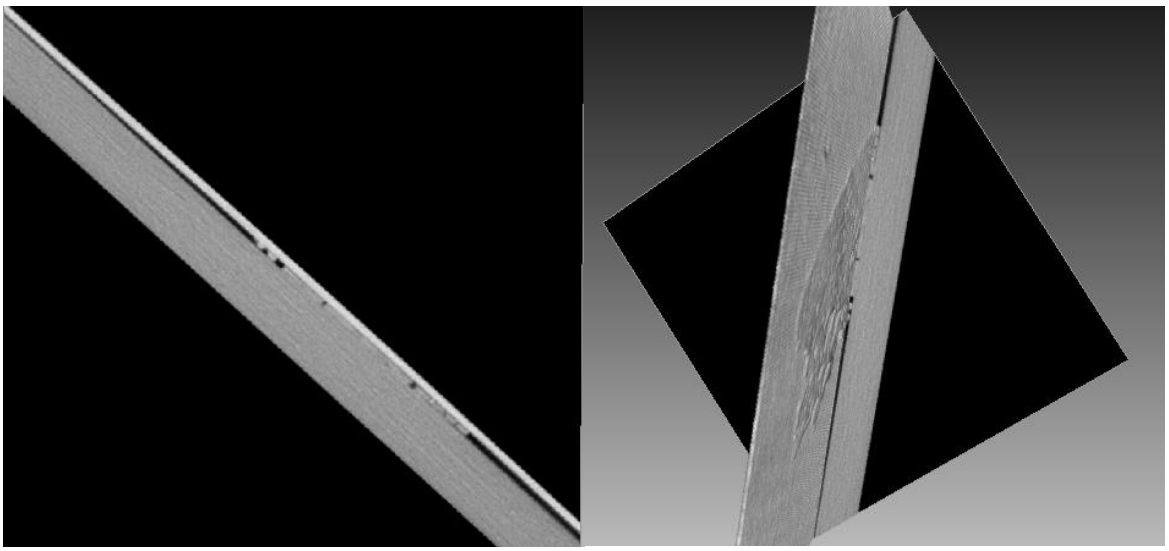


Figure 3.5.4: Visual comparison of material densities of thin section µCT scans

The highly similar densities of glass slide and bone thin section is evidenced in the orthoslice to the left, as the grayscale colour is close to indistinguishable between the 1mm thick glass slide and the porous bone section inserted between it and the denser white coverslip. Attempted 3D reconstruction (right image) resulted in incomplete rendering of the bone section due to the visualisation limitations based on the high indistinguishable density.

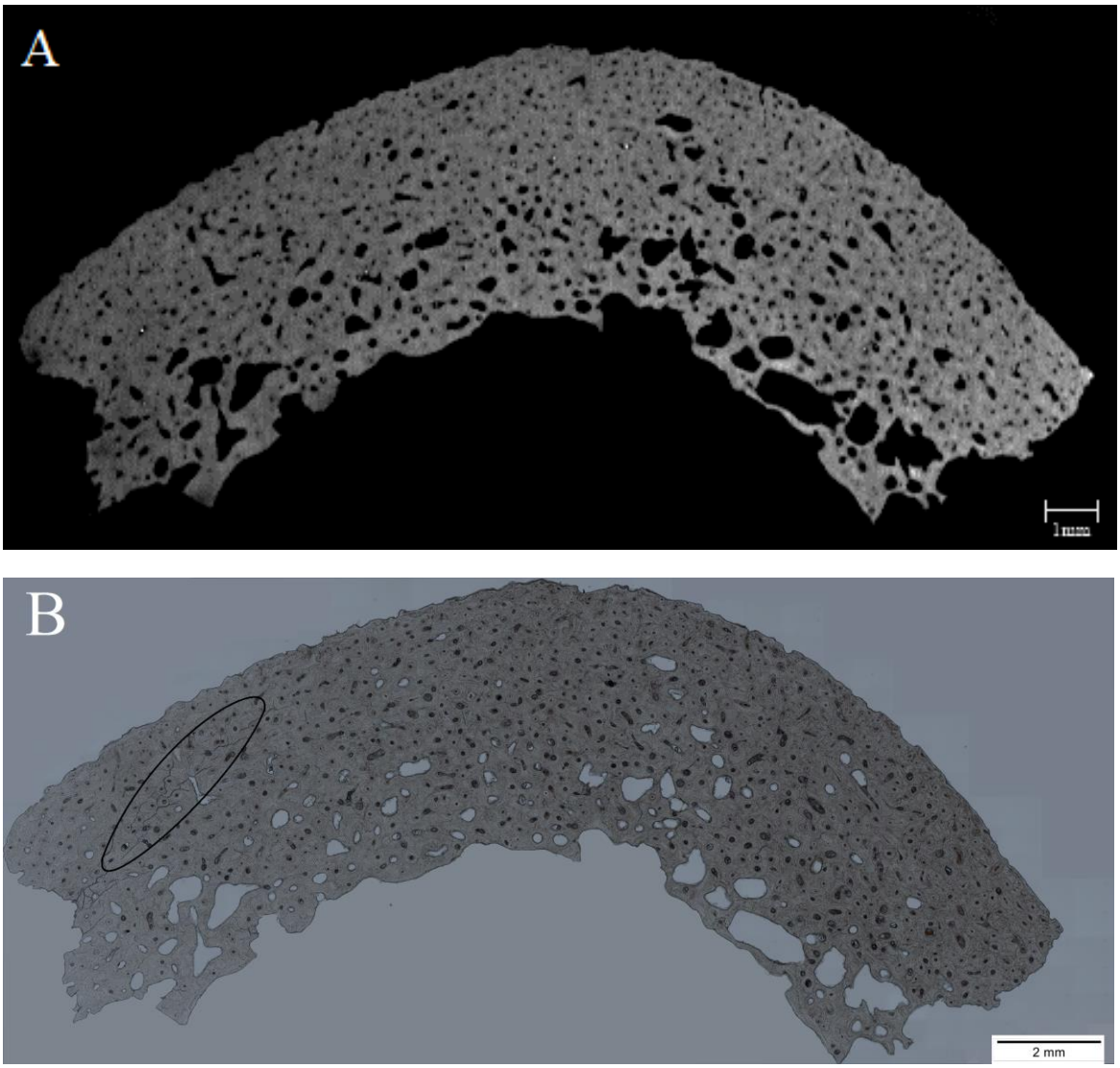


Figure 3.5.5: Example of a transverse orthoslice extracted from a thin section µCT scan (A) contrasted to the equivalent histologically acquired image (B)

Orthoslice extracted through volumetric rendering demonstrates no signs of micro-fracturing, due to insufficient resolution of the µCT scanning technique, compared to a thin section with micro-fracturing observable (black ellipse) in this image.

4 DISCUSSION

Conventionally, lightning fatality identification is reserved to forensic pathology and police services. Typically it can be validated through passer-by witnessing of the incident, meteorological services lightning detection plausibility, incident site investigation, victim clothing investigation or use of soft tissue markers and trauma (Blumenthal, 2005). These trauma markers considered are not always only specific to lightning injury mechanics. The most commonly associated to lightning fatalities being cutaneous thermal disruption at entry and exit sites of the lightning current or underlying metallic objects worn by individuals (Blumenthal, 2005; Pfortmueller *et al.* 2012). The above limitations impede accurate identifcation of cause of death in lightning fatalities, highlighting the need for a simpler, more easily verifiable method.

4.1 Methodology Construct Validity and Fluid Testing

To test the electrical effects of lightning on bone two distinct methods or modes were used in order avoid false discharge and delivery of the current. A standardised parallel brass plate design was used firstly. To eliminate the possibility that the current would travel through air, asymmetrically positioned steel wire brackets were inserted directly below the cortex to direct the current in closer proximity to the bone tissue prior to placement between the parallel plates. The impulse generator experimental design utilised is the closest approximation of the current and energy levels that can be reproduced experimentally. Reported peak currents in lightning strikes range between 2 and 300 kA or 12 and 200 kA (Blumenthal, 2005; Apfelberg, 1974). However, the closest approximation of these current and energy levels that can be reproduced experimentally range from 1 to 100kA (Hauschild and Lemke, 2014). The equipment available for this however had a functional range of 1 to 15kA. Further to which, in order to test the effects of lightning on bone we developed two modes of current application to ensure current delivery and electric field suspension of the bone material. These two modes included, parallel plate mode of current application (PPM) and wide-directed mode of current application (WDM).

PPM consisted of bone blocks being positioned in between two parallel brass plates unmodified and an impulse current released over the testing area. WDM consisted of placing six asymmetrically placed steel wire brackets in a bone blocks, immediately internally to the cortex and within the trabecular space of the bone, and followed by positioning of the bone block in between the parallel plates and directing a current through the specimen testing area.

In order to accomplish the objectives of this study, it became a priority to ascertain construct validity because of the use of embalmed human remains as an experimental sample, since embalmed material was the only form of human remains accessible for this study. This was achieved through the initial fluid tests carried out and described in section 3.1.

Initial low voltage resistivity tests revealed a greater amount of resistance to current flow in fresh and used embalming solutions than in the isotonic saline. This was strongly evidenced by the comparatively delayed presentation of and slow increase in shunt voltage measured. The observed trend persisted throughout all the low voltage tests demonstrating a positive relationship between voltage input and shunt voltage. However, the trend was scaled downward for both embalming solutions, with the fresh solution even more so, indicating the increased resistance of these fluids. Despite these low voltage observations, when the solutions were placed under high voltage current experimentation they behaved identically. Both used and fresh embalming solutions had higher acidity due to their ethanol component. As the solution is used and exposed to air, the ethanol evaporates accounting for the higher pH observed in used embalming fluid. The general understanding of the relationship between pH and conductivity is explained as increasing at high and low pH values, and decreasing as it reaches a pH of 7 since the concentration of H^+ and OH^+ ions is increasingly balanced not permitting quick electron transfer from ion to ion (Hodgeson, 2001; Leveling, 2002). However, in high impulse current and voltage circumstances the high speed momentum of the current can cause dielectric break down of the insulation resistance of the solution which creates an ionised channel through it permitting current passage (Kind, 1978). This was observed in this study. The fluid tests thus demonstrate a strong construct validity of using specimens stored

in embalming fluid for such research. A literature survey revealed no published data on the dielectric property alterations of embalming fluids as a storage means. A handful of studies evaluated the alteration in mechanical and thermal properties of embalmed bone specifically (McElhaney *et al*. 1964; Ohman *et al*. 2008; Sutherland, 2009). They found no real observable difference in tissue properties during short term storage, and noted a greater amount of variation within individual samples than between the controls and embalmed specimens. A single study identified a decrease in dielectric potentials of bone with refrigeration and freezing (Saha and Williams, 1988). However, to the best of our knowledge no further research has been published regarding the effects of embalming solutions on the electrical properties of bone tissue. Having not identified any previous research describing the effects of embalming fluid to bone electrical properties, and with limited to no embalming induced effects on most other properties, the fluid testing results from this study, present a fairly reliable form of construct validity for allowing embalmed remains use for electrical testing. Based on the observed high voltage tests conducted as part of the fluid testing, even with consideration of the low voltage increased resistivity observed, it would be safe to assume that embalming would have no substantial effects on the dielectric properties of bone, at least in the high voltage experimentation spectrum.

4.2 Observed High Voltage Impulse Current Induced Damage

Macroscopic assessment of the majority of the bone blocks subjected to current application, revealed damage identified as minor thermal disruptions of high intensity on small focused areas, causing darkening of the affected area of direct current attachment. The appearance of this damage is, however, inconsistent with traditional thermal bone alteration studied in terms of forensic cremains and burnt bone analysis (Brain, 1993). Normally remains identified in a burnt state tend to have undergone a great amount of thermal disruption, both in terms of time exposure and heat transfer (Fairgrieve, 2008). When thermally modified by means of an open flame, bone undergoes a series of chemical alterations which lead to whole tissue

physical changes. These include the evaporation of physisorbed and chemisorbed water, the interstitial deposition of the degenerated organic component of bone tissue (collagen and ground substance), the inversion of the hydroxyapatite crystals and lastly the fusion of the crystalline inorganic matrix of the bone into a significantly fragile composition (Randolph-Quinney, 2014a). These changes in bone ultrastructure appear more distinguishably through a series of colour changes and heat fractures (Randolph-Quinney, 2014a). These colour changes depend on multiple factors, but are generally consistent with underlying bone physical and chemical modifications, and range from yellow colours as dehydration progresses, to a blackened charred appearance as organic material is destroyed and deposited in the bone matrix, and to an off-white colour as the bone mineral matrix fuses into a calcined weakened state (Schmidt and Symes, 2008). The modifications observed in this study's sample is inconsistent with any of these ultrastructure modifications usually observed in burnt bones.

Ideally, the extent of heat transferred into a sample is measured as heat release rate, which combines both the extent of time and heat released (Shipp, 2004). A similar conceptual approach can be used to describe the damaging process observed in this study. The current is evident as an excessive energy discharge that generates a great amount of heat but releases it over a minute amount of time and over a microscopic surface area (Fig 3.2.2), not allowing for the large scale thermal modifications observed in fire altered remains.

The particularly extensive macroscopic fracturing observed in a few of the samples in this study suggests multiple possible mechanisms, none of which relate directly to heat modification. Notably, there was no prolonged high energy burning, which is generally deemed necessary to cause radical ultrastructural modifications as observed in other studies (Randolph-Quinney, 2014b). A possible reason behind the explosive fracturing may be based on the pressure wave generated around the ionisation channel that is formed for the traversing high intensity current (Blumenthal *et al.*, 2012). This was described briefly in section 4.1 as the mechanism that allows current passage through more resistant fluids. When the pressure

wave surrounding a lightning discharge causes trauma, it is termed barotrauma and is considered the sixth mechanism of injury behind lightning strikes (Blumenthal *et al.*, 2012). This mechanism may be the cause of the large-scale fracturing seen in some samples in this study. As shown in figure 3.2.4B, the current appears to be traversing the sample almost entirely in the medullary cavity, where an expanding pressure wave could possibly cause such an explosive event. This proposition was however not considered as a possible mechanism of injury during the design of the study hence appropriate pressure wave measurements were not taken. However, for future studies this possibility should be taken into account and the pressure wave quantified during the process of current application in order to demonstrate whether a blast wave is powerful enough to be responsible for this extreme traumatic reaction.

The most likely mechanism behind the explosive macroscopic fracturing of the bone specimens is explained by the intrinsic piezoelectric properties of bone (Fukada and Yasuda, 1957). Piezoelectric materials demonstrate the ability to generate an electric field around them when placed under stress; comparatively, inversely piezoelectric materials experience stress forces when placed in an electric field. Bone tissue expresses both forms of piezoelectric properties (Fukada and Yasuda, 1957; Bassett and Becker, 1962; Wieland *et al.* 2015). Previously it has been hypothesised that these properties are due to the orientation and arrangement of collagen fibres and their interaction with the hydroxyapatite crystalline matrix (Martin, *et al.* 1979, Wieland *et al.* 2015). It has also been suggested that the piezoelectric properties of bone may play a role in its lamellar development in a fashion similar to that of ferroelectric crystal domain formation (Martin, *et al.* 1979). The piezoelectric properties of bone have been shown to depend on moisture content and temperature, with high temperatures and high moisture content leading to a stress induced piezoelectric potential being restored to normal levels more rapidly than in lower temperatures and lower moisture contents (Fukada and Ueda, 1979; Reinish and Nowick 1979). High voltage impulse tests generate an instantaneous, transient, powerful electric field in the testing area around the transitioning current (Schon, 2013). This would result in the areas of the bone tissue traversed by the

current to experience a great amount of stress instantaneously and locally. In the three cases where the bone blocks fractured in a large scale, the bone matrix was likely weakened due to the advanced age of the individual, as an increased likelihood of metabolic bone disorder exists at such ages, shown by projections indicate up to 14 million adults in the U.S. over the ages of 50 will have osteoporosis by 2020 (Lane, 2006). This may have resulted in the increased likelihood for the strain experienced under direct electric stimulation to resolve in extreme fracturing. This was in fact observed in the higher ranges of charging potentials (6kV and 10kV) when the current was forced through close proximity to the bone, such as when directed through WDM or the insulation tape covering. The drier nature of the bone as well as the transient increase in temperature seen in the thermally altered samples may also be one of the causes behind the observed fracturing; however, the applicability of these differences to this study may be insignificant as the bone was not given the opportunity to return to a normal state of piezoelectric polarization due to the immediate fracturing.

4.3 Understanding Micro-fracture Occurrence, Extent and Typology

Through comparison of control sections it was observed that normal bone ground sections do not present micro-fracturing as observed in the experimental sections. It is worth noting however, that in the eldest female individual a small prevalence of exclusively short interstitial micro-fractures was evident in certain control samples. We postulate, that this is due to her advanced age and the likelihood of osteopenia, if not osteoporosis, being involved in a reduced mineral content (Lane, 2006). Hence this fracture typology was excluded from consideration as characteristic in high intensity current application, since it may be a function of age and bone density as opposed to related to the electrical treatment applied. Notably, in our earlier animal study, in which a lightning struck giraffe's femur was compared to a series of porcine femora that were tested at 15kV charging potential in a manner similar to this study's, we observed these micro-fractures, exclusively in the experimental samples and not in control samples (Bacci *et al.*, 2014). In that study the porcine bones used were all obtained

from juvenile animals, suggesting that bone mineral density was not the only factor behind the formation of that particular fracture typology as opposed to this study's observations. However, animal bone differs greatly structurally from human bone; particularly, porcine bone used in the aforementioned study, was mainly constituted of lamellar and plexiform bone as well as primary osteons. A comparative study of different age cohorts in terms of electrically induced damage would be necessary to clarify this. Other fracture typologies were not observed in control sections and were considered as characteristic of current induced damage.

Micro-fracturing typologies classified in this study can be contrasted to patterned fracturing observed in a burnt bone. The most evidently analogous in appearance are short interstitial, circumferential and circumferential irregular micro-fractures, all of which were identified as part of previous work carried out by C.K. Brain (1993), in his attempt to ameliorate the understanding of burnt remains identified at Swartkrans. Brain did not classify the fracturing patterns observed as we did in this study; however, similarities in patterns were observed and hence a direct comparison, based on fracture typology identified and defined in this study, was carried out. For the purposes of this study, circumferential micro-fractures were defined as circular micro-fracture extending within the osteon unit's concentric lamellae. Circumferential irregular micro-fractures were defined as curvilinear micro-fractures starting within an osteon unit's concentric lamellae but extending outside the bounds of the cement lines. When applying this classification and observations to Brain's (1993) work, circumferential and circumferential irregular micro-fractures appeared consistently starting at temperatures of 400^{o}C and appearing larger with increasing temperatures (Fig. 4.3.1) (Brain, 1993). Interstitial micro-fracture are also seen at 400^{o}C but seem to disappear at temperatures of 600^{o}C and above (Fig. 4.3.1) (Brain, 1993). The overall extent of fracturing amplifies as exposure temperature increases (Brain, 1993), resulting in an appearance more akin to what this study identified as irregular micro-fractures, which followed no specific patterns in terms of shape, location or size and extended further and wider than other typologies (Fig. 4.3.1). Additionally, in controlled fire experiments Brain (1993) demonstrated, at a starting

temperature of 300 ºC, a consuming blackened charred appearance in the bone samples histological structure (Fig. 4.3.1), caused by the decomposition of the organic components of the bone matrix and soot deposition (Schmidt and Symes, 2008; Randolph-Quinney, 2014b). The remaining type of micro-fracturing observed in the present study, radiating micro-fractures, defined as outward radiating micro-fracture from within the osteon canals, were not mentioned in previous literature and hence, appear unique to high voltage impulse current application trauma, and could be suggested to be induced by multiple mechanisms, including localised microscale barotrauma akin to the sixth mechanism of injury identified by Blumenthal and colleagues (2012) and/or the inversely piezoelectric properties of bone Fukada and Yasuda, 1957; Bassett and Becker, 1962).

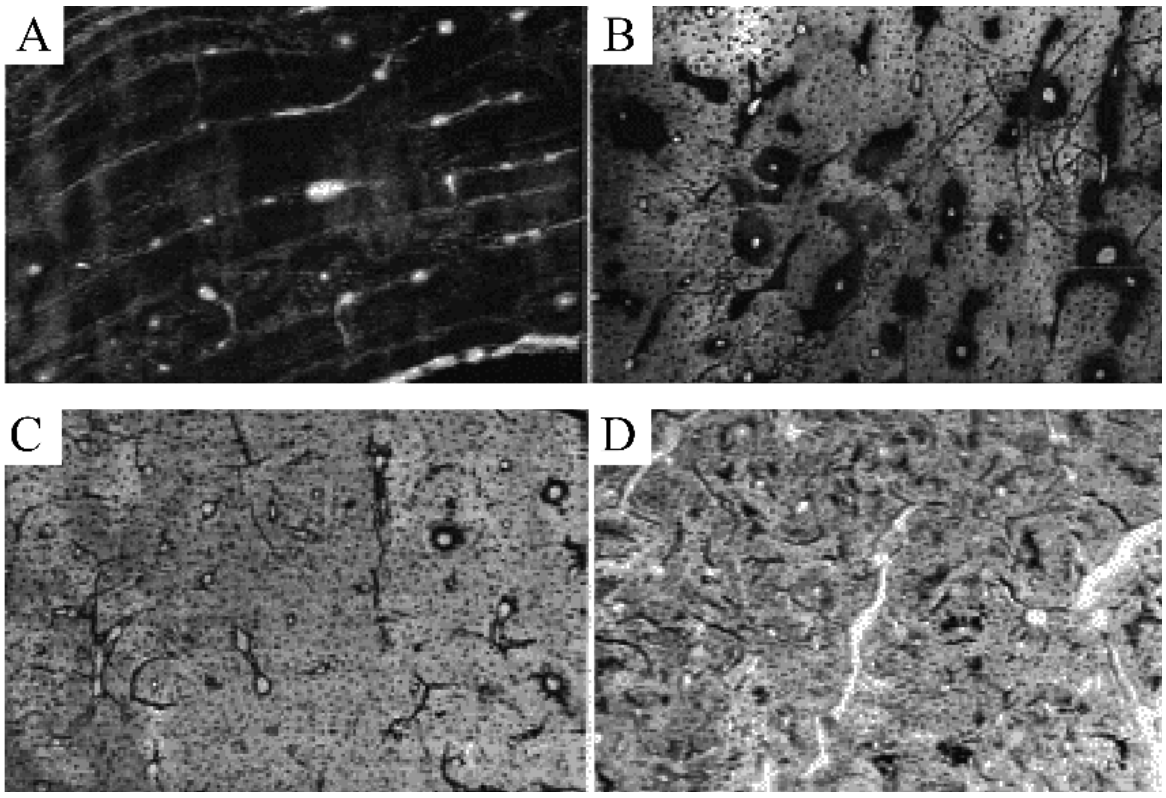


Figure 4.3.1: Thin sections of the experimentally heated bone samples (Brain, 1993)

This image from C. K. Brain's Swartkrans: A Cave's Chronicle of Early Man, highlights the microscopic changes observed in bone burnt at different temperatures. Note soot deposition within the osteon matrix at 300ºC (A), the occurrence of interstitial, circumferential, and circumferential irregular micro-fractures at 400ºC (B) and 500ºC (C), and irregular micro-fracturing at 700 ºC (D).

When compared to damage observed in this study, many similarities are observed. Firstly, as energy levels increase, both circumstances, the extent and typology alters, seeing a marked increase in burnt bone (Brain, 1993) and a relative increase in this study. In terms of typology of micro-fracturing there appears to be a greater presence of irregular and circumferential irregular fractures at greater energy levels in both thermal (Brain, 1993) and electrical studies. However, no soot deposition is observed in the electrically modified samples of this study at a microscopic level.

Bone undergoes dramatic organic and crystalline structural alterations when exposed to great heat intensities. As bone is exposed to heat, collagen fibre denaturation and deposition caused by the micro-fracture and separation of the bone matrix, occurs (Castillo *et al.*, 2013). This deposition results in a cord-like arrangement of the fibres as the temperatures increase to 200 ^{o}C (Castillo *et al.*, 2013). The cords then fracture and start compacting into a seemingly chaotic fashion at 400 ^{o}C (Castillo *et al.*, 2013). This chaotic matrix of denatured collagen and decomposed apatite crystals begin rearranging into cube-like crystalline formation at 500 ^{o}C, which then condense into a solid irregularly shaped crystalline matrix at 600 ^{o}C (Castillo *et al.*, 2013). The inorganic crystals become evident again as larger, round shaped structures at 700 ^{o}C (Castillo *et al.*, 2013). As the temperature increases to 800^{o}C, the crystals become larger and begin fusing with one another (Castillo *et al.*, 2013). As the crystalline structure appears more condensed smaller rounded crystals begin surfacing at 900 ^{o}C, eventually leading to a dense surface of microcrystals (1000 ^{o}C), which demonstrates increasing porosity as the temperature increases further to 1100 and 1200 ^{o}C (Castillo *et al.*, 2013).

The thermochemical changes in bone ultrastructure observed as fractures, crystalline matrix changes and colour changes, lead to greater changes in the physical ultrastructure of the tissue. These include the alteration of osteon size with reports of relative osteon size increase (Bradtmiller and Buikstra, 1984). Contrasting with reports of shrinkage of individual osteon units by up to 16.7% and contemporaneously enlargement of the osteon canal by 10.5% (Nelson, 1992). The nature of these studies highlights great variation, both in terms of

experimental technique and the comparative nature of the samples (Fairgrieve, 2008). Differential burning would result in different changes in ultrastructure and the investigations were carried out on different samples not allowing for a direct comparison (Fairgrieve, 2008).

The table below (Table 4.3.1) indicates in a summarized manner the contrasted differences between the traits induced by electrical damage and those traits traditionally identified as heat modifications.

Table 4.3.1: Comparative summary of electrical and thermal ultrastructure alterations

A summary of the observed bone ultrastructure alterations is presented in tabular form comparing occurrences observed in the high voltage impulse current trials and the ones described in burnt bone literature as characteristic of heat-induced skeletal modifications. The table demonstrates a complete lack of concomitant structural changes traditionally observed alongside micro-fracturing, as well as demonstrates a new form of micro-fracturing observed in electrical modification alone, the radiating type.

Ultrastructure Alteration	Observed in Electrical Experiments	Described in Burnt Bone Literature	Citation for Burnt Bone Literature
Radiating Micro-fracturing	X		N/A
Circumferential Micro-fracturing	X	X	Brain, 1993
Circumferential Irregular Micro-fracturing	X	X	Brain, 1993
Irregular Micro-fracturing	X	X	Brain, 1993
Soot and Organic Material Deposition		X	Randolph-Quinney, 2014b
Colour Changes		X	Fairgrieve, 2008
Osteon Size Alteration	N/A	X	Bradtmiller and Buikstra, 1984; Nelson 1992
Crystalline Matrix Inversion		X	Castillo *et al.*, 2013

Histological analysis demonstrated a lack of concomitant structural alterations traditionally identified in burnt bone circumstances, in any of the samples of this study, barring osteonal size alteration which should be investigated in a future study to eliminate or include in the traumatic pattern observed. Thus thermal dynamisms cannot be designated as the sole mechanism behind high voltage impulse current bone histological structure alterations.

Considering the identified markers of histological alterations, the difference in traumatic mechanism can also be explained by the inversely piezoelectric properties of bone (Fukada and Yasuda, 1957). This hypothesis was put forward previously by us (Bacci *et al.*, 2014), as it consistently explained the wide range of microscopic damage observed in both lightning incidental and experimentally tested samples. The incidental sample consisting of a lightning struck giraffe and the experimentally electrically traumatised porcine specimens. In that study, assessment of a proximal femur from a lightning struck animal had a slightly different pattern of trauma in the histological structure, demonstrating a greater prevalence of radiating micro-fractures than the other types of fracturing observed (Bacci *et al.*, 2014). This was hypothesized to be due to the probable current pathway in a lightning event, believed to traverse a body principally through the neurovasculature of an individual as it is the least resistant tissue component of the organism (Cooper and Cantrill, 1992). This is corroborated by recent research which identified current densities traversing simulated multi-tissue models, and identified that 11% of the total current density experienced by the sample was distributed within the vascular network, with 85% of it being distributed through muscle, 3.5% through fat and only 0.5% through cortical bone and bone marrow (Lee, 2015). Despite the apparently lower current density distribution in the vasculature, the relative component of the vasculature was solely 3% of the model, opposed to the 51% of it consisting of muscle tissue. It thus becomes evident that the fact that 11% of the total current travels in 3% of the total tissue, indicates a higher affinity for the current to travel through the vasculature (Lee, 2015). In this process the current possibly saturates the vasculature with charge and possibly through the nervous system (Cooper and Cantrill, 1992; Meschel, 2009b), and is likely to transfer into the musculature, by passing through gap junctions within cell walls and taking advantage of the depolarising potential of muscle and nervous tissue (Meschel, 2009c).

In terms of reality simulation, blood and vasculature remain one of the most conductive media/tissues in the body as suggested by Lee (2015), as well as Gabriel and colleagues (2009) identifying it as the 4th most conductive medium in the body after urine, cerebrospinal

fluid, and bile. This conductivity is most likely due to the fluid's composition. Blood pH is normally physiologically maintained between 7.36 and 7.42 (Caroline, 2013). The pH would have strong effects on the conductivity of a medium, with the convention being low and high pHs being more conductive while pH values close to 7 would be less conductive (Hodgeson, 2001; Leveling, 2002). In this study however, the opposite was identified. As the literature on blood conductivity demonstrates its high conductivity, there may be underlying complex factors contributing to this increased conductivity. These factors may include the viscosity of the liquid and the cellular density.

Both these mechanism of current passage suggest the piezoelectric effect of the current on bone, as the current travelling through vasculature enters the bone unit and spreads within the cortical bone itself through nutrient foramina and the propagation of the vasculature within the bone matrix. We would hence postulate that as the current travels through the vasculature and within the osteon canals it applies a transient electrical field (Rakov *et al.*, 1996; Schon, 2013) to the bone matrix. This electric field then would induce a level of stress on the surrounding collagen matrix of the bone (Wieland *et al.* 2015) resulting in micro-fracturing, mainly of the radiating type as the osteon units would be the first and most strongly affected components of the skeletal ultrastructure due to proximity. Alternatively the mechanism of injury may possibly occur in a similar manner to a previously discussed concept by Malan (1963). According to this concept, a current would traverse rocky soil material through spaces and fissures which are partly infilled with moist soil which would then react to the heavy current by heating and within the confined space of an intra-mineral cavity, the heated moisture could possibly result in enough pressure being exerted to induce fracturing of the rocks (Malan, 1963).

The other fracture typologies can be explained by a combination of thermal and piezoelectric forces acting on the bones. The remaining current travelling through muscle would form a greater electric field acting on the whole bone and inducing the other typologies of micro-fractures. This is possibly enhanced by the combination of a thermally induced damaging

component to this secondary grouping of micro-fracturing, particularly the more irregular typologies also seen in Brain's (1993) research.

Strain is experienced by bone as inherent patterns of stress build within the bone, and beyond its elasticity, it resolves into destructive damage (Davy and Jepsen, 2001). Five principal types of forces act on bone during trauma, compression, tension, shear, torsion and bending (Davy and Jepsen, 2001). Differentiating which of the five forms of force the bone matrix failed under is problematic with the two-dimensional view of the histological analysis of this study, as no clear direction of fracturing and nature of fracturing is visualised. However, it has been observed that under torsional loading, some microstructural damage termed ''interlamellar debonding'', visually similar to the circumferential fractures observed within this study, occurred (Jepsen *et al.* 2001). In consideration of the location of damage of circumferential micro-fracturing, the collagen fibres of the bone matrix are organised in these same locations, possibly suggesting a strong relationship with the damage observed, since collagen is reported as the main component in the inversely piezoelectric properties of trabecular bone (Wieland *et al.* 2015) Three-dimensional analysis would most likely allow for a great amount of understanding of the force type behind the damage.

In the samples used for this study, as well as the experimental samples in our previous study (Bacci *et al.* 2014), the decreased incidence of radiating micro-fractures is likely explained by the lack of an intact vascular network, possibly resulting in a smaller component of the current actually travelling in the above mentioned manner, and rather affecting the bone as a whole piezoelectrically and thermally. Furthermore, partial decomposition of the collagen, heavily responsible for the piezoelectric properties of bone (Wieland *et al.* 2015) is likely a factor as well. The samples of our previous study (Bacci *et al.* 2014) and the samples of this present study may provide a basis for consideration of peri- and post-mortem trauma involvement of a high voltage impulse current on an individual.

4.4 Quantification of Electrical Effects on the Bone Histological Structure

Repeatability of the study was found reliable in terms of intra-observer error with low margins of error. However, fracture quantification was identified as lacking in terms of multi-observer reproducibility. An extremely high margin of error was identified; however, it was observed that the discrepancy in measurements and micro-fracture identification was tied to the observers' inexperience. This was evidenced by the fact that many structures, commonly highlighted and measured as fractures by the secondary observers, were simply normal bone histological structures. The structures most commonly confused with fractures included transverse canals being confused with irregular fractures and osteon cement lines being confused with circumferential fractures. In other cases fractures were confused with normal histological appearance, resulting in an overall pronounced variation in individual fracture and total fracture measurements as well as number of fractures. Despite this variation in histology knowledge based fracture identification and measuring, the methodology of analysis was consistent and accurate as the simple total bone area measurements obtained were strongly consistent throughout all observers. It is thus highlighted that a great amount of training in bone histology and fracture identification is necessary to allow the quantification of structural modification in high voltage impulse current tests.

Initial statistical tests were centred on identifying significant differences in associations between any of the damage inducing factors (charging potential, peak voltage, peak current and mode of current application) and the resulting damage extent and typology (fracture number, fracture dimensions, total fracture area to total bone area ratio and fracture type). Significant differences identified within the individual fracture data set when grouped under charging potential. The differences observed in fracture area and fracture perimeter between a charging potential of 4kV and 6kV, both of which consisted of wire-directed mode testing (WDM).

Other significant differences identified included the fracture length and fracture perimeter over charging potentials of 3.5kV (PPM) and 4kV (WDM). Perimeter appearing as a significant difference in both groups where area and length appeared significantly different is probably also a result of its close relationship to both those measurements. The substantial increase in fracture area between the 4kV WDM current and the 6kV WDM current, suggests possibly a greater threshold for damage with wire-directed current application. Possibly meaning that damage scales at greater increments when the current is forced through the tissue, as opposed to purely directed at it, as in the PPM. In this circumstance, 4kV could potentially be a lower end threshold for thermal damage, similar to Brain's (1993) findings, suggesting a greater extent of thermal damage variation may exist amongst trial groups within WDM than in PPM. This is corroborated by the macroscopic singeing and thermal alterations observed and discussed earlier, and augments the explanation of the combined electrical and thermal damage hypothesis.

Principal component analysis yielded interesting results. The first purely continuous variable iteration of principal components always yielded two principal components, while the second iteration of both data sets yielded three principal components, almost inducing a separation of peak voltage and peak current as different damage inducing forces. In the first iteration of the individual fracture data set, analysis of individual fractures resulted in a PC1 that described the extent of observed damage and a PC2 composed of pC and peak residual voltage. The first iteration is able to corroborate the low extent of damage observed at the 4kV WDM charging potential but also demonstrates a lower extent of damage at 3.5kV PPM than the other two trials at 6kV WDM and 6.5kV PPM. This suggests that higher charging potential may induce greater extent of damage, even if by small increments, regardless of mode of current application. As 6kV WDM demonstrated slightly less damage than 6.5kV PPM but still within similar ranges throughout all testing charging potentials (Fig. 3.4.2.1-2).

The second iteration, inclusive of categorical data, demonstrates firstly and foremost the nature of the experimental design in greater currents being generated with PPM. However, a similar extent of damage was observed throughout charging potentials (Fig 3.4.2.3-5).

When fracture typology is observed, there is clear increased likelihood of radiating micro-fractures extending further than other types of fracturing as most observed outliers were of this typology (Fig. 3.4.2.6-7). Furthermore it is noticeable that a shift in greater presence and prevalence of irregular and circumferential irregular micro-fractures is more likely at higher peak current observations, a prediction accommodated by the sixth mechanism of injury (Blumenthal *et al.* 2012). Conversely, PPM, which yielded the higher intensity currents, also appeared to induce increased irregularity in fracture typology and marginally decreased extent of damage, compared to WDM with a greater extent of radiating micro-fracture observation. This suggests an increased likelihood for the vascular current delivery and proximity piezoelectric interaction being the driving mechanism behind micro-traumatology observed. Further observations in consideration of peak voltage and mode, demonstrate similar trends as described above. Higher peak voltages were tied to a higher extent of fracturing and more consistent with radiating micro-fractures as well as increased intermingling of fracture typologies across lower residual voltages. This corroborates the piezoelectric stress hypothesis, as a greater potential difference induces a greater electric field in the area the potential difference is experienced.

In total fracture analysis the primary PC consisted of fracture measurement components and fracture number while the second component consisted of pV, and pC. A highly suggestive likelihood of increased total fracture measurements was observed across the highest charging potentials (6 and 6.5kV), despite the large extent of variation in measured peak voltage and peak current output throughout these tests.

These speculations suggested an underlying correlation, which was identified in the form of a moderate correlation between fracture number and peak current, suggesting a certain extent of dependence of degree of fracturing to current intensity.

4.5 The Inability of µCT in Resolving Micro-fracturing

Micro-focus computed tomography (µCT) has been commonly used as a non-invasive investigation method in geology and bone research (Bouxsein *et al.*, 2010; Golab *et al.*, 2013). It has noteworthy potential in revealing three-dimensional internal features and ultrastructure modification of solid materials in a non-invasive manner. It has been used in multiple studies to visualize and quantify fracture networks observed in minerals (Cai *et al.,* 2014; Viljoen *et al., 2015)*. However, it has hardware limitations, tied to the energy levels of the beam emission that limit the X-ray beam penetration, and beam cone spread size, which limits the resolution of the resulting scans (Buzug, 2008).

Theoretically the finest resolution available in conventional µCT is the width of the X-ray beam. However, for that resolution to be achieved the sample scanned would need to be close enough for the radiation to strike it and be entirely included in the spread to be scanned in its entirety. This explains how smaller samples (i.e. bone thin sections) are more likely to obtain a finer resolution. Regardless, the nature of the equipment does not allow for a finer resolution for the thickness and size of the samples of this study, not even thin sections. Furthermore, the µCT facility at NECSA is not a phase contrast coherent scanning system (Hoffman and De Beer, 2012), which limits the observed resolution due to its low capacity to differentiate similar internal densities as different contrast levels to identify structural damage (Buzug, 2008).

This resulted in the inability of the scans to demonstrate any sign of micro-fracturing and indicated that techniques which can resolve finer structures would be necessary to identify this form of damage in a non-invasive manner. Such techniques exist and include nano-focus computed tomography (Stellenbosch University, Western Province, South Africa) and phase

contrast synchrotron tomography (European Synchrotron Radiation Facility ESRF Grenoble, France). The nano-focus tomography in Stellenbosch is a commercial enterprise, resulting in a prohibitively expensive option, while synchrotron tomography is located on a different continent making analysis increasingly complex logistically. These techniques are hence too limiting and would not be available for use in forensic lightning death identification circumstances, by police or forensic services.

5 CONCLUSION

5.1 Introduction

The occurrence of lightning strike fatalities is fairly common throughout the world and amongst the highest ones are observed within South Africa, with up to 100 annual fatalities (Blumenthal *et al.* 2012). Customarily lightning fatalities are identified based on a multitude of soft tissue and circumstantial evidence as demonstrated by a plethora of case studies and clinical reports from forensic pathologist services (Wright and Davis, 1980; Mitchell and Davis, 1984; Mellen *et al.,* 1992; Lifschultz and Donoghue, 1993; Blumenthal, 2005). Circumstantial evidence commonly attributed to lightning fatalities are witnessing of the lightning event, identificiation of heat damaged debris and clothing on or at the lightning event site, and lightning metereological reports (Lifschultz and Donoghue 1993; Blumental, 2005). Conventionally, cutaneous burns of varied ranges are considered indicative of lightning trauma and death (Blumenthal, 2005), however, low incidence of electrical burns complicates manner of death identification (O'Keefe Gatewood and Zane 2004).

Large scale skeletal trauma has been identified and considered as a possible indicator of lightning fatalities in a handful of cases (Kotak *et al.* 2000; Kannan *et al.* 2004), however microstructural bone alteration has not been considered previously to the best of our knowledge. Our previous study outlined a series of traumatic patterns identifiable within lightning struck and experimentally current tested samples (Bacci *et al.* 2014). The traumatic patterns common to both samples consisted of extensive micro-fracturing typologically partially diverse to previously identified traumatic micro-fracturing related to heating and burning of bone tissues (Brain, 1993).

5.2 Findings

Fluid tests were initially carried out to justify usage of embalmed material for the study. An increased resistance to current flow was identified in embalming fluids at low voltage tests. However, when tested under high voltage high amperage currents all solutions behaved

virtually identical, demonstrating distinct breakthrough and current delivery across the sample. This suggested no substantial difference in current propagation properties of the solutions, permitting use of embalmed remains.

In the process of current application to bone, thermal and electrical forces are introduced into the tissue and induce alterations in the bone structure in the form of fracturing either macroscopic or microscopic. Macroscopic damage was evidenced in situations where currents were forcibly directed within the bone structure and were observed as gross and thorough explosive fracturing of the bone samples. This observation is firstly reported within this study to the best of our knowledge and suggests a possible identifier for lightning fatalities even at a macroscopic level, however there are certain limitations mainly related to sample size and incidence of this type of injury in this study's presentation. The effective damage on the microstructure of bone is related to the impulse current applied and generates identical typologies of damage as observed in our previous work (Bacci *et al.* 2014). The typologies of damage consist of 4 diverse scopes of fracturing, including radiating, circumferential, irregular and circumferential irregular micro-fracturing. The latter three typologies of fracturing have been identified within previous literature demonstrating micro-structural damage experienced by bone through burning (Brain, 1993); however, extensive radiating micro-fractures have not been previously identified in any studies looking at micro-structural bone injury known to us. When compared to heat induced damage and ultrastructural alterations, the observed electrically induced injury were vastly different. The alterations of electrically induced micro-trauma identified did not include most of the traditionally observed features characteristic of thermal modification such as soot deposition and colour alteration (Brain, 1993; Schmidt and Symes, 2008; Randolph-Quinney, 2014a-b), except at a macroscopic level in direct areas of observable current contact, or crystalline matrix inversion and fusion (Castillo *et al.*, 2013).

Considering the overlay of traumatic patterns, the presence of a newly defined form of damage, as well as the lack of other conventional fire related bone ultrastructural alterations we suggests an intertwined mechanism of injury. We hence suggest that the effects on the

bone tissue may be caused by the electrical effect of the high voltage current and induced electric field affecting the inversely piezoelectric bone (Fukada and Yasuda, 1957; Wieland *et al.* 2015) combined with the thermal effects resulting from direct contact of the current with the bone. However, this would require a more directed approach in terms of experimental method to comprehend the true mechanism behind the micro-trauma observed.

Despite KWA demonstrating significant differences between current trials, there were differences both between and within different modalities. However, intensity of charging potential did seem to induce greater extents of damage, even if only slightly in the overall relative similarity in damage extent, throughout all graphic depictions of the measurement data both in KWA analysis and PCA. Furthermore, typology of damage was observed to shift to a more irregular nature at greater peak currents. This form of irregularity in fracturing was akin to the micro-fractures identified in Brain's (1993) research, suggesting the possibility of these fractures being induced thermally at potential transient temperatures of 400-600^{o}. Additionally, radiating micro-fractures, the type identified solely in this study and believed to be particularly indicative of electrical effects on bone, appeared to generally be greater in size than most other micro-fracture types, irrespective of mode of current application. These micro-fractures could also potentially be a result of microscale barotrauma within osteon canals as corroborated by the sixth mechanism theory which would predict greater extent of fracturing with greater current intensities (Blumenthal *et al.* 2012).

The electrical experimental design in its dual nature of parallel plate current application versus wire-directed current application, yielded different but interesting results nonetheless. It is hence suggested that between the two current application modes, the parallel plate mode would simulate lightning better as this is an unmodified direction of current into the tissue. However, for this study the wire-directed current was a necessity to ascertain the passage of the current through the bone and not allow for air conduction, possibly limiting the effects on the tissue. This will be considered for future studies in order to design a better total area of

contact with the tissue and render the wire-directed mode a testing ground procedure rather than a final one.

A great complexity in the mechanism of micro-traumatic effects induced by impulse current application is evident. A possible threshold of damage is possibly observable within wire-directed currents due to the suggested greater thermal impact of a closely associated current pathway than in the residual electric field over the testing area. Further differences in current pathway and direct effects on its attachments sites need to be investigated for the creation of qualitatively accurate methodology for the identification of cause of death in lightning fatalities.

Unfortunately, despite its great potential as both a non-invasive and highly analytical method of micro-fracture visualisation, micro-focus computed tomography was unable to resolve fracturing extents even once samples were reduced to minimal physical sizes and re-scanned for an increased resolution (Buzug, 2008). We can thus confidently state that μCT is unable to assist in this type of investigative process at the current levels of fracturing observed.

5.3 Limitations and Future Studies

As observations were made throughout the course of this study multiple limitations were identified. In the experimental process the first limitation consisted of the plate design being larger than the bone specimens, allowing for areas of the parallel plates having no bone in between them. This may have resulted in air conduction of the current. This was then considered and the second modality of current application was carried out as wire-directed. The effects of the two modes of current application, are based on a small number of cohorts. This should be clarified by following up this study with an extensive wide range multi-trialled series of experiments to fully define differences of current pathway and effect on bone. Furthermore, the two modes of current application are intended to simulate two different manners of electrical conduction, and may or may not be a direct representation of lightning current pathways though the body or skeleton. It would be necessary to correlate patterns of real life scenarios possibly by inspecting entry and exit sites of the current for localised

underlying skeletal tissue damage. This would allow to address the possible equifinality of lightning fatalities, based on distinct pattern identification, possibly related to the sheer intensity of energy behind lightning strikes which may be beyond other energy levels of skeletal trauma.

Further interesting considerations come from the sampling used in this study. The sample for this study consisted of older individual's bones. Since this has been the first experimental study identifying electrically induced damage on human bone, it remains to be seen whether age of the individual is significant for extent of damage. Hence, a study focusing on the effects of age of an individual to the experienced thermal and electrical modification should be carried out. Further research examining the possible differences in fracture pattern and extent between the bone elements and the location investigated may be of interest to allow elimination of variation and as a result increase the accuracy of any forensic methods generated.

Skeletal tissue may also react differently to current exposure based on mineral density and the overall size of the bones preservation of the tissue, particularly in relation to decomposition of the organic material of the bone. The multitude of these conditions should be considered as limitations for this study and should be further investigated in differential experimentation of bone material in relation to electrical properties and effects to high voltage current application. Only once a better understanding of the different responses based on condition and constitution overarching statements or definitions can be considered along electrical induced trauma to the skeleton.

Although embalming fluid exposure and preservation was tested within this study for construct validity, a more extensive study on the effects of bone dielectric property alteration with focus on differential preservation techniques including different embalming fluid solutions against fresh bone as well as a comparison to dry bone would outline or resolve concerns behind the use of embalmed remains for studies in electrical interactions with bone. This, combined with

comparison between dry and wet bone would also allow to understand the manner in which preservation state of remains may influence observed effects of lightning strike, possibly allowing for identification of peri-mortem versus post-mortem electrical trauma.

Considerations on the large scale macro-fracturing, in terms of its use as an indicator of lightning fatalities, will need further testing as it was observed in only 3 of the experimental specimens within a small sample size and may not be representative. Factors inducing this particularly violent reaction of the bone may also include bone mineral density and preservation techniques, possibly increasing likelihood of this reaction with increased fragility of bone. Further research should be aimed at eliminating concerns of equifinality around extensively fragmentary traumatic features.

Perhaps the most important future study however, would consist of thorough experimentation to extensively comprehend the full extent of bone tissue modification induced by electrical and thermal energy. Ideally this would be achieved by shifting the measurements of interest to energy input (Vuille *et al.* 2009a-b) into the bone as opposed to temperatures (Shipp, 2004) and current intensities in order to allow for a more direct comparison of the two mechanisms within the energy continuum of trauma. Alternatively, it would be beneficial to carry out high voltage impulse current tests while considering the temperatures experienced by the bone material due to the current and recording more precisely the exact pathway of the current and its thermal component via a thermal high speed camera. This could be further expanded upon both lightning and high voltage electrocution by including the consideration of time, particularly in response to the heat levels generated. This could be possible as the impulse generator used to simulate a lightning strike impulse experimentally, generates currents comparable to low end lightning strikes but also consistent with high voltage electrocution conditions if extended in time of exposure. Furthermore, investigation of osteon size alteration in specimens experiencing a high voltage impulse current should be carried out to explore their possible occurrence in electrical modification of bone. Possibly allowing the understanding of the extent of the thermal effect of current on bone.

It would be of great interest to attempt at the least nano-focus computed tomography and possibly even synchrotron scanning in order to attempt and three-dimensionally identify and compare micro-fracturing matrices within the same samples before and after current treatment, even if the high cost of such equipment would make it impossible to use for forensic cause of death identification. As this process would likely yield crucial information into the biomechanics of bone piezoelectric damage, it would be a logical extension of the study to measure stress-strain loadings piezoelectrically induced during current application via standard techniques of mechanical engineering material testing. Such techniques would involve placing strain gauges to measure the strain explicitly and compare it to strain bone undergoes in a mechanically induced set of trials[1] (Fritton and Rubin, 2001). This would allow to understand the nature of bone structural failure as well as how forces dissipate throughout the bone.

In successful future applications of this study's findings, more information would be required to understand if different histological treatment in the processing of sections might induce different, yet unidentified artefacts not accounted for in this study. Ideally a simplified categorisation would be more favourable to the application of this study to a forensic setting. However, at a present stage our understanding is too narrow to allow for this type of classification, this could only be done once more extensive studies are carried out and definitions are outlined based on a bigger sample and more varied ranges of tissue states as well as current intensities.

Since lightning is generally composed of multiple lightning strokes forcing current through a system (Rakov and Uman, 2003a), it would be important to consider the effects of multiple current applications within one bone element which would more likely simulate a more realistic scenario with multiple current strokes from a lightning discharge.

[1] For this to be possible specific stain gauges able to withstand high temperatures and a high current in close proximity will be necessary, as well as strain gauges that have a rapid enough signal response to capture the transient impulse current.

Lastly, the effects of lightning strike resulting in fatalities should be directly investigated in the form of a comparison of experimental data both from this study and future studies that completely define the current damage observed within bone tissue. A direct comparison of these results to bone samples retrieved from individual cases of lightning fatalities should be hence carried out. This would allow to overcome the risk of equifinality in lightning fatality identification within the medico-legal process by providing distinct criteria in terms of mechanism of trauma and manner of death, resulting in an isotaphonomic ideal method of lightning fatality definition.

REFERENCES

Aaron, J.E. and Shore, P.A., (2004). Histomorphometry. In: Langton, C.M. and Njeh, C.F. ed. *The Physical Measurement of Bone*. Bristol, Philadelphia: Institute of Physics Publishing, pp.185-224.

Anderson, R.B., (2001). Does A Fifth Mechanism Exist to Explain Lightning Injuries? *IEEE Engineering in Medicine and Biology*, 20, 105-116.

Andrews, P., and Williams, D.B., (1973). Use of Principal Components Analysis in Physical Anthropology. *American Journal of Physical Anthropology,* 39, 291-303.

Apfelberg, D.B., Masters, F.W., and Robinson, D.W., (1974). Pathophysiology and Treatment of Lightning Injury. *The Journal of Trauma*, 14, 453-60.

Bacci, N., Augustine, T., Randolph-Quinney, P., *et al.* (2014). Recognition of lightning-induced damage to the skeleton: a forensic taphonomic study. *IEEE Xplore Digital Library,* 1299-1302.

Bassett, C.A.L., Becker, R.O., (1962). Generation of electric potentials in bone in response to mechanical stress. *Science*, 137, 1063–64.

Berger, K., Anderson, R.B., and Kroninger, H. (1975). Parameters of lightning flashes. *Electra,* 80, 223–37.

Bernstein, T., (1973). Effects of electricity and lightning on man and animals. *Journal of forensic sciences*, 18, 3–11.

Bertalanffy, L., (1950). The theory of open ssysten in physics and biology. *Science*. 111, pp. 23-9

Blumenthal, R, (2005). Lightning Fatalities on the South African Highveld a Retrospective Descriptive Study for the Period 1997 to 2000. *American Journal of Forensic Medicine and Pathology.* 26, 66–69.

Blumenthal, R., (2009). A retrospective descriptive study of electrocution deaths in Gauteng, South Africa: 2001–2004. *Burns.* 35, 888-94.

Blumenthal, R., Jandrell, I.R., and West, N.J., (2012). Does a Sixth Mechanism Exist to Explain Lightning Injuries? Investigating a Possible New Injury Mechanism to Determine the Cause of Injuries Related to Close Lightning Flashes. *American Journal of Forensic Medicine and Pathology.* 33, pp. 222-6.

Blumenthal, R., Trengrove, E., Jandrell, IR., Saayman, G. (2012). Lightning medicine in South Africa, *South African Medical Journal*, July, 102, 7, pp. 625-6.

Bouxsein, M. L., Boyd, S. K., Christiansen, B. A., *et al.* (2010). Guidelines for assessment of bone microstructure in rodents using micro–computed tomography. *Journal of bone and mineral research*, 25, 1468-86.

Brain, C.K., (1993). The occurrence of burnt bones at Swartkrans and their implications for the control of fire by early hominids. In: Brain, C.K. ed. Swartkrans: A cave's chronicle of early man, Transvaal Museum, pp.229-42.

Bradtmiller, B., and Buikstra, J.E. (1984). Effects of burning on human bone microstructure: a preliminary study. *Journal of Forensic Science*, 29, 535-40.

British Standards Institute, (1992). Protection of structures against lightning. BS 6651.

Brooks, C.E.P. (1925). The distribution of thunderstorms over the globe. *Geophysical Memoires,* (Air Ministry, Meteorological Office, London), 24, 147–64.

Buzug, T.M., (2008). Fundamentals of X-ray Physics. In: Buzug, T.M. ed. Computed Tomography: from Photon Statistics to Modern Cone Beam CT. Berlin: Springer-Verlag Berlin Heidelberg. pp. 15-59

Cady, W. G. (1946). Piezoelectricity: An introduction to the theory and application of electromechanical phenomena in crystals. New York: McGraw-Hill Book Company, p. 183.

Cai, Y., Liu, D., Mathews, J.P., *et al.* (2014). Permeability evolution in fractured coal—Combining triaxial confinement with X-ray computed tomography, acoustic emission and ultrasonic techniques. *International Journal of Coal Geology*, *122*, pp. 91-104.

Carlson, W.D. *et al*., (2003). Applications of high-resolution X-ray computed tomography in petrology, meteoritics and palaeontology. *Geological Society, London, Special Publications*, 215, pp. 7–22.

Caroline, N., (2013). Nancy Caroline's Emergency care in the streets (7th ed.). Buffer systems: Jones & Bartlett Learning. pp. 347–9

Castillo, R.F., Ubelaker, D.H., Acosta, J.A.L., *et al.* (2013). Effects of temperature on bone tissue. Histological study of the changes in the bone matrix. *Forensic science international*, 226, 33-37.

Chan, Y., and Walmsley, R.P., (1997). Learning and Understanding the Kruskal-Wallis One-Way Analysis-of Variance-by-Ranks Test for Differences among Three or More Independent Groups. *Physical Therapy,* 77, 1755-61.

Cooper, M.A., (2002). A Fifth Mechanism of Lightning Injury, *Academic Emergency Medicine,* 9, 172-4

Cooper, M.A., and Cantrill, S.V. (1992). Electrical and lightning injuries. *Patient Care*. 26, 158-75.

Cooper, M.A, Holle, R.L., and Andrews, C., (2008). Distribution of Lightning Injury Mechanisms. In: *20th International Lightning Detection Conference, Tucson, Arizona, USA.*

Cooper, M.A, and Holle, R.L., (2010). Mechanisms of Lightning Injury Should Affect Lightning Safety Messages. In: *21st International Lightning Detection Conference, Orlando, Florida, USA.*

Currey, J.D., (2013). *Bones: Structure and Mechanics*: Princeton University Press, USA.

Davy, D.T., and Jepsen, K.J., (2001). Bone Damage Mechanics. In: Cowin, S.C., ed. Bone Biomechanics Handbook. Boca Raton, London, New York, Washington D.C.: CRC Press. pp. 18-1 - 18-23.

Dryden, I.L., Bai, L., Brignell C.J., *et al.* (2009). Factored principal components analysis with applications to face recognition. *Statistics and Computing*, 19, 229-38.

Fairgrieve, S.I., (2008). Forensic Cremation Recovery and Analysis. Boca Raton: CRC Press. pp. 42-58.

Fritton, Rubin, (2001). Bone Deformation Using Strain Gauges. In: Cowin, S.C., ed. Bone Biomechanics Handbook. Boca Raton: CRC Press. pp. 8-1 - 8-35.

Fukada, E. and Ueda, H., (1979). Temperature dependance of the piezoelectric constant of hydrated bone and collagen. In: Brighton, C.T., Black, C.T., and Pollack, S.R., eds. Electrical Properties of Bone and Cartilage: Experimental Effects and Clinical Applications, pp.31-45.

Fukada, E., and Yasuda, I., (1957). On the Piezoelectric Effect of Bone. *Journal of the Physical Society of Japan*, 12, 1158–62.

Fuquay, D.M., Baughman, R.G., Taylor, A.R., *et al*. (1967). Characteristics of seven lightning discharges that caused forest fires. *Journal of Geophysics Research,* 72, pp. 6371–3.

Fuquay, D.M., Taylor, A.R., Hawe, R.G., *et al.* (1972). Lightning discharges that have caused forest fires. *Journal of Geophysics Research,* 77, pp. 2156–8.

Gabriel, C., Peyman, A., & Grant, E. H. (2009). Electrical conductivity of tissue at frequencies below 1 MHz. *Physics in medicine and biology*, *54*, p. 4863.

Gijben M., (2012). The lightning climatology of South Africa. *South African Journal of Science*, 108, pp. 1-10.

Gill, T., (2008a). Initial steps in the development of a comprehensive lightning climatology of South Africa. MSc dissertation, Johannesburg, University of the Witwatersrand.

Gill, T., (2008b). A lightning climatology of South Africa for the first two years of operation of the South African Weather Service lightning detection network: 2006-2007. In: *20th International Lightning Detection Conference*, *Tucson, Arizona, USA.*

Golab, A., Ward, C. R., Permana, A., *et al.* (2013). High-resolution three-dimensional imaging of coal using microfocus X-ray computed tomography, with special reference to modes of mineral occurrence. *International Journal of Coal Geology*, 113, 97-108.

Golde, R.H., (1977). The lightning protection of tall structures. In: Hughes, J. ed. *Review of Lightning Protection Technology for Tall Structures*, Arlington, Virginia: Publication no. AD-A075 449, Office of Naval Research, pp. 242–9.

Golde, R.H., and Lee, W.R., (1976). Death by lightning. *Proceedings of the Institution of Electrical Engineers,* 123, 1163.

Gomes, C., (2012). Lightning Safety of Animals. *International Journal of Biometereology*, 56, pp. 1011-23.

Gookin, J., (2010). Backcountry Lightning Risk Management. In *21st International Lightning Detection Conference, Orlando, Florida, USA.*

Hanson, G.C. and McIlwraith, G.R., (1973). Lightning Injury : Two Case Histories and a Review of Management, *British Medical Journal*, 4, 271–4.

Harris, R. J. (1975). A Primer of Multivariate Statistics. New York, Academic Press.

Hauschild, W. and Lemke, E., (2014). Basic High-Voltage Test Techniques. In: Hauschild, W. and Lemke, E., eds. Berlin: Springer Berlin Heidelberg. pp.17-80

Hendry, J. (1993). Planning for lightning. *Weatherwise,* 45, pp. 19.

Hillier, M.L., and Bell, L.S., (2007). Differentiating human bone from animal bone: a review of histological methods. *Journal of Forensic Sciences,* 52, 249-63.

Hodgson, A.W.E., (2001). Electrochemical Methods. In: Spencer, N.D. and Moore, J.H., Encyclopaedia of Chemical Physics and Physical Chemistry: Applications, London: Taylor and Francis.

Hoffman, J.W. and De Beer, F.C. (2012). Characteristics of the Micro-Focus X-ray Tomography Facility (MIXRAD) at Necsa in South Africa. In: 18th World Conference on Nondestructive Testing, Durban, South Africa

Holle, R.L., (2008). Annual rates of lightning fatalities by country. In *20th International Lightning Detection Conference*. Tucson, Arizona, USA, pp. 1–14.

Holle, R.L., López, R.E., and Navarro, B.C., (2005). Deaths, injuries, and damages from lightning in the United States in the 1890s in comparison with the 1990s. Journal of Applied Meteorology, 44, 1563-73.

Jandrell, I.R., Blumenthal, R., Anderson, R.B., *et al.* (2009). Recent lightning research in South Africa with a special focus on keraunopathology. In: *16th International Symposium on High Voltage Engineering,* Johannesburg, South Africa.

Jepsen, K.J., Davy, D.T., and Akkos, O., (2001). Observations of Damage in Bone. In: Cowin, S.C., ed. *Bone Biomechanics Handbook.* Boca Raton, London, New York, Washington D.C.: CRC Press. pp. 17-1 - 17-15.

Kannan, R.Y., Chester, D.L. *et al*. (2004). Combined Bennet's fracture subluxation ad scapho-trapezio-trapezoidal dislocation secondary to lightning strike, *The Journal of Trauma*, 57. pp. 1351-53.

Kerr, J.B., (2010). Skeletal Tissues. In: Kerr, J.B. ed. Functional Histology: 2nd ed. Sydney: Elsevier Mosby. pp. 223-56.

Kind, D. (1978). An introduction to high-voltage experimental technique: Textbook for electrical engineers. Braunschweig, W. Germany: Friedr. Vieweg

Kitagawa, N., Brook, M., and Workman, E.J. (1962). Continuing currents in cloud-to-ground lightning discharges. *Journal of Geophysics Research.* 67, pp. 637–47.

Kotak, B. P., Haddo, O., Iqbal, M., *et al.* (2000). Bilateral scapular fractures after electrocution. *Journal of the Royal Society of Medicine*. 93, pp. 143-4.

Lane, N.E., (2006). Epidemiology, aetiology, and diagnosis of osteoporosis. *American journal of obstetrics and gynaecology*, 194, pp. 3-11.

Lee, Y.H. (2015). The simulated effect of the lightning first short stroke current on a multi-layered cylindrical model of the human leg. MSc dissertation, Johannesburg, University of the Witwatersrand.

Lifschultz, B.D. and Donoghue, E.R., (1993). Deaths caused by lightning. *Journal of forensic sciences*, 38, pp. 353–8.

Linting, M., and van der Kooij, A., (2012). Nonlinear Principal Components Analysis with CATPCA. Journal of Personality Assessment, 94, pp. 12-25.

Leveling, A., (2002). The relationship between pH and conductivity in a Lithium contaminated De-ionazied water system, Pbar Note 674. [Online] Available from: http://pbar.fnal.gov/documents/pbarnotes/pdf_files/PB674.pdf [Accessed 29 March 2016]

Lyman, R. L., (2004). The concept of equifinality in taphonomy. *Journal of Taphonomy*,

2, pp. 15–26.

Maat, G.J.R., Van Den Bos, R.P.M., and Aarents, M.J., (2001). Manual preparation of ground sections for the microscopy of natural bone tissue: update and modification of Frost's ‘rapid manual method’. *International Journal of Osteoarcheology*, 11, pp. 366-74.

Malan, D.J. (1963). *Physics of Lightning*, The English Universities Press Limited, London, UK, p. 164.

Marshall, T.C., and Stolzenburg, M. (2001). Voltages inside and just above thunderstorms. *Journal of Geophysics Research,* 106, pp. 4757–68.

Martin, R.B., Holt, D.H., and Advani, S. (1979). Anomalous Piezoelectric Behaviour in Dry Bone. In: Brighton, C.T., Black, C.T., and Pollack, S.R., eds. Electrical Properties of Bone and Cartilage: Experimental Effects and Clinical Applications, pp. 31-45.

Martiniakova, M., Grosskopf, B., Omelka, R., *et al.* (2006). Histological study of compact bone tissue in some mammals: a method for species determination. *International Journal of Osteoarcheology,* 17, 82-90.

McElhaney, J., Fogle, J., Byars, E., *et al*., (1964). Effect of embalming on the mechanical properties of beef bone. *Journal of Applied Physiology*, 19, pp.1234–6.

Mellen, P.F., Weedn, V.W. and Kao, G., (1992). Electrocution: a review of 155 cases with emphasis on human factors. *Journal of forensic sciences*, 37, 1016–22.

Mescher, A., (2009a). Bone. In: Mescher, A., ed. *Junqueira's Basic Histology: Text and Atlas, 12th Ed.*: USA: McGraw-Hill Education. pp. 121-34.

Mescher, A., (2009b). Nervous Tissue and the Nervous System. In: Mescher, A., ed. Junqueira's Basic Histology: Text and Atlas, 12th Ed.: USA: McGraw-Hill Education. pp. 140-66.

Mescher, A., (2009c). Muscle Tissue. In: Mescher, A., ed. *Junqueira's Basic Histology: Text and Atlas, 12th Ed.*: USA: McGraw-Hill Education. pp. 167-84.

Mitchell, E.K. and Davis, J.H., (1984). Electrocution by street lighnting. *Journal of forensic sciences*, 29, pp.836–42.

Nakahori, K., Egawa, T., and Mitani, H. (1982). Characteristics of winter lightning currents in Hokuriku district. *IEEE Transactions* on Power *Apparatus* and *Systems.* 101, pp. 4407–12.

Nelson, R. (1992). A microscopic comparison of fresh and burned bone. *Journal of Forensic Science*, 37, 1055-60.

O'Keefe Gatewood, M. and Zane, R.D., (2004). Lightning injuries. *Emergency medicine clinics of North America*, 22, 369–403.

Ohman, C., Dall'Ara, E., Baleani, M., *et al*. (2008). The effects of embalming using a 4% formalin solution on the compressive mechanical properties of human cortical bone. *Clinical biomechanics,* 23, pp.1294–8.

Orville, R.E. (1968). A high-speed time-resolved spectroscopic study of the lightning return stroke: Part II, A quantitative analysis. *Journal of Atmospheric Science,* 25, pp. 839–51.

Orville, R.E., Uman, M.A., and Sletten, A.M. (1967). Temperature and electron density in long air sparks. *Journal of Applied Physics,* 38, pp.895–6.

Pfortmueller, C. A., Yikun, Y. Haberkern, M. *et al*., (2012). Injuries, sequelae, and treatment of lightning-induced injuries: 10 years of experience at a swiss trauma center. *Emergency medicine international*, 2012, 1-6.

Randolph-Quinney, P.S., (2014a).Burnt human remains I: fire dynamics and body recovery. In X. Mallett and T. Blythe eds. Advances in Human Identification. Boca Raton: CRC Press. pp. 127-44.

Randolph-Quinney, P.S., (2014b). Burnt human remains II: identification and laboratory analysis. In X. Mallett and T. Blythe eds. Advances in Human Identification. Boca Raton: CRC Press. pp. 145-64.

Rakov, V.A., and Uman, M.A., (2003a). Incidence of lightning. In: Rakov, V.A., and Uman, M.A., eds. Lightning Physics and Effects. Cambridge: Cambridge University Press. pp. 24-52

Rakov, V.A., and Uman, M.A., (2003b). Downward negative lightning discharges to ground. In: Rakov, V.A., and Uman, M.A., eds. Lightning Physics and Effects. Cambridge: Cambridge University Press. pp. 108-90.

Rakov, V.A., Uman, M.A., Hoffman, G.R., et al. (1996). Bursts of pulses in lightning electromagnetic radiation: observations and implications for lightning test standards. IEEE Trans. Electromagn. Compat. 38, 156–64.

Reazer, J.S., Serrano, A.V., Walko, L.C., et al. (1987). Analysis of correlated electromagnetic fields and current pulses during airborne lightning attachments. *Electromagnetics,* 7, pp. 509–39.

Reinish, G.B., and Nowick, A.S., (1979). A model for dielectric behaviour of wet bone. In: Brighton, C.T., Black, C.T., and Pollack, S.R., eds. Electrical Properties of Bone and Cartilage: Experimental Effects and Clinical Applications, pp.31-45.

Ross, M.H., and Pawlina, W., (2006). Bone. In: Ross, M.H., and Pawlina, W., eds. Histology: a text and atlas: with correlated cell and molecular biology, 5th ed. Baltimore: Lippincott Wiliams and Wilkins. pp. 218-32

Saha, S., and Williams, P.A., (1988). Effects of various storage methods on the dielectric properties of compact bone. *Medical and Biological Engineering and Computing*, 26, 199-202.

Schmidt, C.W. and Symes, S.A. (2008). Analysis of Burned Human Remains. London: Academic Press, Elsevier

Schon, K., (2013). Characterisation and Generation of High Impulse Voltages and Currents. In: Schon, K., ed. High Impulse Voltage and Current Measurement Techniques. Switzerland: Springer International Publishing, pp. 5-38.

Schonland, B.F.J., (1964). *The Flight of Thunderbolts*, 2nd ed., Oxford: Clarendon Press. pp.182.

Sellers, E., Vervoort, A. and Van Cleynenbreugel, J., (2003). Three-dimensional visualization of fractures in rock test samples, simulating deep level mining excavations, using X-ray computed tomography. *Geological Society, London, Special Publications*, 215, 69–80.

Shipp, M., (2004). The use of laboratory reconstruction in fire investigation. In: Daeid N.N. ed. Fire Investigaation. Bocca Raton: CRC Press. pp. 104-35.

Skoog, D. A., Holler, F. J., & Crouch, S. R. (2007). *Instrumental analysis*. Cengage Learning India, p. 9.

Sutherland, A., (2009) Quantitative and Qualitative Analysis of Heat Induced Changes to Embalmed Porcine Bone. MSc dissertation, Glasgow, Scotland, University of Strathclyde.

Sterchi, D.L. (2013). Bone. In: Suvarna, S.K., Layton, C., and Bancroft, J.D., eds. Bancroft's Theory and Practice of Histological Techniques.

Vance, E.F. (1980). Electromagnetic interference control. *IEEE Transactions on Electromagnetic Compatibility.* 22, 319–28.

Vandersteen, K., Busselen, B. and Abeele, K.V.D. (2003). Quantitative characterization of fracture apertures using microfocus computed tomography. *Geological Society, London , Special Publications*, 215, 61–68.

Viljoen, J., Campbell, Q.P., Le Roux, M., *et al.* (2015). An Analysis of the Slow Compression Breakage of Coal Using Microfocus X-Ray Computed Tomography. *International Journal of Coal Preparation and Utilization*, 35, 1-13.

Vuille, C., Serway, R.A., and Faughn, J.S. (2009a). Energy. In: Vuille, C., Serway, R.A., and Faughn, J.S. eds. College Physics. Canda: Brooks/Cole Cengage Learning. pp. 141-2.

Vuille, C., Serway, R.A., and Faughn, J.S. (2009b). Energy in Thermal Processes. In: Vuille, C., Serway, R.A., and Faughn, J.S. eds. College Physics. Canda: Brooks/Cole Cengage Learning. pp. 355.

Uman, M.A., (2001). The lightning discharge. Mineola, New York: Dover Publications. pp. 376-78.

Wieland, D.C.F. Krywkaa, C., Mick, E., *et al.* (2015). Investigating the inverse piezoelectric effect of trabecular bone on a micrometre length scale using synchrotron radiation. *Acta Biomaterialia,* 25, 339-46.

Wright, R.K. and Davis, J.H. (1980). The Investigation of Electrical Deaths: A Report of 220 Fatalities. *Journal of forensic sciences*, 25, 514–21.

APPENDIX A: Recipes

A1: Solution Constitution:

Embalming Fluid:

Alcohol: 84.706%

Glycerine: 9.412%

Formalin: 4.706%

Phenol: 1.176%

Thymol: 0.001%

Isotonic Saline:

Distilled water: 99.1%

NaCl: 0.9%

A2: Staining Solutions:

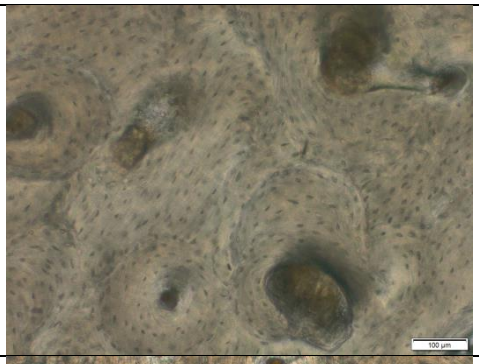
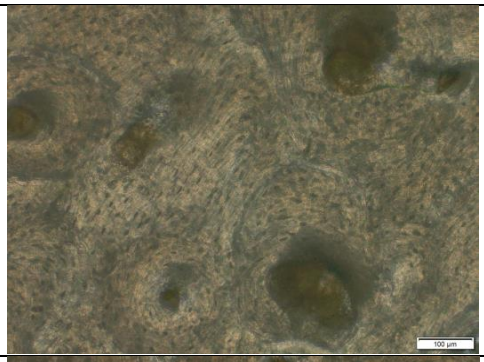
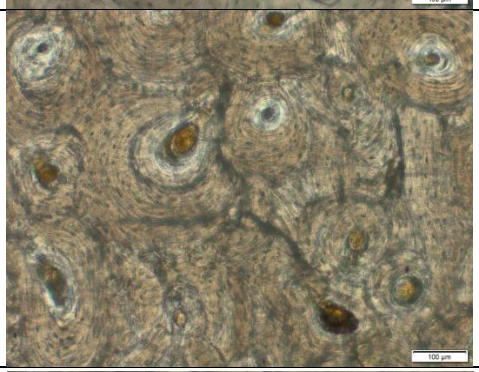
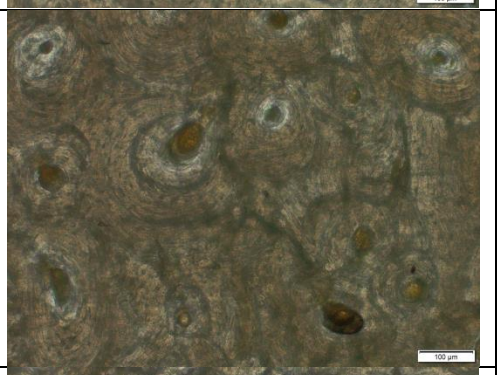
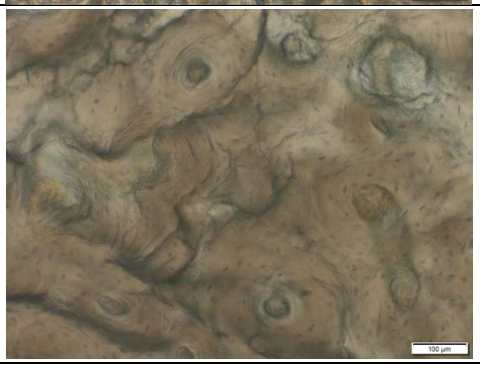
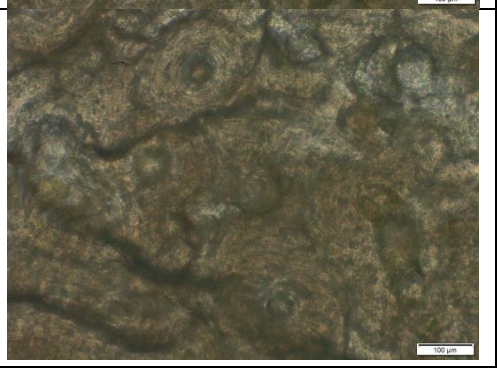
1. Stable Iron Hematoxylin:
    a. Solution A:
        i. Haematoxylin powder - 1g
        ii. 95% alcohol - 100ml
    b. Solution B:
        i. Aluminium chloride hexahydrate ($H_{12}AlCl_3O_6$) - 10g
        ii. Ferrous sulphate hydrate ($FeSO_4 \cdot xH_2O$) - 10g
        iii. Distilled water - 100ml
    c. Mix solutions A and B then add:
        i. HCl - 2ml

ii. 9% Sodium iodate ($NaIO_3$) solution - 2ml

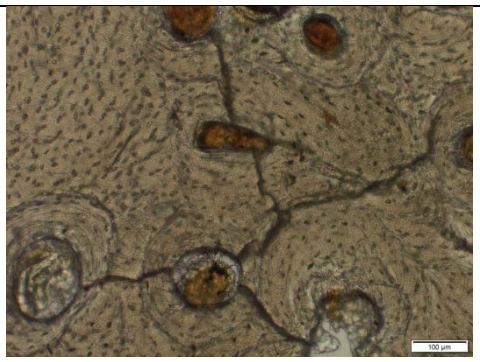
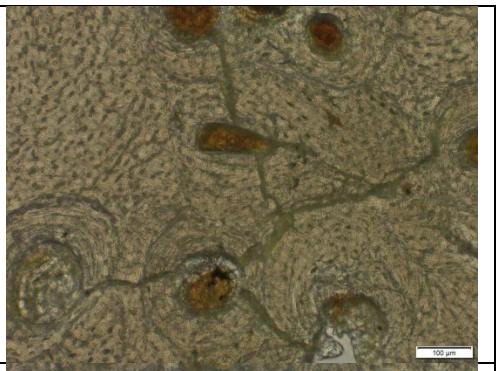
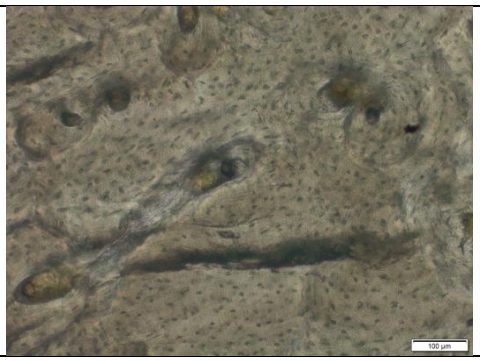
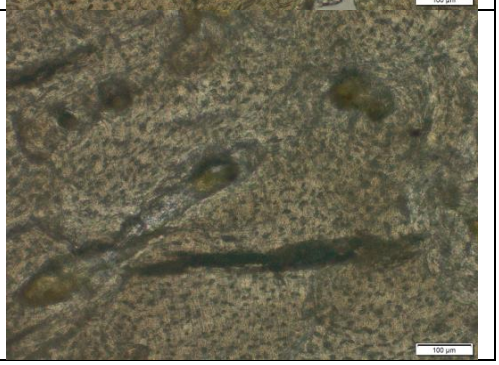
2. Fuchsin Ponceau:
    a. Fuchsin acid - 0.1g
    b. Ponceau S – 0.2g
    c. Distilled water – 200ml
    d. Acetic acid - 0.4ml
3. Methyl Blue
    a. Methyl blue – 2g
    b. Acetic acid – 2ml
    c. Distilled water – 100ml

APPENDIX B: Original Qualitative Analysis Photomicrographs

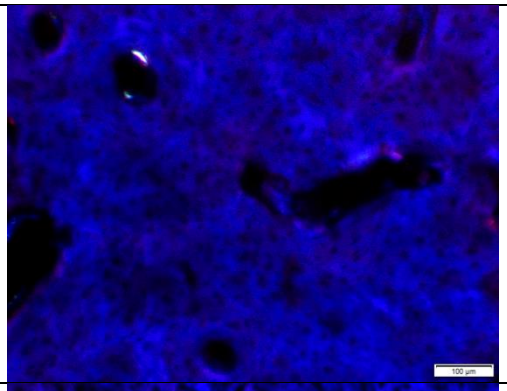
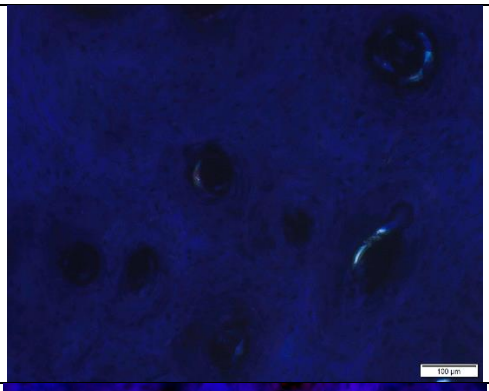
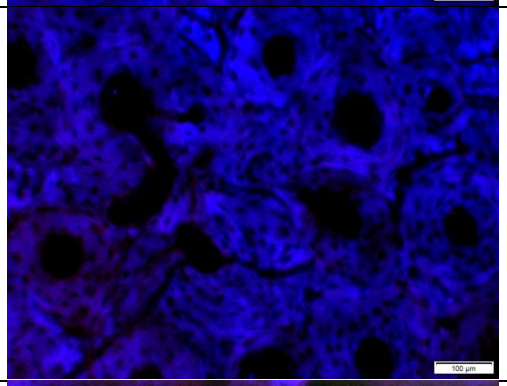
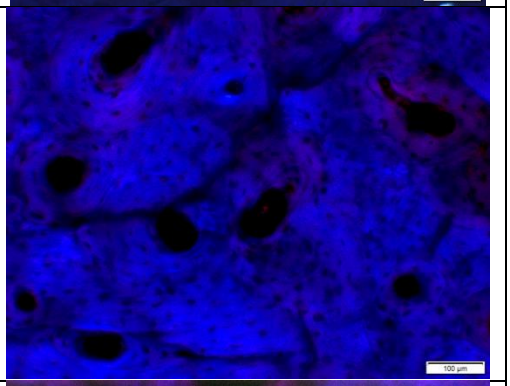
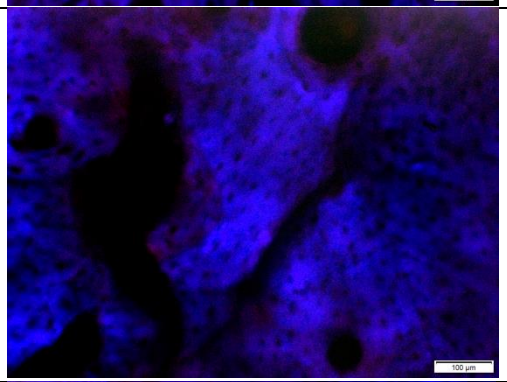
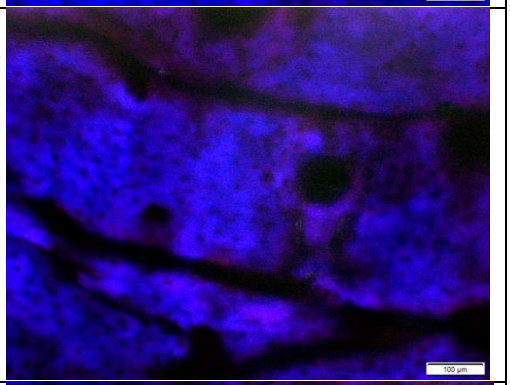
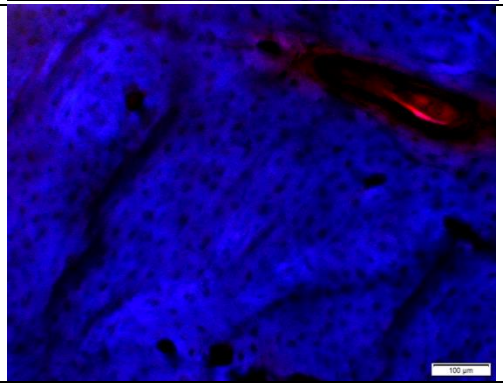
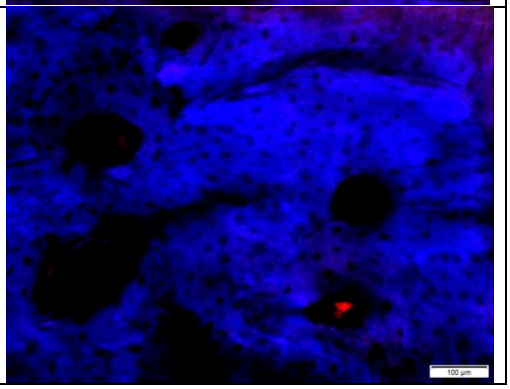
APPENDIX Table B1.1: Unstained Original Photomicrographs Part 1

Charging Voltage	Bright Field	Polarised Light
Control		
3.5Kv PPM		
4Kv WDM		

APPENDIX Table B1.2: Unstained Original Photomicrographs Part 2

6Kv WDM		
6.5Kv PPM		

APPENDIX Table B2: Stained Original Photomicrographs

Charging Voltage	First Photomicrograph	Second Photomicrograph
Control		
3.5Kv PPM		
6kV WDM		
10kV PPM		

APPENDIX C: Descriptive Statistics

Table C1: Depiction of the Descriptive Statistics Pertinent to the Individual Micro-Fracture Data Set

Variable	N	Min.	Max.	Mean	Std. Error	Std. Deviation
FT	98	0	4	1.99	.114	1.126
pV	98	1.1200	7.040	4.520	.196	1.937
pC	98	.000	9.440	4.959	.405	4.014
Potential	98	3.5	6.5	5.388	.124	1.226
FW	98	0	23.229	8.617	.422	4.182
FL	98	0	1099.488	259.529	19.060	188.683
FP	98	0	4310.435	578.999	54.156	536.122
FA	98	0	10924.400	2214.527	221.830	2196.002

Table C2: Depiction of the Descriptive Statistics Pertinent to the Total Fracture Data Set

Variable	N	Min.	Max.	Mean	Std. Error	Std. Deviation
pV	34	.000	7.040	4.735588	.3379977	1.971
pC	34	.000	9.440	4.810588	.7287414	4.249
CP	34	0	6.5	4.941	.2677	1.5607
FN	34	0	7	2.85	.356	2.076
TFA	34	.000	27034.552	6398.061	1221.640	7123.324
TFA/TBA	34	.000	.0568	.011	.002	.0132

APPENDIX D: Intraclass Correlation Repeatability Test Results

APPENDIX D1: Two-way Mixed Intraclass Correlation Repeatability Test Results for Inter-observer Trials

Table D1.1: Tabulation of Two-way mixed Intraclass Correlation Coefficients for Repeatability of Inter-observer Trials in Regards to Fracture Number

Intraclass correlation coefficient (ICC) for fracture number measurements was identified as a moderate statistically insignificant correlation (.590, p=0.183) with an extremely high range of ICCs between the lower and higher bounds of the trial measurements, further demonstrating the unreliability of the observers.

	Intraclass	95% Confidence Interval		F Test with True Value 0			
	Correlation	Lower Bound	Upper Bound	Value	df1	df2	Sig
Single Measures	.223	-.192	.955	2.116	2	8	.183
Average. Measures	.590	-4.134	.991	2.116	2	8	.183

Table D1.2: Tabulation of Two-way mixed Intraclass Correlation Coefficients for Repeatability of Inter-observer Trials in Regards to Total Fracture Area

Intraclass correlation coefficient (ICC) for total fracture area measurements was identified as a weak statistically insignificant correlation (.227, p=0.183) with a high range of ICCs between the lower and higher bounds of trial measurements, further demonstrating the unreliability of the observers.

	Intraclass	95% Confidence Interval		F Test with True Value 0			
	Correlation	Lower Bound	Upper Bound	Value	df1	df2	Sig
Single Measures	.055	-.033	.814	2.090	2	8	.186
Average Measures	.227	-.191	.956	2.090	2	8	.186

Table D1.3: Tabulation of Two-way mixed Intraclass Correlation Coefficient for Repeatability of Inter-observer Trials in Regards to Total Bone Area

Intraclass correlation coefficient (ICC) for total bone area measurements was identified as an excellent statistically significant correlation (.995, p=0.000) with a very low range of ICCs between the lower and higher bounds of trial measurements, demonstrating the reliability when the measurement nature is simple and explicit for observers.

	Intraclass Correlation	95% Confidence Interval		F Test with True Value 0			
		Lower Bound	Upper Bound	Value	df1	df2	Sig
Single Measures	.975	.876	.999	288.676	2	8	.000
Average Measures	**.995**	**.972**	**1.000**	288.676	2	8	**.000**

Table D1.4: Tabulation of Two-way mixed Intraclass Correlation Coefficient for Repeatability of Inter-observer Trials in Regards to Total Fracture Area over Total Bone Area

Intraclass correlation coefficient (ICC) for total fracture area over total bone area ratios were identified as very weak statistically insignificant correlation (.178, p=0.226) with a fairly high range of ICCs between the lower and higher bounds of trial measurements, demonstrating the unreliability of the observers based on the total fracture area component of the ratio calculated despite the high precision of the total bone area.

	Intraclass Correlation	95% Confidence Interval		F Test with True Value 0			
		Lower Bound	Upper Bound	Value	df1	df2	Sig
Single Measures	.042	-.036	.791	1.802	2	8	.226
Average Measures	.178	-.212	.950	1.802	2	8	.226

APPENDIX D2: Two-way Mixed Intraclass Correlation Repeatability Test Results for Intra-observer Trials

Table D2.1: Tabulation of Two-way mixed Intraclass Correlation Coefficient for Repeatability of Intra-observer Trials in Regards to Fracture Number

Intraclass correlation coefficient (ICC) for fracture number was identified as exceptionally strong statistically significant correlation (.976, p=0.000) with a particularly tight range of ICCs between the lower and higher bounds of trial measurements, demonstrating the high reliability of measurements obtained by the principal investigator as trained in the methodology and bone histology.

	Intraclass Correlation	95% Confidence Interval		F Test with True Value 0			
		Lower Bound	Upper Bound	Value	df1	df2	Sig
Single Measures	.891	.591	.997	43.619	2	8	.000
Average Measures	**.976**	**.878**	**.999**	43.619	2	8	**.000**

Table D2.2: Tabulation of Two-way mixed Intraclass Correlation Coefficient for Repeatability of Intra-observer Trials in Regards to Total Fracture Area

Intraclass correlation coefficient (ICC) for total fracture area was identified as an excellent statistically significant correlation (.979, p=0.000) with a particularly tight range of ICCs between the lower and higher bounds of trial measurements, demonstrating the high reliability of measurements obtained by the principal investigator as trained in the methodology and bone histology.

	Intraclass Correlation	95% Confidence Interval		F Test with True Value 0			
		Lower Bound	Upper Bound	Value	df1	df2	Sig
Single Measures	.901	.591	.997	89.476	2	8	.000
Average Measures	**.979**	**.878**	**.999**	89.476	2	8	**.000**

Table D2.3: Tabulation of Two-way mixed Intraclass Correlation Coefficient for Repeatability of Intra-observer Trials in Regards to Total Bone Area

Intraclass correlation coefficient (ICC) for total bone area was identified as an outstandingly strong statistically significant correlation (.998, p=0.000) with an extraordinarily tight range of ICCs between the lower and higher bounds of trial measurements, demonstrating the high reliability of measurements obtained by the principal investigator as trained in the methodology and bone histology, even more so with the most explicit and simple measurement.

	Intraclass Correlation	95% Confidence Interval		F Test with True Value 0			
		Lower Bound	Upper Bound	Value	df1	df2	Sig
Single Measures	.992	.957	1.000	862.968	2	8	.000
Average Measures	**.998**	**.991**	**1.000**	862.968	2	8	**.000**

Table D2.4: Tabulation of Two-way mixed Intraclass Correlation Coefficient for Repeatability of Intra-observer Trials in Regards to Total Fracture Area over Total Bone Area

Intraclass correlation coefficient (ICC) for total fracture area over total bone area was identified as an outstandingly strong statistically significant correlation (.979, p=0.000) with a particularly tight range of ICCs between the lower and higher bounds of trial measurements, demonstrating the high reliability of measurements obtained by the principal investigator as trained in the methodology and bone histology.

	Intraclass Correlation	95% Confidence Interval		F Test with True Value 0			
		Lower Bound	Upper Bound	Value	df1	df2	Sig
Single Measures	.902	.594	.997	90.386	2	8	.000
Average Measures	**.979**	**.880**	**.999**	90.386	2	8	**.000**

APPENDIX E: Kruskal-Wallis ANoVA by Ranks Results

APPENDIX E1: Kruskal-Wallis ANoVA by Ranks on the Individual Fracture Data

Kruskal-Wallis ANOVA by Ranks; FA
Independent (grouping) variable: Potential
Kruskal-Wallis test: H (3, N= 98) =10,41140 p =,0154

Depend.: FA	Code	Valid N	Sum of Ranks	Mean Rank
1	1	15	832,500	55,50000
2	2	20	665,000	33,25000
3	3	28	1654,000	59,07143
4	4	35	1699,500	48,55714

Kruskal-Wallis ANOVA by Ranks; FL
Independent (grouping) variable: Potential
Kruskal-Wallis test: H (3, N= 98) =9,372622 p =,02

Depend.: FL	Code	Valid N	Sum of Ranks	Mean Rank
1	1	15	929,500	61,96667
2	2	20	701,000	35,05000
3	3	28	1550,000	55,35714
4	4	35	1670,500	47,72857

Kruskal-Wallis ANOVA by Ranks; FP
Independent (grouping) variable: Potential
Kruskal-Wallis test: H (3, N= 98) =10,32662 p =,01

Depend.: FP	Code	Valid N	Sum of Ranks	Mean Rank
1	1	15	903,500	60,23333
2	2	20	686,000	34,30000
3	3	28	1611,000	57,53571
4	4	35	1650,500	47,15714

Kruskal-Wallis ANOVA by Ranks; FW
Independent (grouping) variable: Potential
Kruskal-Wallis test: H (3, N= 98) =3,625103 p =,30

Depend.: FW	Code	Valid N	Sum of Ranks	Mean Rank
1	1	15	612,500	40,83333
2	2	20	875,500	43,77500
3	3	28	1439,000	51,39286
4	4	35	1924,000	54,97143

	Kruskal-Wallis ANOVA by Ranks; FA Independent (grouping) variable: Mode Kruskal-Wallis test: H (1, N= 98) =,1640930 p =,68			
Depend.: FA	Code	Valid N	Sum of Ranks	Mean Rank
1	1	50	2532,00(	50,6400(
2	2	48	2319,00(	48,3125(

	Kruskal-Wallis ANOVA by Ranks; FL Independent (grouping) variable: Mode Kruskal-Wallis test: H (1, N= 98) =,7891464 p =,37			
Depend.: FL	Code	Valid N	Sum of Ranks	Mean Rank
1	1	50	2600,00(	52,0000(
2	2	48	2251,00(	46,8958:

	Kruskal-Wallis ANOVA by Ranks; FP Independent (grouping) variable: Mode Kruskal-Wallis test: H (1, N= 98) =,3152040 p =,57			
Depend.: FP	Code	Valid N	Sum of Ranks	Mean Rank
1	1	50	2554,00(	51,0800(
2	2	48	2297,00(	47,8541:

	Kruskal-Wallis ANOVA by Ranks; FW Independent (grouping) variable: Mode Kruskal-Wallis test: H (1, N= 98) =,1910629 p =,66			
Depend.: FW	Code	Valid N	Sum of Ranks	Mean Rank
1	1	50	2536,50(	50,7300(
2	2	48	2314,50(	48,2187:

	Kruskal-Wallis ANOVA by Ranks; FA Independent (grouping) variable: pC Kruskal-Wallis test: H (7, N= 98) =14,05930 p =,05			
Depend.: FA	Code	Valid N	Sum of Ranks	Mean Rank
1	1	15	832,50(	55,5000(
2	2	9	231,00(	25,6666:
3	3	22	1133,00(	51,5000(
4	4	14	885,00(	63,2142:
5	5	3	70,00(	23,3333:
6	6	8	317,50(	39,6875(
7	7	16	843,50(	52,7187:
8	8	11	538,50(	48,9545:

	Kruskal-Wallis ANOVA by Ranks; FL Independent (grouping) variable: pC Kruskal-Wallis test: H (7, N= 98) =10,90958 p =,14			
Depend.: FL	Code	Valid N	Sum of Ranks	Mean Rank
1	1	15	929,500	61,96667
2	2	9	278,000	30,88889
3	3	22	1036,000	47,09091
4	4	14	837,000	59,78571
5	5	3	100,000	33,33333
6	6	8	352,500	44,06250
7	7	16	850,000	53,12500
8	8	11	468,000	42,54545

	Kruskal-Wallis ANOVA by Ranks; FW Independent (grouping) variable: pC Kruskal-Wallis test: H (7, N= 98) =18,20052 p =,01			
Depend.: FW	Code	Valid N	Sum of Ranks	Mean Rank
1	1	15	612,500	40,83333
2	2	9	295,000	32,77778
3	3	22	1102,000	50,09091
4	4	14	885,000	63,21429
5	5	3	32,500	10,83333
6	6	8	316,500	39,56250
7	7	16	899,500	56,21875
8	8	11	708,000	64,36364

	Kruskal-Wallis ANOVA by Ranks; FA Independent (grouping) variable: pV Kruskal-Wallis test: H (8, N= 98) =15,79126 p =,04			
Depend.: FA	Code	Valid N	Sum of Ranks	Mean Rank
1	1	16	843,500	52,71875
2	2	6	404,000	67,33333
3	3	9	428,500	47,61111
4	4	9	231,000	25,66667
5	5	22	1133,000	51,50000
6	6	14	885,000	63,21429
7	7	3	70,000	23,33333
8	8	8	317,500	39,68750
9	9	11	538,500	48,95455

	Kruskal-Wallis ANOVA by Ranks; FL Independent (grouping) variable: pV Kruskal-Wallis test: H (8, N= 98) =12,28190 p =,13			
Depend.: FL	Code	Valid N	Sum of Ranks	Mean Rank
1	1	16	850,000	53,12500
2	2	6	435,000	72,50000
3	3	9	494,500	54,94444
4	4	9	278,000	30,88889
5	5	22	1036,000	47,09091
6	6	14	837,000	59,78571
7	7	3	100,000	33,33333
8	8	8	352,500	44,06250
9	9	11	468,000	42,54545

	Kruskal-Wallis ANOVA by Ranks; FW Independent (grouping) variable: pV Kruskal-Wallis test: H (8, N= 98) =18,25859 p =,01			
Depend.: FW	Code	Valid N	Sum of Ranks	Mean Rank
1	1	16	899,500	56,21875
2	2	6	258,000	43,00000
3	3	9	354,500	39,38889
4	4	9	295,000	32,77778
5	5	22	1102,000	50,09091
6	6	14	885,000	63,21429
7	7	3	32,500	10,83333
8	8	8	316,500	39,56250
9	9	11	708,000	64,36364

	Kruskal-Wallis ANOVA by Ranks; FP Independent (grouping) variable: pV Kruskal-Wallis test: H (8, N= 98) =12,14467 p =,14			
Depend.: FP	Code	Valid N	Sum of Ranks	Mean Rank
1	1	16	825,000	51,56250
2	2	6	420,000	70,00000
3	3	9	483,500	53,72222
4	4	9	273,000	30,33333
5	5	22	1036,000	47,09091
6	6	14	878,000	62,71429
7	7	3	110,000	36,66667
8	8	8	348,500	43,56250
9	9	11	477,000	43,36364

	Kruskal-Wallis ANOVA by Ranks; FP Independent (grouping) variable: pC Kruskal-Wallis test: H (7, N= 98) =10,96485 p =,14			
Depend.: FP	Code	Valid N	Sum of Ranks	Mean Rank
1	1	15	903,500	60,23333
2	2	9	273,000	30,33333
3	3	22	1036,000	47,09091
4	4	14	878,000	62,71429
5	5	3	110,000	36,66667
6	6	8	348,500	43,56250
7	7	16	825,000	51,56250
8	8	11	477,000	43,36364

APPENDIX E2: Multiple Variable Comparison Post-Hoc Test Results of the Individual Fracture Data Set for Charging Potential Grouping

	Multiple Comparisons z' values; FA Independent (grouping) variable: Potential Kruskal-Wallis test: H (3, N= 98) =10,41140 p =,01			
Depend.: FA	1 R:55,500	2 R:33,250	3 R:59,071	4 R:48,557
1		2,290955	0,392548	0,791212
2	2,290955		3,101799	1,920533
3	0,392548	3,101799		1,458420
4	0,791212	1,920533	1,458420	

	Multiple Comparisons p values (2-tailed); FA Independent (grouping) variable: Potential Kruskal-Wallis test: H (3, N= 98) =10,41140 p =,01			
Depend.: FA	1 R:55,500	2 R:33,250	3 R:59,071	4 R:48,557
1		0,131796	1,000000	1,000000
2	0,131796		0,011541	0,328744
3	1,000000	0,011541		0,868349
4	1,000000	0,328744	0,868349	

	Multiple Comparisons z' values; FL Independent (grouping) variable: Potential Kruskal-Wallis test: H (3, N= 98) =9,372622 p =,02			
Depend.: FL	1 R:61,967	2 R:35,050	3 R:55,357	4 R:47,729
1		2,771455	0,726475	1,622582
2	2,771455		2,439395	1,590736
3	0,726475	2,439395		1,058147
4	1,622582	1,590736	1,058147	

	Multiple Comparisons p values (2-tailed); FL Independent (grouping) variable: Potential Kruskal-Wallis test: H (3, N= 98) =9,372622 p =,02			
Depend.: FL	1 R:61,967	2 R:35,050	3 R:55,357	4 R:47,729
1		0,033484	1,000000	0,628073
2	0,033484		0,088271	0,670015
3	1,000000	0,088271		1,000000
4	0,628073	0,670015	1,000000	

	Multiple Comparisons z' values; FP Independent (grouping) variable: Potential Kruskal-Wallis test: H (3, N= 98) =10,32662 p =,01			
Depend.: FP	1 R:60,233	2 R:34,300	3 R:57,536	4 R:47,157
1		2,670207	0,296504	1,490170
2	2,670207		2,791190	1,613140
3	0,296504	2,791190		1,439595
4	1,490170	1,613140	1,439595	

	Multiple Comparisons p values (2-tailed); FP Independent (grouping) variable: Potential Kruskal-Wallis test: H (3, N= 98) =10,32662 p =,01			
Depend.: FP	1 R:60,233	2 R:34,300	3 R:57,536	4 R:47,157
1		0,045483	1,000000	0,817077
2	0,045483		0,031509	0,640284
3	1,000000	0,031509		0,899892
4	0,817077	0,640284	0,899892	

	Multiple Comparisons z' values; FW Independent (grouping) variable: Potential Kruskal-Wallis test: H (3, N= 98) =3,625103 p =,30			
Depend.: FW	1 R:40,833	2 R:43,775	3 R:51,393	4 R:54,971
1		0,302887	1,160633	1,611185
2	0,302887		0,915095	1,404776
3	1,160633	0,915095		0,496378
4	1,611185	1,404776	0,496378	

	Multiple Comparisons p values (2-tailed); FW Independent (grouping) variable: Potential Kruskal-Wallis test: H (3, N= 98) =3,625103 p =,30			
Depend.: FW	1 R:40,833	2 R:43,775	3 R:51,393	4 R:54,971
1		1,000000	1,000000	0,642836
2	1,000000		1,000000	0,960527
3	1,000000	1,000000		1,000000
4	0,642836	0,960527	1,000000	

APPENDIX E3: Multiple Variable Comparison Post-Hoc Test Results of the Individual Fracture Data Set Grouped for Peak Current

	Multiple Comparisons z' values; FA Independent (grouping) variable: pC Kruskal-Wallis test: H (7, N= 98) =14,05930 p =,0501							
Depend.: FA	1 R:55,500	2 R:25,667	3 R:51,500	4 R:63,214	5 R:23,333	6 R:39,688	7 R:52,719	8 R:48,955
1		2,488416	0,420123	0,730073	1,788694	1,270244	0,272160	0,579903
2	2,488416		2,296107	3,090749	0,123091	1,014789	2,283347	1,822185
3	0,420123	2,296107		1,205036	1,609524	1,006231	0,130453	0,242424
4	0,730073	3,090749	1,205036		2,204579	1,866897	1,008621	1,244692
5	1,788694	0,123091	1,609524	2,204579		0,849567	1,642615	1,383415
6	1,270244	1,014789	1,006231	1,866897	0,849567		1,058389	0,701400
7	0,272160	2,283347	0,130453	1,008621	1,642615	1,058389		0,337993
8	0,579903	1,822185	0,242424	1,244692	1,383415	0,701400	0,337993	

	Multiple Comparisons p values (2-tailed); FA Independent (grouping) variable: pC Kruskal-Wallis test: H (7, N= 98) =14,05930 p =,0501							
Depend.: FA	1 R:55,500	2 R:25,667	3 R:51,500	4 R:63,214	5 R:23,333	6 R:39,688	7 R:52,719	8 R:48,955
1		0,359278	1,000000	1,000000	1,000000	1,000000	1,000000	1,000000
2	0,359278		0,606753	0,055903	1,000000	1,000000	0,627478	1,000000
3	1,000000	0,606753		1,000000	1,000000	1,000000	1,000000	1,000000
4	1,000000	0,055903	1,000000		0,769542	1,000000	1,000000	1,000000
5	1,000000	1,000000	1,000000	0,769542		1,000000	1,000000	1,000000
6	1,000000	1,000000	1,000000	1,000000	1,000000		1,000000	1,000000
7	1,000000	0,627478	1,000000	1,000000	1,000000	1,000000		1,000000
8	1,000000	1,000000	1,000000	1,000000	1,000000	1,000000	1,000000	

	Multiple Comparisons z' values; FL Independent (grouping) variable: pC Kruskal-Wallis test: H (7, N= 98) =10,90958 p =,1426							
Depend.: FL	1 R:61,967	2 R:30,889	3 R:47,091	4 R:59,786	5 R:33,333	6 R:44,063	7 R:53,125	8 R:42,545
1		2,592216	1,562411	0,206403	1,592216	1,438271	0,865205	1,720646
2	2,592216		1,440061	2,378655	0,128953	0,953469	1,876852	0,912081
3	1,562411	1,440061		1,305901	0,786147	0,257971	0,645879	0,432900
4	0,206403	2,378655	1,305901		1,462261	1,247668	0,640095	1,504853
5	1,592216	0,128953	0,786147	1,462261		0,557359	1,106334	0,497408
6	1,438271	0,953469	0,257971	1,247668	0,557359		0,736050	0,114821
7	0,865205	1,876852	0,645879	0,640095	1,106334	0,736050		0,949952
8	1,720646	0,912081	0,432900	1,504853	0,497408	0,114821	0,949952	

	Multiple Comparisons p values (2-tailed); FL Independent (grouping) variable: pC Kruskal-Wallis test: H (7, N= 98) =10,90958 p =,1426							
Depend.: FL	1 R:61,967	2 R:30,889	3 R:47,091	4 R:59,786	5 R:33,333	6 R:44,063	7 R:53,125	8 R:42,545
1		0,267008	1,000000	1,000000	1,000000	1,000000	1,000000	1,000000
2	0,267008		1,000000	0,486526	1,000000	1,000000	1,000000	1,000000
3	1,000000	1,000000		1,000000	1,000000	1,000000	1,000000	1,000000
4	1,000000	0,486526	1,000000		1,000000	1,000000	1,000000	1,000000
5	1,000000	1,000000	1,000000	1,000000		1,000000	1,000000	1,000000
6	1,000000	1,000000	1,000000	1,000000	1,000000		1,000000	1,000000
7	1,000000	1,000000	1,000000	1,000000	1,000000	1,000000		1,000000
8	1,000000	1,000000	1,000000	1,000000	1,000000	1,000000	1,000000	

	Multiple Comparisons z' values; FW Independent (grouping) variable: pC Kruskal-Wallis test: H (7, N= 98) =18,20052 p =,0111							
Depend.: FW	1 R:40,833	2 R:32,778	3 R:50,091	4 R:63,214	5 R:10,833	6 R:39,563	7 R:56,219	8 R:64,364
1		0,671919	0,972329	2,118113	1,668212	0,102088	1,505546	2,084696
2	0,671919		1,538818	2,505395	1,157646	0,491059	1,978549	2,471470
3	0,972329	1,538818		1,349987	2,243290	0,896847	0,655914	1,359307
4	2,118113	2,505395	1,349987		2,895567	1,876816	0,672271	0,100324
5	1,668212	1,157646	2,243290	2,895567		1,492424	2,536998	2,890365
6	0,102088	0,491059	0,896847	1,876816	1,492424		1,352809	1,877138
7	1,505546	1,978549	0,655914	0,672271	2,536998	1,352809		0,731340
8	2,084696	2,471470	1,359307	0,100324	2,890365	1,877138	0,731340	

	Multiple Comparisons p values (2-tailed); FW Independent (grouping) variable: pC Kruskal-Wallis test: H (7, N= 98) =18,20052 p =,0111							
Depend.: FW	1 R:40,833	2 R:32,778	3 R:50,091	4 R:63,214	5 R:10,833	6 R:39,563	7 R:56,219	8 R:64,364
1		1,000000	1,000000	0,956633	1,000000	1,000000	1,000000	1,000000
2	1,000000		1,000000	0,342481	1,000000	1,000000	1,000000	0,376765
3	1,000000	1,000000		1,000000	0,696587	1,000000	1,000000	1,000000
4	0,956633	0,342481	1,000000		0,105973	1,000000	1,000000	1,000000
5	1,000000	1,000000	0,696587	0,105973		1,000000	0,313061	0,107743
6	1,000000	1,000000	1,000000	1,000000	1,000000		1,000000	1,000000
7	1,000000	1,000000	1,000000	1,000000	0,313061	1,000000		1,000000
8	1,000000	0,376765	1,000000	1,000000	0,107743	1,000000	1,000000	

	Multiple Comparisons z' values; FP Independent (grouping) variable: pC Kruskal-Wallis test: H (7, N= 98) =10,96485 p =,1402							
Depend.: FP	1 R:60,233	2 R:30,333	3 R:47,091	4 R:62,714	5 R:36,667	6 R:43,563	7 R:51,563	8 R:43,364
1		2,493977	1,380357	0,234795	1,310473	1,339196	0,848488	1,494592
2	2,493977		1,489440	2,665453	0,334105	0,957490	1,791860	1,019570
3	1,380357	1,489440		1,607160	0,595671	0,300562	0,478632	0,354978
4	0,234795	2,665453	1,607160		1,439886	1,519732	1,071687	1,689063
5	1,310473	0,334105	0,595671	1,439886		0,358225	0,832662	0,361602
6	1,339196	0,957490	0,300562	1,519732	0,358225		0,649755	0,015052
7	0,848488	1,791860	0,478632	1,071687	0,832662	0,649755		0,736187
8	1,494592	1,019570	0,354978	1,689063	0,361602	0,015052	0,736187	

	Multiple Comparisons p values (2-tailed); FP Independent (grouping) variable: pC Kruskal-Wallis test: H (7, N= 98) =10,96485 p =,1402							
Depend.: FP	1 R:60,233	2 R:30,333	3 R:47,091	4 R:62,714	5 R:36,667	6 R:43,563	7 R:51,563	8 R:43,364
1		0,353698	1,000000	1,000000	1,000000	1,000000	1,000000	1,000000
2	0,353698		1,000000	0,215277	1,000000	1,000000	1,000000	1,000000
3	1,000000	1,000000		1,000000	1,000000	1,000000	1,000000	1,000000
4	1,000000	0,215277	1,000000		1,000000	1,000000	1,000000	1,000000
5	1,000000	1,000000	1,000000	1,000000		1,000000	1,000000	1,000000
6	1,000000	1,000000	1,000000	1,000000	1,000000		1,000000	1,000000
7	1,000000	1,000000	1,000000	1,000000	1,000000	1,000000		1,000000
8	1,000000	1,000000	1,000000	1,000000	1,000000	1,000000	1,000000	

APPENDIX E4: Multiple Variable Comparison Post-Hoc Test Results of the Individual Fracture Data Set Grouped for Peak Voltage

	Multiple Comparisons z' values; FA Independent (grouping) variable: pV Kruskal-Wallis test: H (8, N= 98) =15,79126 p =,0455								
Depend.: FA	1 R:52,719	2 R:67,333	3 R:47,611	4 R:25,667	5 R:51,500	6 R:63,214	7 R:23,333	8 R:39,688	9 R:48,955
1		1,07367(	0,43111:	2,28334:	0,13045:	1,00862:	1,64261!	1,05838!	0,33799:
2	1,07367(		1,31603-	2,78035:	1,20903!	0,29688(	2,18840!	1,80030(	1,27357!
3	0,43111:	1,31603-		1,63715!	0,34565:	1,28438:	1,28073(	0,57348!	0,10511(
4	2,28334:	2,78035:	1,63715!		2,29610:	3,09074!	0,12309:	1,01478!	1,82218!
5	0,13045:	1,20903!	0,34565:	2,29610:		1,20503(	1,60952-	1,00623:	0,24242-
6	1,00862:	0,29688(	1,28438:	3,09074!	1,20503(		2,20457!	1,86689:	1,24469:
7	1,64261!	2,18840!	1,28073(	0,12309:	1,60952-	2,20457!		0,84956:	1,38341!
8	1,05838!	1,80030(	0,57348!	1,01478!	1,00623:	1,86689:	0,84956:		0,70140(
9	0,33799:	1,27357!	0,10511(	1,82218!	0,24242-	1,24469:	1,38341!	0,70140(	

	Multiple Comparisons p values (2-tailed); FA Independent (grouping) variable: pV Kruskal-Wallis test: H (8, N= 98) =15,79126 p =,0455								
Depend.: FA	1 R:52,719	2 R:67,333	3 R:47,611	4 R:25,667	5 R:51,500	6 R:63,214	7 R:23,333	8 R:39,688	9 R:48,955
1		1,000000(	1,000000(	0,806757	1,000000(	1,000000(	1,000000(	1,000000(	1,000000(
2	1,000000(		1,000000(	0,195479	1,000000(	1,000000(	1,000000(	1,000000(	1,000000(
3	1,000000(	1,000000(		1,000000(	1,000000(	1,000000(	1,000000(	1,000000(	1,000000(
4	0,806757	0,195479	1,000000(		0,780111	0,071875	1,000000(	1,000000(	1,000000(
5	1,000000(	1,000000(	1,000000(	0,780111		1,000000(	1,000000(	1,000000(	1,000000(
6	1,000000(	1,000000(	1,000000(	0,071875	1,000000(		0,989411	1,000000(	1,000000(
7	1,000000(	1,000000(	1,000000(	1,000000(	1,000000(	0,989411		1,000000(	1,000000(
8	1,000000(	1,000000(	1,000000(	1,000000(	1,000000(	1,000000(	1,000000(		1,000000(
9	1,000000(	1,000000(	1,000000(	1,000000(	1,000000(	1,000000(	1,000000(	1,000000(	

	Multiple Comparisons z' values; FL Independent (grouping) variable: pV Kruskal-Wallis test: H (8, N= 98) =12,28190 p =,1391								
Depend.: FL	1 R:53,125	2 R:72,500	3 R:54,944	4 R:30,889	5 R:47,091	6 R:59,786	7 R:33,333	8 R:44,063	9 R:42,545
1		1,423397	0,153571	1,876852	0,645879	0,640095	1,106334	0,736050	0,949952
2	1,423397		1,171456	2,776646	1,940247	0,916382	1,948012	1,851859	2,075727
3	0,153571	1,171456		1,794658	0,698035	0,398511	1,140062	0,787605	0,970172
4	1,876852	2,776646	1,794658		1,440061	2,378655	0,128953	0,953469	0,912081
5	0,645879	1,940247	0,698035	1,440061		1,305901	0,786147	0,257971	0,432900
6	0,640095	0,916382	0,398511	2,378655	1,305901		1,462261	1,247668	1,504853
7	1,106334	1,948012	1,140062	0,128953	0,786147	1,462261		0,557359	0,497408
8	0,736050	1,851859	0,787605	0,953469	0,257971	1,247668	0,557359		0,114821
9	0,949952	2,075727	0,970172	0,912081	0,432900	1,504853	0,497408	0,114821	

	Multiple Comparisons p values (2-tailed); FL Independent (grouping) variable: pV Kruskal-Wallis test: H (8, N= 98) =12,28190 p =,1391								
Depend.: FL	1 R:53,125	2 R:72,500	3 R:54,944	4 R:30,889	5 R:47,091	6 R:59,786	7 R:33,333	8 R:44,063	9 R:42,545
1		1,000000	1,000000	1,000000	1,000000	1,000000	1,000000	1,000000	1,000000
2	1,000000		1,000000	0,197723	1,000000	1,000000	1,000000	1,000000	1,000000
3	1,000000	1,000000		1,000000	1,000000	1,000000	1,000000	1,000000	1,000000
4	1,000000	0,197723	1,000000		1,000000	0,625533	1,000000	1,000000	1,000000
5	1,000000	1,000000	1,000000	1,000000		1,000000	1,000000	1,000000	1,000000
6	1,000000	1,000000	1,000000	0,625533	1,000000		1,000000	1,000000	1,000000
7	1,000000	1,000000	1,000000	1,000000	1,000000	1,000000		1,000000	1,000000
8	1,000000	1,000000	1,000000	1,000000	1,000000	1,000000	1,000000		1,000000
9	1,000000	1,000000	1,000000	1,000000	1,000000	1,000000	1,000000	1,000000	

	Multiple Comparisons z' values; FW Independent (grouping) variable: pV Kruskal-Wallis test: H (8, N= 98) =18,25859 p =,0194								
Depend.: FW	1 R:56,219	2 R:43,000	3 R:39,389	4 R:32,778	5 R:50,091	6 R:63,214	7 R:10,833	8 R:39,563	9 R:64,364
1		0,97112	1,42053	1,97854	0,65591	0,67227	2,53699	1,35280	0,73134
2	0,97112		0,24096	0,68211	0,54146	1,45694	1,59985	0,22385	1,48041
3	1,42053	0,24096		0,49322	0,95121	1,96119	1,50640	0,01256	1,95417
4	1,97854	0,68211	0,49322		1,53881	2,50539	1,15764	0,49105	2,47147
5	0,65591	0,54146	0,95121	1,53881		1,34998	2,24329	0,89684	1,35930
6	0,67227	1,45694	1,96119	2,50539	1,34998		2,89556	1,87681	0,10032
7	2,53699	1,59985	1,50640	1,15764	2,24329	2,89556		1,49242	2,89036
8	1,35280	0,22385	0,01256	0,49105	0,89684	1,87681	1,49242		1,87713
9	0,73134	1,48041	1,95417	2,47147	1,35930	0,10032	2,89036	1,87713	

	Multiple Comparisons p values (2-tailed); FW Independent (grouping) variable: pV Kruskal-Wallis test: H (8, N= 98) =18,25859 p =,0194								
Depend.: FW	1 R:56,219	2 R:43,000	3 R:39,389	4 R:32,778	5 R:50,091	6 R:63,214	7 R:10,833	8 R:39,563	9 R:64,364
1		1,00000	1,00000	1,00000	1,00000	1,00000	0,40250	1,00000	1,00000
2	1,00000		1,00000	1,00000	1,00000	1,00000	1,00000	1,00000	1,00000
3	1,00000	1,00000		1,00000	1,00000	1,00000	1,00000	1,00000	1,00000
4	1,00000	1,00000	1,00000		1,00000	0,44033	1,00000	1,00000	0,48441
5	1,00000	1,00000	1,00000	1,00000		1,00000	0,89561	1,00000	1,00000
6	1,00000	1,00000	1,00000	0,44033	1,00000		0,13625	1,00000	1,00000
7	0,40250	1,00000	1,00000	1,00000	0,89561	0,13625		1,00000	0,13852
8	1,00000	1,00000	1,00000	1,00000	1,00000	1,00000	1,00000		1,00000
9	1,00000	1,00000	1,00000	0,48441	1,00000	1,00000	0,13852	1,00000	

	Multiple Comparisons z' values; FP Independent (grouping) variable: pV Kruskal-Wallis test: H (8, N= 98) =12,14467 p =,1449								
Depend.: FP	1 R:51,563	2 R:70,000	3 R:53,722	4 R:30,333	5 R:47,091	6 R:62,714	7 R:36,667	8 R:43,563	9 R:43,364
1		1,354523	0,18229	1,79186(	0,47863	1,07168	0,83266	0,64975	0,73618
2	1,354523		1,08619	2,64689(	1,74934(	0,52511	1,65788	1,72161	1,84579
3	0,18229	1,08619		1,74492	0,58940	0,74018(	0,89974(	0,73533	0,81051
4	1,79186(	2,64689(	1,74492		1,48944(	2,66545	0,33410	0,95749(	1,01957(
5	0,47863	1,74934(	0,58940	1,48944(		1,60716(	0,59567	0,30056	0,35497
6	1,07168	0,52511	0,74018(	2,66545	1,60716(		1,43988(	1,51973	1,68906
7	0,83266	1,65788	0,89974(	0,33410	0,59567	1,43988(		0,35822	0,36160
8	0,64975	1,72161	0,73533	0,95749(	0,30056	1,51973	0,35822		0,01505
9	0,73618	1,84579	0,81051	1,01957(	0,35497	1,68906	0,36160	0,01505	

	Multiple Comparisons p values (2-tailed); FP Independent (grouping) variable: pV Kruskal-Wallis test: H (8, N= 98) =12,14467 p =,1449								
Depend.: FP	1 R:51,563	2 R:70,000	3 R:53,722	4 R:30,333	5 R:47,091	6 R:62,714	7 R:36,667	8 R:43,563	9 R:43,364
1		1,00000(	1,00000(	1,00000(	1,00000(	1,00000(	1,00000(	1,00000(	1,00000(
2	1,00000(		1,00000(	0,29244	1,00000(	1,00000(	1,00000(	1,00000(	1,00000(
3	1,00000(	1,00000(		1,00000(	1,00000(	1,00000(	1,00000(	1,00000(	1,00000(
4	1,00000(	0,29244	1,00000(		1,00000(	0,27678	1,00000(	1,00000(	1,00000(
5	1,00000(	1,00000(	1,00000(	1,00000(		1,00000(	1,00000(	1,00000(	1,00000(
6	1,00000(	1,00000(	1,00000(	0,27678	1,00000(		1,00000(	1,00000(	1,00000(
7	1,00000(	1,00000(	1,00000(	1,00000(	1,00000(	1,00000(		1,00000(	1,00000(
8	1,00000(	1,00000(	1,00000(	1,00000(	1,00000(	1,00000(	1,00000(		1,00000(
9	1,00000(	1,00000(	1,00000(	1,00000(	1,00000(	1,00000(	1,00000(	1,00000(	

APPENDIX E5: Kruskal-Wallis ANOVA by Ranks on the Total Fracture Data Set

Kruskal-Wallis ANOVA by Ranks; FN
Independent (grouping) variable: Potential
Kruskal-Wallis test: H (3, N= 33) =5,639619 p =,13

Depend.: FracNo	Code	Valid N	Sum of Ranks	Mean Rank
1	1	9	97,500(	10,8333
2	2	6	118,500(	19,7500(
3	3	9	159,500(	17,7222
4	4	9	185,500(	20,6111

Kruskal-Wallis ANOVA by Ranks; TFA
Independent (grouping) variable: Potential
Kruskal-Wallis test: H (3, N= 33) =1,388462 p =,70

Depend.: TFA	Code	Valid N	Sum of Ranks	Mean Rank
1	1	9	127,500(	14,1666
2	2	6	97,000(	16,1666
3	3	9	171,000(	19,0000(
4	4	9	165,500(	18,3888

Kruskal-Wallis ANOVA by Ranks; TFA/TBA
Independent (grouping) variable: Potential
Kruskal-Wallis test: H (3, N= 33) =1,331773 p =,72

Depend.: TFA/TBA	Code	Valid N	Sum of Ranks	Mean Rank
1	1	9	128,500(	14,2777
2	2	6	96,000(	16,0000(
3	3	9	169,000(	18,7777
4	4	9	167,500(	18,6111

Kruskal-Wallis ANOVA by Ranks; FN
Independent (grouping) variable: Mode
Kruskal-Wallis test: H (1, N= 33) =,7154142 p =,3977

Depend.: FracNo	Code	Valid N	Sum of Ranks	Mean Rank
1	1	18	283,000(	15,7222
2	2	15	278,000(	18,5333

Kruskal-Wallis ANOVA by Ranks; TFA
Independent (grouping) variable: Mode
Kruskal-Wallis test: H (1, N= 33) =,2209889 p =,6383

Depend.: TFA	Code	Valid N	Sum of Ranks	Mean Rank
1	1	18	293,000(	16,2777
2	2	15	268,000(	17,8666

Kruskal-Wallis ANOVA by Ranks; TFA/TBA
Independent (grouping) variable: Mode
Kruskal-Wallis test: H (1, N= 33) =,1307408 p =,7177

Depend.: TFA/TBA	Code	Valid N	Sum of Ranks	Mean Rank
1	1	18	296,000(	16,4444
2	2	15	265,000(	17,6666

Kruskal-Wallis ANOVA by Ranks; FN
Independent (grouping) variable: pC
Kruskal-Wallis test: H (8, N= 33) =15,52789 p =,0497

Depend.: FracNo	Code	Valid N	Sum of Ranks	Mean Rank
1	1	9	97,5000(	10,8333
2	2	3	52,0000(	17,3333
3	3	3	66,5000(	22,1666
4	4	3	74,0000(	24,6666
5	5	3	21,0000(	7,0000(
6	6	3	64,5000(	21,5000(
7	7	3	38,5000(	12,8333
8	8	3	82,5000(	27,5000(
9	9	3	64,5000(	21,5000(

Kruskal-Wallis ANOVA by Ranks; TFA
Independent (grouping) variable: pC
Kruskal-Wallis test: H (8, N= 33) =13,22545 p =,1043

Depend.: TFA	Code	Valid N	Sum of Ranks	Mean Rank
1	1	9	127,500(	14,1666
2	2	3	36,500(	12,1666
3	3	3	60,500(	20,1666
4	4	3	73,000(	24,3333
5	5	3	18,000(	6,0000(
6	6	3	80,000(	26,6666
7	7	3	34,500(	11,5000(
8	8	3	72,000(	24,0000(
9	9	3	59,000(	19,6666

Kruskal-Wallis ANOVA by Ranks; TFA/TBA
Independent (grouping) variable: pC
Kruskal-Wallis test: H (8, N= 33) =13,58278 p =,0933

Depend.: TFA/TBA	Code	Valid N	Sum of Ranks	Mean Rank
1	1	9	128,500(	14,2777{
2	2	3	36,000(	12,0000(
3	3	3	60,000(	20,0000(
4	4	3	72,000(	24,0000(
5	5	3	17,000(	5,66667
6	6	3	80,000(	26,66667
7	7	3	34,500(	11,5000(
8	8	3	74,000(	24,66667
9	9	3	59,000(	19,66667

Kruskal-Wallis ANOVA by Ranks; FN
Independent (grouping) variable: pV
Kruskal-Wallis test: H (9, N= 33) =15,63993 p =,0748

Depend.: FracNo	Code	Valid N	Sum of Ranks	Mean Rank
1	1	3	82,5000(	27,5000(
2	2	3	37,0000(	12,3333{
3	3	6	60,5000(	10,0833{
4	4	3	52,0000(	17,3333{
5	5	3	66,5000(	22,16667
6	6	3	74,0000(	24,66667
7	7	3	64,5000(	21,5000(
8	8	3	21,0000(	7,0000(
9	9	3	38,5000(	12,8333{
10	10	3	64,5000(	21,5000(

Kruskal-Wallis ANOVA by Ranks; TFA
Independent (grouping) variable: pV
Kruskal-Wallis test: H (9, N= 33) =13,93291 p =,1247

Depend.: TFA	Code	Valid N	Sum of Ranks	Mean Rank
1	1	3	72,0000(	24,0000(
2	2	3	54,0000(	18,0000(
3	3	6	73,5000(	12,2500(
4	4	3	36,5000(	12,16667
5	5	3	60,5000(	20,16667
6	6	3	73,0000(	24,3333{
7	7	3	80,0000(	26,66667
8	8	3	18,0000(	6,0000(
9	9	3	34,5000(	11,5000(
10	10	3	59,0000(	19,66667

	Kruskal-Wallis ANOVA by Ranks; TFA/TBA Independent (grouping) variable: pV Kruskal-Wallis test: H (9, N= 33) =14,37451 p =,1096			
Depend.: TFA/TBA	Code	Valid N	Sum of Ranks	Mean Rank
1	1	3	74,0000(	24,66667
2	2	3	55,0000(	18,33333
3	3	6	73,5000(	12,2500(
4	4	3	36,0000(	12,0000(
5	5	3	60,0000(	20,0000(
6	6	3	72,0000(	24,0000(
7	7	3	80,0000(	26,66667
8	8	3	17,0000(	5,66667
9	9	3	34,5000(	11,5000(
10	10	3	59,0000(	19,66667

APPENDIX F: Principal Component Analysis of the Total Fracture Data Set, Second Iteration

Table F1: Eigenvalues, respective percentage of variance and cumulative percentages of Variance for the total fracture data set's first iteration

PC	Eigenvalue	Percentage of Variance	Cumulative Percentage of Variance
1	**3.137**	**44.810**	**44.810**
2	**2.024**	**28.916**	**73.726**
3	1.093	15.618	89.344
4	.457	6.524	95.868
5	.277	3.957	99.825
6	.007	.096	99.921
7	.006	.079	100.000

Table F2: Principal component extraction with Varimax rotation and Kaiser Normalization of the total fracture data set's first iteration

	Principal Component 1	Principal Component 2	Principal Component 3
TFA/TBA	**.967**	.081	-.004
TFA	**.964**	.084	.042
FN	**.875**	.153	.023
pC	.178	**.966**	.012
CP	.211	**.961**	.014
pV	-.219	**.613**	.566
Mode	.117	-.013	**.945**

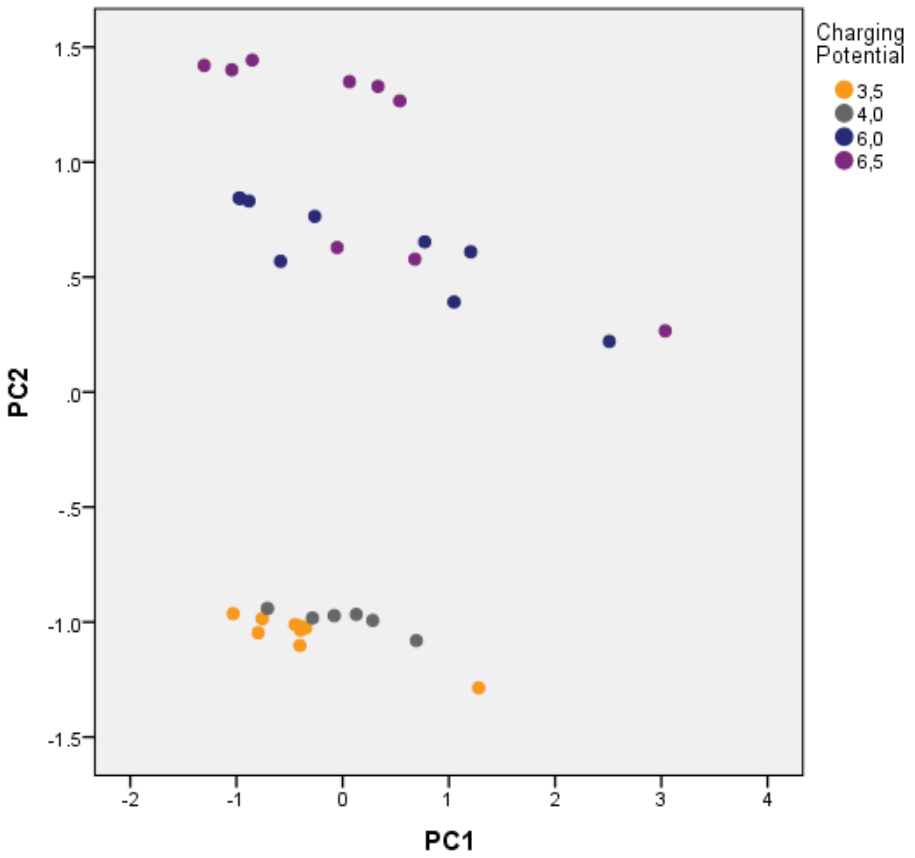


Figure F1: Graphic Representation of PC1 against PC2 of the Second Iteration of the Total Fracture Data Set

APPENDIX G: Ethical Clearance Waiver

Human Research Ethics Committee (Medical)

Research Office Secretariat: Senate House Room SH 10005, 10th floor. Tel +27 (0)11-717-1252
Medical School Secretariat: Medical School Room 10M07, 10th Floor. Tel +27 (0)11-717-2700
Private Bag 3, Wits 2050, www.wits.ac.za. Fax +27 (0)11-717-1265

UNIVERSITY OF THE WITWATERSRAND JOHANNESBURG

Ref: W-CJ-140604-1 04/06/2014

TO WHOM IT MAY CONCERN:

Waiver: This certifies that the following research does not require clearance from the Human Research Ethics Committee (Medical).

Investigator: School of Anatomical Sciences (Head: Prof T J M Daly).

Project title: research on cadaveric material.

Reason: In terms of Chapter 8, sections 62-64 of the National Health Act No 61 of 2003 donated bodies and their tissues may be used for, among other purposes, health research. Use of such material is subject only to permission from the responsible person in the School of anatomical Sciences – the Head or person designated by the Head.

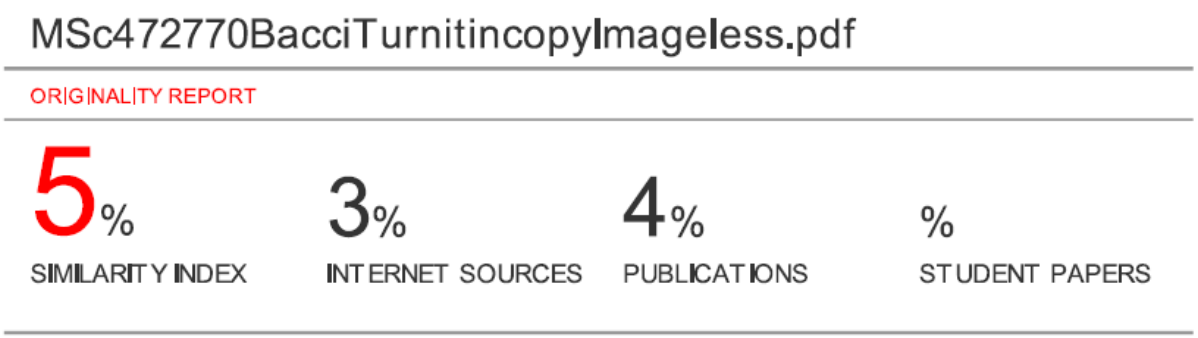
UNIVERSITY OF THE WITWATERSRAND
PROF PE CLEATON-JONES
HREC (MEDICAL)
2014 -06- 04
JOHANNESBURG

Professor Peter Cleaton-Jones

Chair: Human Research Ethics Committee (Medical)

Copy - HREC(Medical) Secretariat : Anisa Keshav, Zanele Ndlovu.

APPENDIX H: Plagiarism Report – Turnitin Report



MSc472770BacciTurnitincopyImageless.pdf

ORIGINALITY REPORT

5%	3%	4%	%
SIMILARITY INDEX	INTERNET SOURCES	PUBLICATIONS	STUDENT PAPERS